ALMA MATER STUDIORUM – UNIVERSITÀ DI BOLOGNA

CAMPUS DI CESENA

DIPARTIMENTO DI

INGEGNERIA DELL'ENERGIA ELETTRICA E DELL'INFORMAZIONE

"GUGLIELMO MARCONI"

CORSO DI LAUREA MAGISTRALE IN INGEGNERIA BIOMEDICA

TITOLO DELLA TESI

DEVELOPMENT OF PROCEDURES TO PERFORM NANOINDENTATION TESTS ON DIFFERENT BONE STRUCTURES

Tesi in

Meccanica dei Tessuti Biologici LM

Relatore

Prof. Ing. Luca Cristofolini

Presentata da

Valentina Pepe

Correlatori

Dr. Enrico Dall'Ara

Dr.ssa Sara Oliviero

Dr.ssa Meena Balasubramanian

Anno accademico 2017/2018

Have a grateful heart

Be yourself

Dream big

Say I love you

Believe in miracles

A.P.

ACKNOWLEDGMENTS

The first dutiful thanks go to my supervisor Prof. Luca Cristofolini for giving me the opportunity to have this fantastic experience abroad and to have always guided me during the writing of this theses.

I would like to acknowledge my supervisor at the University of Sheffield Dr. Enrico Dall'Ara for his extreme availability and for teaching me so many things I will need for the rest of my life.

I would like also to thank my co-supervisor Dr.ssa Sara Oliviero for her support and help during these months in Sheffield.

My sincere thank you to Dr.ssa Meena Balasubramanian for giving me a chance to work on OI human bone sample.

The research is generously funded by Newlife Foundation for Disabled Children (Grant GC/17-18/01: 'Charlie Veale Research Award') for "Comprehensive characterisation of bone tissue from High Bone Mass Osteogenesis Imperfecta patients" study.

The study was funded by the UK National Centre for the Replacement, Refinement and Reduction of Animals in Research (NC3Rs, Grant number: NC/K000780/1) and by the Engineering and Physical Sciences Research Council (EPSRC, MultiSim project, Grant number: EP/K03877X/1).

I wish to thank the School of Engineering and Architecture of the University of Bologna for the financial support to this international exchange.

Thank you to Dawn Bussey for her great patience in teaching me how to use the Nanoindenter.

Thank you to Caroline J Fry for her availability during the microCT scans.

Finally, my sincere thank you to all Insigneo's members for making me feel part of a family during these months.

ABSTRACT

In recent years, nanoindentation has emerged as a powerful technique for investigating the micromechanical properties of bone. This technique allows the decoupling at the microscopic scale of the mechanical properties in multiple directions.

Indentation consists in pressing a hard tip with a known force into a semi-infinite half-space and measuring directly or indirectly the contact area. Nanoindentation is an evolution of the conventional hardness test for assessment of the mechanical properties of thin films and surface layers.

The main goal of this work was to develop a procedure to perform nanoindentation tests on bone tissue in order to study the elastic and inelastic properties of different bone structures. This procedure concerned the entire study of the specimens, from dissection to nanoindentation tests, to the elaboration and analyses of the results. From the nanoindentation measures the values of reduced modulus, hardness, indentation modulus and elastic modulus were obtained. The idea was to perform nanoindentation tests both for preclinical and clinical applications and for that reason, the nanoindentation tests were made both on mouse and on OI (Osteogenesis imperfecta) human bone. Nanoindentation has already been used in previous studies to test the mechanical properties of bone, but it is the first time these tests have been performed on mouse tibiae.

Nanoindentations on mouse bone were performed on different slices of four tibiae obtained from two strains (C57B1/6 and Balb/C), both on cortical and on trabecular bone. Our results are in line with the literature and we found that the reduced modulus (that represents the elastic behaviour of the tissue) ranged between 16.50 ± 7.10 GPa (C57B1/6, trabecular bone) and 25.08 ± 5.21 GPa (Balb/C, cortical bone). The hardness (that is a measure of the resistance to plastic deformation) ranged between 0.62 ± 0.27 GPa (C57B1/6, trabecular bone) and 0.96 ± 0.20 GPa (Balb/C, cortical bone).

The procedure had as its final goal to investigate potential differences between strains, spatial location (Proximal, Central or Distal regions) and spatial orientation (Anterior, Posterior, Medial and Lateral sections). We found no significant differences between the two strains (C57B1/6 vs Balb/C); but we found differences between different mice of the same strain. Our conclusion is that at the tissue level the two strains have similar mechanical

properties, but the inter-subject variability seems greater. We had a limited number of samples, therefore further analyses would be needed to support this idea. We found also significant differences between the three sections (Proximal, Central and Distal). The proximal section was significantly different from both the Central and Distal ones. The lower mechanical properties at the proximal end may be due to the fact that it is closer to the growth plate, where the tissue is younger and less mineralised. Finally, no significant differences were found between the Anterior, Posterior, Medial and Lateral sectors. Potential differences between cortical and trabecular bone were not investigated (the number of the cortical bone indentations was much higher than those on the trabecular bone), but we found differences between proximal cortical and proximal trabecular bone.

Nanoindentations on an OI specimen were performed on different slices to investigate potential differences between the two regions and the four sections. We tested only one OI specimen obtained from the upper limb. Our results are in line with the literature and we found a reduced modulus (that represents the elastic behaviour) of 12.14 ± 5.79 GPa and hardness (that is a measure of the resistance to plastic deformation) of 0.49 ± 0.21 GPa.

Significant statistical differences between two regions were found: possible explanation could be due to differences in local porosity or collagen properties (this may explain the higher modulus and hardness in the first region). The four slices were significantly different too. The differences could be due to the presence of more compact tissue and more cortical bone in some sections as well as the porosity or different mineralization.

In conclusion we developed this new protocol and is now a standard procedure and may be applied to different future works. For example, for pre-clinical applications by increasing the number of different mice or for clinical applications by increasing the number of the OI samples, collecting specimens with different OI type, investigating the effect of treatments, or comparing OI bone to healthy bone.

ABSTRACT

Negli ultimi anni, la nanoindentazione è emersa come potente tecnica per indagare le proprietà micromeccaniche dell'osso. Questa tecnica consente il disaccoppiamento nella scala microscopica delle proprietà meccaniche in più direzioni.

L'indentazione consiste nel premere una punta rigida con una forza nota in un semispazio semi-infinito e nel misurare direttamente o indirettamente l'area di contatto. La nanoindentazione è un'evoluzione dei test di durezza convenzionali per la stima delle proprietà meccaniche degli strati superficiali.

L'obiettivo principale di questo lavoro è stato quello di sviluppare una procedura per eseguire test di nanoindentazione sul tessuto osseo al fine di studiare le proprietà elastiche e inelastiche di diverse strutture ossee. Questa procedura riguardava l'intero studio dei campioni, dalla dissezione ai test di nanoindentazione, all'elaborazione e alle analisi dei risultati. Dalle misure di nanoindentazione sono stati ricavati i valori di reduced modulus, hardness, indentation modulus ed elastic modulus. L'idea era di eseguire test di nanoindentazione sia per applicazioni precliniche che cliniche e per questo motivo, i test di nanoindentazione sono stati effettuati sia su ossa di topo che su ossa umane affette da una particolare condizione patologica, chiamata Osteogenesi Imperfetta. La nanoindentazione è già stata utilizzata in altri studi per testare le proprietà meccaniche dell'osso, ma è la prima volta che questi test vengono eseguiti su tibie di topo.

Le nanoindentazioni sull'osso del topo sono state eseguite su diverse fette di quattro tibie ottenute da due ceppi (C57B1/6 e BALB/C), sia su osso corticale che trabecolare. I nostri risultati sono in linea con la letteratura e abbiamo trovato che il modulo elastico (che rappresenta il comportamento elastico del tessuto) varia tra 16.50 ± 7.10 GPa (C57B1/6, osso trabecolare) e 25.08 ± 5.21 GPa (Balb/C, osso corticale). L'hardness (che misura la resistenza alla deformazione plastica) varia tra 0.62 ± 0.27 GPa (C57B1/6, osso trabecolare) e 0.96 ± 0.20 GPa (Balb/C, osso corticale).

La procedura ha avuto come obiettivo finale quello di indagare le potenziali differenze tra le due razze, la posizione spaziale (regioni prossimali, centrali o distali) e l'orientamento spaziale (sezioni anteriori, posteriori, mediali e laterali). Non abbiamo riscontrato differenze significative tra i due ceppi (C57B1/6 vs BALB/C); ma abbiamo trovato differenze tra

diversi topi dello stesso ceppo. La nostra conclusione è che a livello di tessuto i due ceppi hanno proprietà meccaniche simili, ma la variabilità inter-soggetto sembra maggiore. Tuttavia, abbiamo avuto un numero limitato di campioni, quindi sarebbero necessarie ulteriori analisi per sostenere questa idea.

Abbiamo riscontrato anche differenze significative tra le tre sezioni (prossimale, centrale e distale). La sezione prossimale era significativamente diversa da quella centrale e quella distale. Le proprietà meccaniche all'estremità prossimale possono essere inferiori dal momento che essa è più vicina al growth plate, dove il tessuto è più giovane e meno mineralizzato. Infine, non sono state riscontrate differenze significative tra i settori anteriore, posteriore, mediale e laterale. Non sono state studiate le potenziali differenze tra l'osso corticale e quello trabecolare (il numero delle indentazioni sull'osso corticale era molto più elevato di quelle su osso trabecolare), ma abbiamo trovato differenze tra l'osso prossimale corticale e l'osso prossimale trabecolare.

Le nanoindentazioni sul campione di OI sono state condotte su diverse fette, per analizzare le potenziali differenze tra le due regioni e le quattro sezioni. Abbiamo testato solamente un campione di OI ottenuto dall'arto superiore. I nostri risultati sono in linea con la letteratura e abbiamo trovato un modulo elastico (che rappresenta il comportamento elastico) di 12.14 ± 5.79 GPa e l'hardness (che rappresenta la resistenza alla deformazione plastica) di 0.49 ± 0.21 GPa.

Sono state rilevate significative differenze statistiche tra le due regioni: questo potrebbe essere dovuto a differenze nella porosità locale o a proprietà del collagene (questo può spiegare un modulo elastico e hardness maggiori nella prima regione). Anche le quattro fette erano significativamente diverse. Le differenze potrebbero essere dovute alla presenza di maggior tessuto compatto e corticale in alcune sezioni, oltreché alla presenza di porosità o diversa mineralizzazione.

In conclusione, abbiamo sviluppato questo nuovo protocollo che può essere applicato a diversi lavori futuri. Ad esempio, per le applicazioni precliniche aumentando il numero di topi diversi o per applicazioni cliniche aumentando il numero dei campioni di OI, raccogliendo campioni con diversi tipi di OI, indagando l'effetto dei trattamenti o confrontando le ossa di OI con osso sano.

CONTENTS

CHAPTER 1

BACKGROUND

1.1 Bone

Bone is a highly specialized mineralized connective tissue with structural and metabolic functions. The structural functions consist in providing stiffness, support and resistance to bear the physiological and accidental loads; in supporting the soft tissues and in protecting important districts of the body. The metabolic functions, instead, consists in acting as the main deposit of calcium ions and in maintaining a homeostatic balance of minerals within the body. Bone is a composite heterogeneous and anisotropic biomaterial with a complex hierarchical structure [1].

Different types of bones have different shapes related to their function. There are five types of bones in the skeleton: flat, long, short, irregular, and sesamoid bones.

There are flat bones in the skull (occipital, parietal, frontal), the thoracic cage (sternum and ribs), and the pelvis (ilium, ischium, and pubis). The function is to protect internal organs such as the brain, heart, and pelvic organs.

The long bones (femur, tibia, humerus) support the weight of the body and facilitate movement.

The short bones (scaphoid, trapezoid, calcaneus) are in the wrist and ankle joints and they provide stability and some movement.

Irregular bones vary in shape and structure and therefore do not fit into any other category. They often have a complex shape, which helps protect internal organs. For example, the vertebrae protect the spinal cord.

Sesamoid bones are bones embedded in tendons (like the patella). These small, round bones are commonly found in the tendons of the hands, knees, and feet. Sesamoid bones protect tendons from stress and wear [2].

Long bones like femur and tibia are composed of a Diaphysis, central cylindrical tract with external cortical bone and internal trabecular bone, and two Epiphysis, bone ends enlarged in correspondence of the joints that consist of a layer of cortical bone that surrounds a trabecular bone structure.

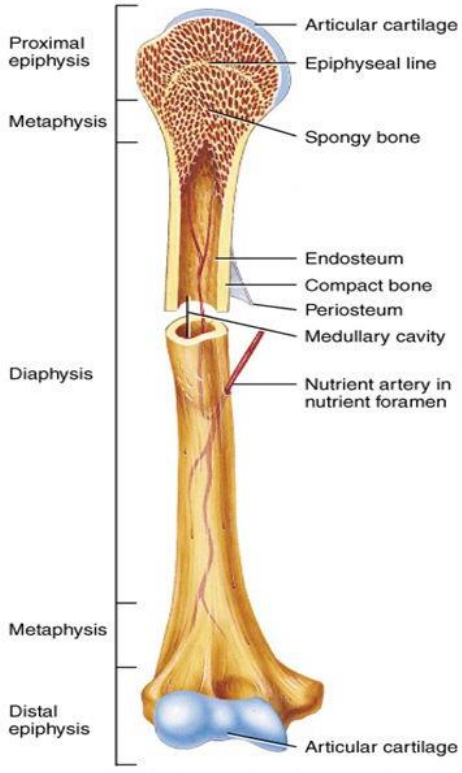

Figure 1: Long bone with Epiphysis, Metaphisis and Diaphysis. Source from https://anatomylife.com/bone-anatomy-epiphyseal-plate/

All skeletal bones consist of an outer surface enveloped by the *periosteum* (a layer of vascularized soft tissue that supplies blood to the bone). The internal cavity is coated by the *endosteum* (layer of cells that separates the bone from the marrow). Periosteum and endosteum host surface cells (osteoclasts, osteocytes) [3].

Each hierarchical level contributes to the global mechanical response:

- The mineralized collagen fibril (MCF, 200 nm)
- The lamella (2–7 μm)
- The bone structural unit (BSU, 60 μm)
- Trabecular (or cancellous or spongy) bone (mm)
- Organ (cm) [4]

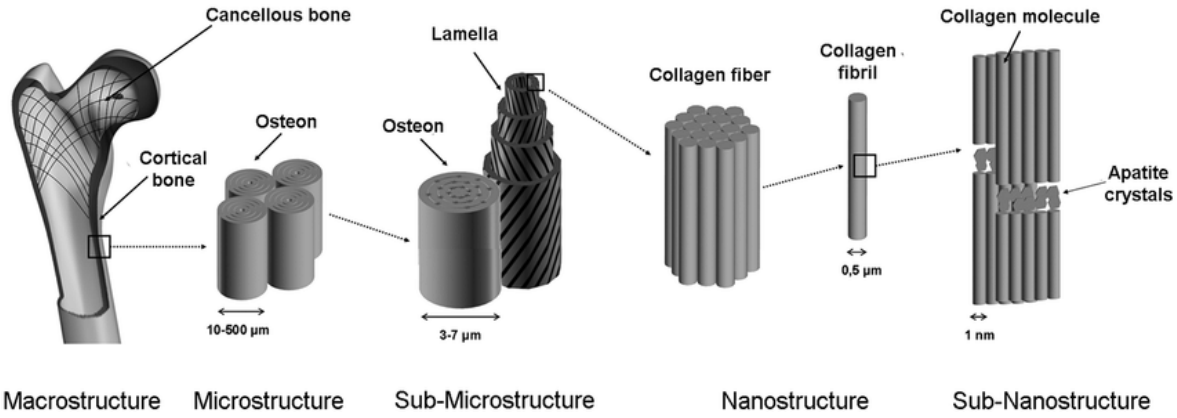

Figure 2: Hierarchical levels. Source from https://www.researchgate.net/figure/The-hierarchical-levels-of-bone-structure-The-six-levels-represent-the-bone-structure_fig1_41458030

In all tissues there are cells and extracellular matrix in different percentages. Cells dispersed in a matrix with tissue formation/repair function and stress state sensor. The extracellular matrix creates the supporting structure for the cells and provides mechanical support. The bone is constituted for 65% by inorganic components (minerals) and for 35% by organic matrix, cells, and water. The inorganic part is solid and brittle, instead the organic part is tough and yielding. Therefore, a phase has mechanical functions of resistance, stiffness and toughness and a phase has a function of connection and filling [5]. The matrix consists of 60% of inorganic components, especially calcium phosphate in the form of hydroxyapatite microcrystals [1].

Bone cells belong to three families. Osteoblasts are responsible for the formation of new tissue. Osteocytes (osteoblasts that differentiate after being trapped in the extracellular matrix) are responsible for tissue maintenance and they coordinate the activity of osteoblasts and osteoclasts; they are found in empty spaces, called lacunae, located between the lamellae. Osteoclasts are responsible for the removal of old or damaged tissue [1-3].

The calcified tissues must therefore be solid to avoid excessive deformations and tough to absorb and dissipate energy in shocks to minimize the energy transmitted to the most vulnerable organs. Calcium mineral are mainly phosphates and calcium carbonates. Specifically, bone is made of calcium and phosphorus apatite like hydroxyapatite but not stoichiometrically exact ($Ca_{10}(PO_4)_6$ $(OH)_2$) and this makes it less stable and precipitates in the form of crystals (as shown in the Fig.3) [3].

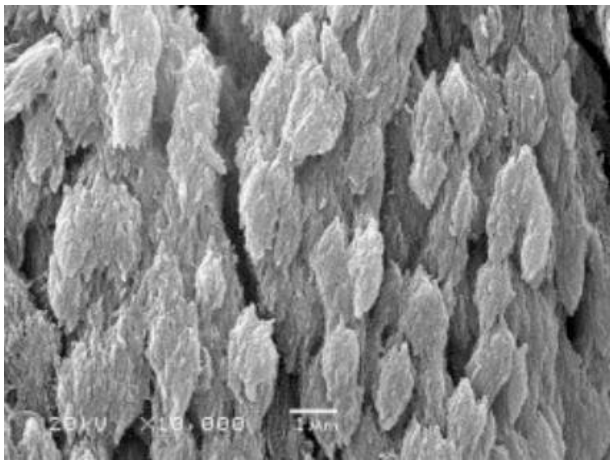

Figure 3: Calcium and phosphorus apatite (like hydroxyapatite) which precipitates in the form of crystals [3]

Hydroxyapatite crystals are mainly responsible for the mechanical properties of calcified tissues. The calcium minerals confer rigidity and high tensile strength, but they make the tissue brittle; the collagen instead represents the deformable and tenacious part (collagen contributes to bone's elastic and viscoelastic behaviour) [3].

1.1.1 Bone microstructure

The bone tissue can be lamellar or non-lamellar.
Non-Lamellar Bone is a tissue in which collagen fibres are collected in large parallel or twisted bundles. It is an amorphous and tendentially isotropic material.

Lamellar or Stratified Bone consists of lamellae or distinct layers in which the collagen fibres are oriented with a strong parallelism. The lamellae with different orientation are juxtaposed to generate a microscopic structure like the plywood [3].

Bone tissues are very resistant and light, and this depends on the internal organization. All bones are formed by two architectural structures that differ in the content of bone tissue and marrow. Cortical bone is compact (with a porosity of 5-10%) and mechanically stiff as well as heavy and expensive in metabolic terms; Trabecular bone is composed by a network of rods, arches and small plates with a porosity of 45-95% of the volume. A thin shell of cortical bone filled with trabecular bone is an optimal structure (from the mechanical point of view) because the cortical bone supports the loads and the trabecular bone supports and prevents instability.

1.1.2 Cortical bone

Cortical bone is about 80% by weight of the skeleton and it is made by lamellae. The lamellae are the structural element of the bone, of which they constitute the scaffolding. Each lamella is approximately 3 to 7 μm thick and contains fine fibres that run in approximately the same direction. The packages of lamellae have three different formats:

- Cylindrical structures of 4-20 concentric lamellae around a longitudinal vascular canal. The orientation of collagen fibres changes from one lamella to the next. The vascular canal and the lamellae form an *osteon* or *Haversian system* (diameter of 150-250 μm, Fig.4).

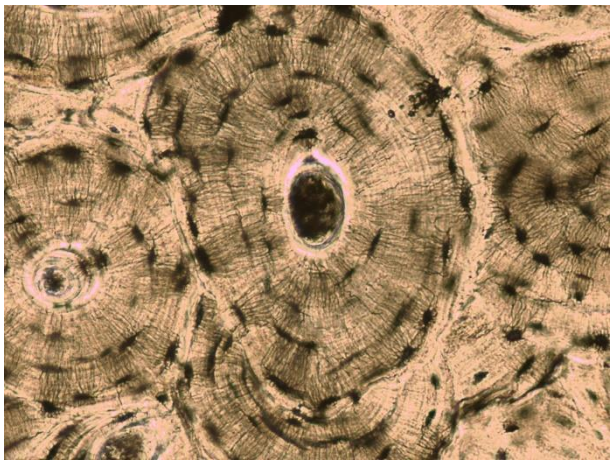

Figure 4: Osteons or Haversian systems. Source from: https://www.pinterest.it/pin/565905509399132109/

Each osteon is surrounded by the *cement line* of 1-2 μm (mineralized matrix poor in collagen fibres).

The osteonal bone tissue is not homogeneous (its characteristics vary according to the position) and anisotropic (its properties vary according to the direction in which it is loaded). The inhomogeneity is due to non-homogeneous distribution of structural units. Anisotropy is due to the orientation of the osteons. The osteons do not have a random distribution in the bone, in fact there are significant differences from region to region due to local stress type (tension, compression, torsion). In fact, it has been observed that the osteons are disposed according to a certain direction rather than in others (they align themselves according to the trend of the main tensions); a thesis supported also by the fact that, in general, for the cortical bone, the longitudinal Young's modulus is decidedly superior compared to the transversal (for a long bone 17.4 GPa in the longitudinal direction, 9.6 GPa in transverse direction) [3-6].

The Fig.5 shows the direction of the osteons according to the load direction (transversal, longitudinal and alternating).

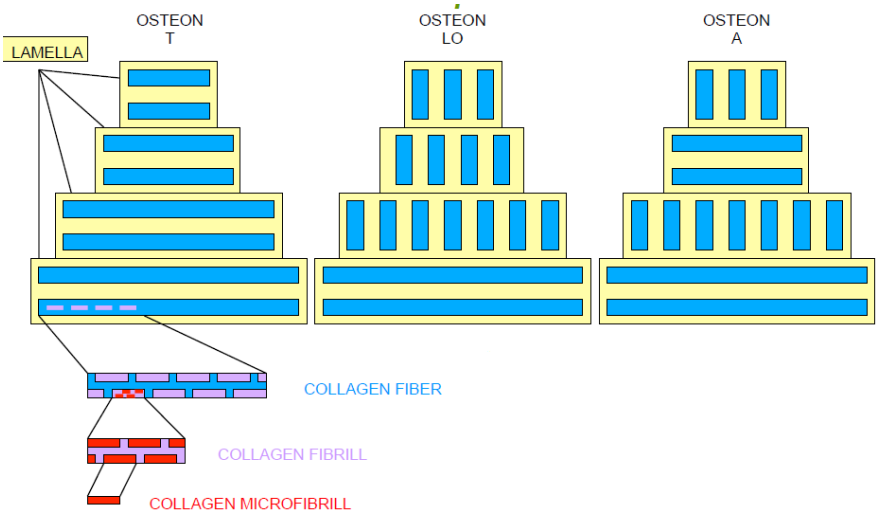

Figure 5: Osteons' distribution due to local stress (transversal direction on the right, longitudinal in the middle and alternating on the left) [3]

- *Interstitial lamellae*: fragments of osteons and reconstituted circumferential lamellae during the regeneration process. They fill the spaces between the haversian systems.

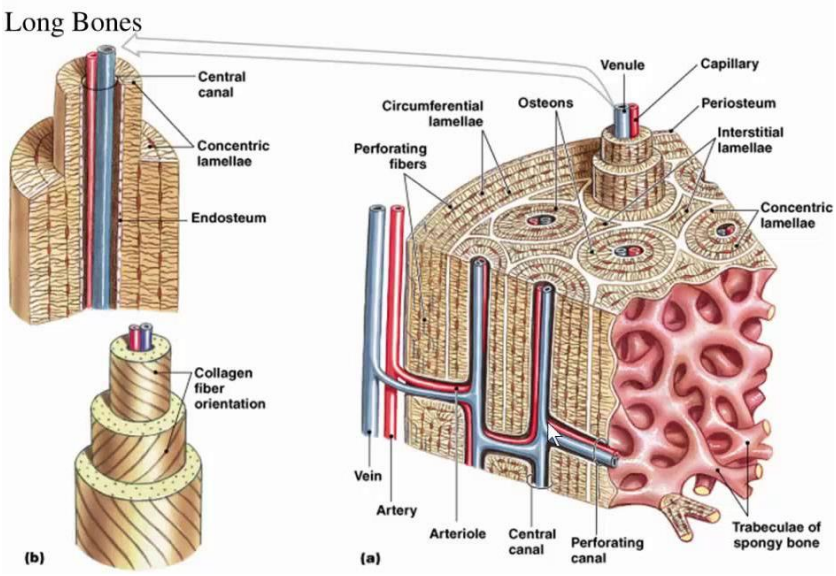

*Figure 6: The structure of the compact bone. Source from https://www.visualizepicture.com/c/spongy-bone-structure_HapJAd*voUaH6BmyFveFZBI7qeRNsoouZXpuxxx2MhM/*

- Layers of lamellae develop without interruption to wrap the bone. They are on the outer surface of the cortical bone (under the periosteum) and inside (adjacent to the endosteum).

The canaliculi and Volkmann's canals form a 3D network that provides nutriment to the cells. The Volkmann's canals are of the same size of the Haversian canals; the canaliculi are a few orders of magnitude smaller. They are connected to the periosteum and bone marrow. Each osteocyte is in a lacuna that is connected to at least one canaliculus [3].

1.1.3 Trabecular bone

Trabecular bone (Fig.7) is a network of trabeculae (thickness less than 0.2 mm) interconnected. The interstitial space is filled by the marrow that contributes to the stiffness [3].

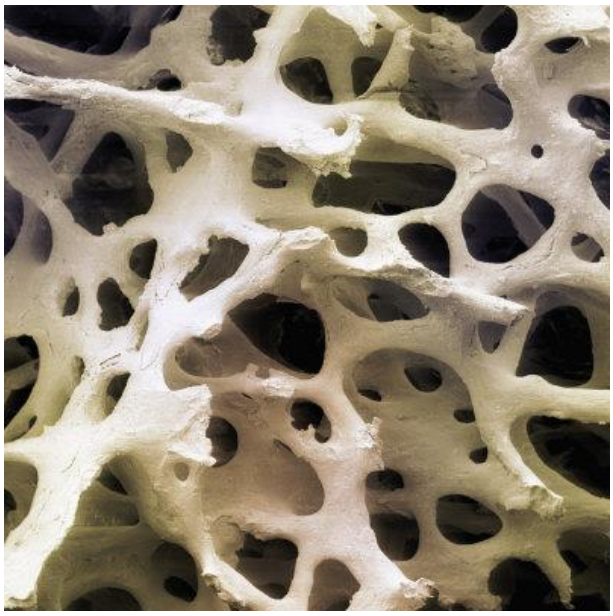

Figure 7: Trabecular bone. Source from https://www.sciencephoto.com/media/118920/view

Packages of parallel lamellae form each trabecula. These packages (up to 1 mm long and 50-60 μm in diameter) are the analogue of the osteon in the compact bone. The cement lines are located between the lamella packages. The trabecular bone absorbs impacts very well. The density and thickness of the trabeculae depend on the intensity of the transmitted loads. The trabeculae tend to align themselves according to the directions of the main stresses (Fig.8) [3].

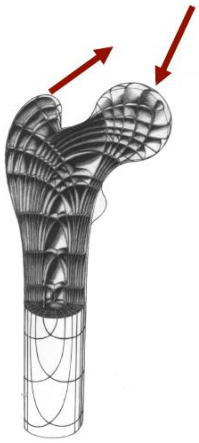

Figure 8: Trabeculae alignment according to the directions of the main stresses [3]

1.1.4 Mechanical properties of bone

The mechanical properties of bone are often determined experimentally in vitro. There are no significant differences between live and immediately post-mortem specimens

because most of the bone tissue is made up of the extracellular matrix. Furthermore, the presence of water also affects the mechanical properties. The water in the bone is present for 10-20% by weight: one part is trapped in the trabecular bone, the other one is in the collagen [3].

The bone is a fragile material, so it has little plastic deformation before the fracture. The cortical bone is strong and stiff: the fracture does not take place according to a very precise angle, but it follows the direction that opposes lower stress and deformation, according to the arrangement of the osteons [7]. Fractures occur when the local stress acting at one or more sites in bone exceed the capacity of the bone to dissipate the related energy without suffering damage that results in a substantial loss of structural integrity. Intrinsic material properties that contribute to increased fracture resistance include those that promote plasticity and toughness, i.e., ductility, energy absorption, and dissipation. Fracture resistance extends beyond the intrinsic material properties of bone to encompass all levels of scale up to the whole bone [8]. Fibre orientation can affect crack propagation, and the successive alteration in fibre orientation within the concentric lamellae of an osteon is thought to reflect such an adaptation in bone. Accumulated microdamage may contribute to increased fracture risk if appropriate remodelling of damaged areas is not undertaken. Intrinsic mechanisms of fracture resistance are also affected by strain rate; higher strain rates are associated with increased material stiffness and reduced ductility (post-yield plastic deformation). Thus, at abnormally high strain rates, bone behaves as if it is more "brittle" [9]

The mechanical properties of bone are usually studied under static conditions, i.e., under a slowly applied force or load. When a force is applied to a body, it produces stress and strain within the body. Stress is the ratio between the force and the area upon which it acts, i.e., force per unit area (MPa). Strain is a change in the linear dimensions of a body when a force is applied; since there are no standard units of measurement for strain, it can be recorded as percentage. A stress-strain curve is obtained by plotting stress against strain. From a tangent drawn to the straightest part of this curve the modulus of elasticity (that is a measure of the stiffness of the material) can be computed. Elasticity is the property of a material that allows it to return to its original dimensions after the removal of a force or load. The energy the specimen absorbs to failure can be determined by measuring the area below the stress-strain curve. Another mechanical property that is investigated on the bone is the hardness that is a

measure of the resistance to localized plastic deformation induced by either mechanical indentation or abrasion [10].

The main mechanical tests that are carried out on bone tissue are basically traction, compression, bending and torsion tests in which a test machine is used. It can give as output force and displacement results from which stress, deformation and/or elastic modulus values can be obtained. Another mechanical test is the nanoindentation test. Indentation consists in pressing a hard tip with a known force into a semi-infinite half-space and measuring directly or indirectly the contact area. The nanoindenter can give as output reduced modulus and hardness values.

1.2 Osteogenesis Imperfecta

Osteogenesis imperfecta (OI) is a heterogeneous group of inherited disorders of bone formation (6-7 in 100.000 births), resulting in low bone mass and an increased propensity to fracture. Other manifestations include blue-grey sclerae, joint hypermobility, hearing loss, dentinogenesis imperfecta, and short stature. It is a variable condition with a range of clinical severity [11].

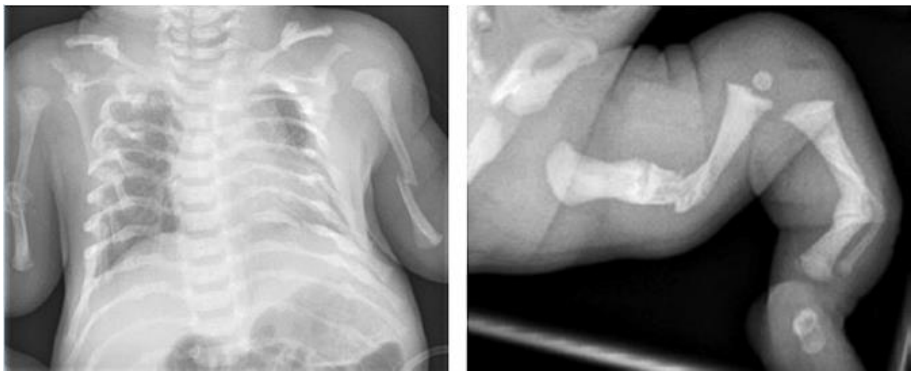

Figure 9: Radiographs of an OI child [12]

Previously, osteogenesis imperfecta was known as an autosomal dominant disorder caused by mutations in COL1A1 and COL1A2, coding for the α1(I) and α2(I) chains of type I collagen, the most abundant protein of bone, skin and tendon. Although about 85–90% of cases are caused by structural or quantitative mutations in the collagen genes themselves, the disorder is now more fully understood as a predominantly collagen-related disorder.

Seven recessive forms are caused by defects in genes whose protein products interact with collagen for folding or post-translational modifications. Two other rare defects mainly affect bone mineralisation, but also decrease collagen production.

Figure 10: Imaging at 4.5 years of age demonstrating the face and significant limb deformities [12]

The most common structural defects in type I collagen causing osteogenesis imperfecta are glycine substitutions in the helical domain (as shown in the Fig.11). Glycine substitutions delay helical folding, prolonging access time for modifying enzymes [11].

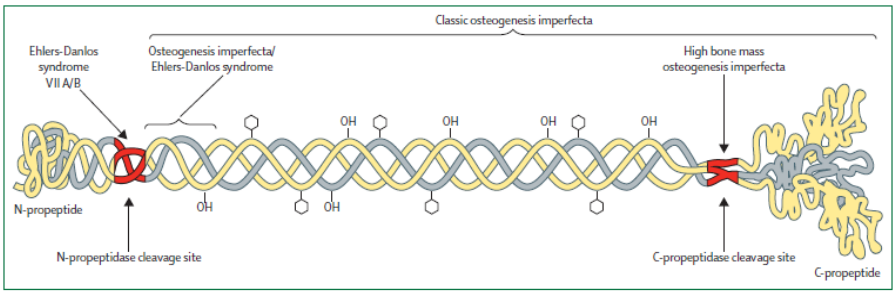

Figure 11: Mutations in specific positions along type I procollagen molecule cause distinct clinical phenotypes [11]

In general, glycine substitutions near the carboxyl-terminal end appear to result in the severest phenotype. Collagen with a primary structural defect has more severe consequences for intracellular metabolism and matrix structure than does a reduced amount of normal collagen [11]. Most mutations causing more severe OI result from the substitution of glycine by another amino acid that disrupts tight coiling of the triple helix, delaying the process and allowing additional posttranslational modification of the collagen molecules to take place, distorting its 3D structure [13].

The classification evolved with the new genetic discoveries. The 1979 Sillence classification divided osteogenesis imperfecta into four types (based on symptoms/prognosys), from mild to lethal, based on clinical and radiographic features. Identification of collagen defects showed that mild Sillence type I was related to quantitative deficiency of structurally normal collagen, whereas lethal (type II), severe (type III), and moderate (type IV) forms had mutations altering collagen structure [11]. At the 2009 meeting of the International Nomenclature group for Constitutional Disorders ICHG of the Skeleton (INCDS) (Published as 2010 Nosology), a decision was finally made to group the known OI syndromes into five groups (adding OI type V). The importance of the different genetic causes of the OI types was acknowledged by encapsulating the causative genes as subtypes of OI types I–V (Table 1) [14].

TABLE I. A New OI Nomenclature Combined With Causative Genes (A) Phenotypes With Mild to Moderate Severity, (B) Progressively Deforming and Perinatally Lethal Phenotypes

OI syndrome names	Type	Gene	MIM	Locus	Protein product	Inheritance
(A)						
Non-deforming OI with blue sclerae	1	1. *COL1A1*	#166200	17q21.33	Collagen alpha-1(I) chain	AD
		2. *COL1A2*	#166200	7q22.3	Collagen alpha-2(I) chain	AD
Common variable OI with normal sclerae	4	1. *COL1A1*	#166220	17q21.33	Collagen alpha-1(I) chain	AD
		2. *COL1A2*	#166220	7q22.3	Collagen alpha-2(I) chain	AD
		3. *WNT1*[a]	#615220	12q13.12	Wingless-type MMTV integration site family, member 1	AD
					Cartilage-associated protein (CRTAP)	
		1. *CRTAP*	#610682	3p22.3	Cyclophilin B (CyPB)	AR
		2. *PPIB*	#259440	15q22.31	Osterix	AR
		3. *SP7*	#613849	12q13.13	Plastin 3	AR
		1. *PLS3*		Xq23		XL
OI with calcification in interosseous membranes	5	1. *IFITM5*	#610967	11p15.5	Interferon-induced transmembrane protein 5	AD
(B)						
Progressively deforming	3	1. *COL1A1*	#259420	17q21.33	Collagen alpha-1(I) chain	AD
		2. *COL1A2*	#259420	7q22.3	Collagen alpha-2(I) chain	AD
		1. *BMP1*	#614856	8p21.3	Bonemorphogeneticprotein 1	AR
		2. *CRTAP*	#610682	3p22.3	Cartilage-associatedprotein (CRTAP)	AR
		3. *FKBP10*	#610968	17q21.2	Peptidyl-prolyl cis-transisomerase FKBP10	AR
		4. *LEPRE1*	#610915	1p34.2	Prolyl 3-hydroxylase 1 (P3H1)	AR
		5. *PLOD2*	#609220	3q24	Procollagen-lysine, 2-oxoglutarate	AR
		6. *PPIB*	#259440	15q22.31	5-dioxygenase 2	AR
		7. *SERPINF1*	#613982	17p13.3	Cyclophilin B (CyPB)	AR
		8. *SERPINH1*	#613848	11q13.5	Pigment-epithelium-derived factor (PEDF)	AR
		9. *TMEM38B*	#615066	9q31.1	Heat shock protein 47 (HSP47)	AR
		10.*WNT1*	#615220	12q13.12	Trimeric intracellular cation channel B (TRIC-B)	AR
		11.*CREB3L1*		11q11	Wingless-type MMTV integration site family, member 1	AR
					Old Astrocyte Specifically induced substance (OASIS)	AR
Perinatally lethal OI	2[b]	1. *COL1A1*	#166220	17q21.33	Collagen alpha-1(I) chain	AD
		2. *COL1A2*	#166220	7q22.3	Collagen alpha-2(I) chain	AD
		1. *CRTAP*	#610682	3p22.3	Cartilage-associated protein (CRTAP)	AR
		2. *LEPRE1*	#610915	1p34.2	Prolyl 3-hydroxylase 1 (P3H1)	AR
		3. *PPIB*	#259440	15q22.31	Cyclophilin B (CyPB)	AR

So far, 12 families with AR OI due to *WNT1* mutations have been described. Developmental delay was reported in affected individuals from three families. It is uncertain whether this is part of the clinical phenotype resulting from *WNT1* mutations [Fahiminiya et al., 2013; Keupp et al., 2013; Pyott et al., 2013]. A dominant *WNT1* mutation appeared to cause early onset osteoporosis [Keupp et al., 2013; Laine et al., 2013].

In clinical practice subdivisions OI type II-A and OI type II-B are still in use. OI type II-A appears to be exclusively caused by heterozygous mutations in the *COL1A1/2* genes [van Dijk et al., 2010]. It has been reported that mutations in *PLOD2* may also result in progressively deforming OI [Puig-Hervás et al., 2012].

Although the INCDS agreed to retain the Sillence classification as "the prototypic and universally accepted way to classify the degree of severity in OI", the need for internationally agreed criteria for grading severity between affected individuals was proposed and adopted, reflecting also the improved treatment possibilities (surgical, pharmacological and conservative) for patients with OI [15].

Bone is a collagen-hydroxyapatite composite where the collagen fibres are high deformable and tenacious, and the hydroxyapatite crystals give stiffness to the tissue, but they make it brittle. The mineral crystals have the same orientation of the collagen fibres and they are also within the collagen fibrils [3]. The key feature that discriminates OI from other early-onset bone fragility conditions is the hyper mineralization of the bone material itself, although increased mineralization density is not the only contributor to brittleness [13]. The single most important clinical feature of the OI bone is the propensity to fractures throughout life. Another feature could be the significantly reduced bone density in at least one area of the skeleton [16]. Net bone fragility is the result of contributions from primary bone fragility and the secondary fragility resulting from osteoporosis. Osteoporosis develops in most patients with OI. The finding of elevated serum and urine markers of bone turnover in patients with OI is best explained by a combination of increased bone formation and increased bone resorption. The net effect is a small progressive bone loss since bone resorption is often greater than bone formation, with immobilization also exerting a negative effect on bone formation [17].

1.2.1 Osteogenesis Imperfecta Types

OI type I is characterized by increased bone fragility, which is usually associated with low bone mass, distinctly blue-grey sclerae, and susceptibility to conductive hearing loss commencing in adolescence and young adult life. OI type I and IV are the most common varieties of OI in European communities and have a birth prevalence in the order of 4-5 in 100.000 births [18]. Hearing impairment resulting from both conductive and sensorineural loss is detectable in over 50% of patients with OI type I by 40 years of age. Vertigo is a troublesome symptom in many people with OI [19].

In OI type II the skeletal, joint, and extra skeletal features of this group of foetuses and children are extremely severe (1-2:100.000 births). Foetuses detected at 18–20 weeks

gestation have short crumpled long bones, bowing or angulation deformities of long bones and marked deficiency of ossification of facial and skull bones [16]. At this early gestation, there may be few rib fractures but with each month in utero there is progressive fracturing of ribs resulting in the continuously beaded appearance combined with crumpled (accordion-like) long bones that is the characteristic of the extremely severe end of the spectrum represented by OI type II. The thighs are held abducted and in external rotation. The chest is small for gestation and respiratory excursion may be depressed because of the pain from multiple rib fractures and the abnormal biomechanical properties of semi continuous beading from fracture callus along each rib in the most severely affected. Several clinical features suggest that new-borns with OI type II are in constant pain. They may have excessive perspiration, pallor, show anxiety at being touched and move their limbs very little because of multiple fractures. One-fifth are stillborn and 90% die by 4 weeks of age [16].

Individuals with OI type III usually have new born or infant presentation with bone fragility and multiple fractures leading to individuals with progressive deformity of the skeleton (1-2:100.000 births). They are generally born at or near term and have normal birth weight and often normal birth length, although this may be reduced because of deformities of the lower limbs at birth. Although the sclerae may be blue at birth, observation of many patients with this syndrome documents that the sclerae become progressively less blue with age [20]. In the past, approximately two-thirds of the patients died by the end of the second decade. Death usually resulted from the complications of skeletal chest wall deformity including kyphoscoliosis, pulmonary hypertension, and cardio-respiratory failure. With the present therapeutic options, it can be expected that today most patients with OI type III will survive into adult life. A publication (Alcausin et al.,2013) confirmed that treatment appears to be well tolerated and associated with an increase in bone density, reduced fracture frequency and improved vertebral shape [15].

OI type IV is the most variable form of the condition with symptoms ranging from moderately severe to so mild that it may be difficult to make the diagnosis. These patients have recurrent fractures, osteoporosis and variable degrees of deformity of long bones and spine but normal sclerae. The sclerae may be bluish at birth but the blue tinge fades during childhood. Hearing impairment is not often encountered [17].

In OI type V (<1:100.000 births) calcification of the inter-osseous membrane in the forearms is observed from early in life, which leads to restriction of pronation and

supination, and eventual dislocation of the radial heads. The sclerae are white. Those affected tend to have higher serum alkaline phosphatase values and have an increased risk of developing hyperplastic callus following a fracture or orthopaedic surgery [17].

While propensity to fractures throughout life is the single most important clinical feature, experience with families with OI type I indicate that perhaps 10% of affected individuals have not had a long bone fracture during childhood.

Skeletal deformities such as scoliosis and basilar impression are regarded as secondary deformations rather than primary malformations. Although the absence of deformity of long bones has been advanced as a diagnostic criterion, the presence of deformity seems at least partly significantly influenced by quality of care [15].

The initial diagnosis of OI is largely based on clinical and radiographic findings. Fractures from mild trauma, bowing deformities of long bones, and growth deficiency are the hallmark features. When possible, clinicians should do a full screen of osteogenesis imperfecta causative genes and identify carrier status or presence of second mutations to understand the complexity of the disorder rather than stopping the investigation when the first plausible mutation is identified [11].

1.2.2 Treatments

The treatments currently used for this type of pathology are many:
Bisphosphonate treatment aims to reduce the osteoclast activity and it has become the gold standard for treatment of children with moderate to severe OI [15]. Bisphosphonate therapy may be more effective in children than in adults because it has differential effects upon modelling and remodelling bone (the effects may be different in a growing skeleton (with both modelling and remodelling) compared with a mature skeleton (that under goes remodelling only)) [21]. Studies in adults with OI without recent fracture show increased bone resorption markers and markers of osteoblast function [22]. These results suggest that OI is a high turnover disease with increased osteoclast and osteoblast activity but decreased synthesis of collagen although non-collagenous protein secretion may be unaffected. The use of bisphosphonates, therefore, in adults and children with OI type I might potentially have a deleterious effect on bone strength, by further reducing synthesis of type I collagen through suppression of osteoblasts. The effect of this on bone fragility is not known [23].

In patients with less severe OI (type I), *Teriparatide* (a pharmacological treatment based on the injection of the Parathyroid Hormone, PTH) resulted in increased markers of bone formation, accompanied by increases in proximal femur of BMD (bone mineral density). Although bisphosphonates appear to increase BMD in adults with OI, they reduce bone remodelling and bone formation, actions that may be problematic in the presence of underlying defects in bone formation and osteoblastic function. This suggests that the combination therapy with teriparatide and bisphosphonates may be useful [24].

1.2.3 Mechanical properties of OI bone

Much of the studies about mechanical properties in OI have been undertaken using the *oim* mouse model. The mice have a moderately severe OI phenotype; they are smaller at birth and grow less well than wild-type littermates, have low bone mass, fracture with minimal trauma, and develop bone deformities. At a tissue level, cortical thinning and reductions in trabecular number are observed on light microscopy, along with a lack of lamellar architecture and increased osteocyte density. The bone matrix compressive elastic modulus of *oim* tibia by nanoindentation was reduced by 20% compared with wild type. The overall picture that emerges from the mouse model reports is of a disorganized bone matrix, more loosely woven, less capable of responding to normal mechanical inputs, and less able to absorb and dissipate energy that might lead to fracture [13].

Fracture resistance is difficult to measure *in vivo*. A novel approach using microindentation has been developed that provides information on the ability of bone to resist a localized fracture. When a long OI bone breaks, the fracture line tends to be transverse, suggesting that some of the mechanisms that normally promote energy dissipation are abrogated. At lower scale lengths in OI, multiple factors likely interact to reduce the ability of the disorganized matrix to effectively absorb or dissipate fracture-causing energy. Vanleene at al. (2012) used the *oim* model, in which the mice do not express col1-a2 protein and have homotrimer collagen1-(a1) instead of the normal heterotrimeric helix. These mice have extreme bone fragility, mimicking moderate to severe OI in humans [25]. At the microscopic (matrix) scale, *oim* bone is mostly composed of woven tissue with unorganized collagen fibres, a high mineral/protein content ratio and a high porosity. *Oim* bone apatite crystals are small and not well aligned and their crystallinity and chemical composition is altered [26].

Their results showed that the elastic modulus (measured with nanoindentation tests) was not significantly different between *oim* and wild type animals (6.99 ± 1.18 GPa vs 6.95 ± 0.75 GPa) while the ultimate stress (σ_{ult}) was lower in *oim* mice compared to wild type mice (90.0 ± 34.6 MPa vs 122.9 ± 8.6 MPa). At the macroscopic scale, *oim* bone was weak (decrease of σ_{ult}) and brittle (little post-yield deformation). In addition, the whole bone estimates of modulus include the effects of porosity, which is significantly increased in *oim*, thereby providing an overall modulus that includes the matrix and the voids. For a same amount of energy dissipated during a load, while the wild type bone matrix remains in the elastic domain, the *oim* bone matrix will reach the plastic domain where its higher resistance does not allow further plastic deformation, triggering the catastrophic fracture of the bone and explaining the increased bone brittleness.

Vanleene et al. did not observe correlation between the bone mineralization and stiffness at the microscopic scale either in the *oim* or in the wild type mice. This has important implications in bone pathologies and the therapeutic strategies developed to counter their effects. Therapies that promote apposition and accumulation of hyper-mineralized bone tissue, may have the limitation of accumulating bone with poor structural and mechanical properties with possible long-term negative effects [25].

1.3 Characterization of the tissue properties with Nanoindentation

1.3.1 Theory

The macroscopic mechanical properties of bones are determined by composition as well as nanostructural (lamella), microstructural (osteon/trabecular packet) and structural (cortical/trabecular) organization. Several micromechanical models with increasing sophistication have been proposed to quantify the relationship between composition, hierarchical organization and macroscopic mechanical properties [27].

Indentation consists in pressing a hard tip with a known force into a semi-infinite half-space and measuring directly or indirectly the contact area. In the classical hardness test performed at the macroscopic or microscopic level the contact area is estimated optically from the imprint created by the tip on the material and leads to the definition of hardness as the force

divided by this area. Nanoindentation is an evolution of the conventional hardness test for assessment of the mechanical properties of thin films and surface layers. This technique reduces the depth of indentation to submicron range, extends the spatial resolution to about 1 μm and allows for estimation of the local elastic modulus under specific assumptions and careful calibration. Recent depth-sensing technologies allow for measurement of the tip displacement during the indentation process of a semi-infinite half-space with micro- and even nanoprecision. Indirect estimation of the contact area is obtained by preliminary calibration of the tip shape and system compliance. Shallow indentation depths down to 100 nm allow for spatial resolution of the measurements in the micron range, and the specimen position is typically controlled by high-precision motorized tables or piezoelectric scanners [4]. In recent years, nanoindentation has emerged as a powerful technique for investigating the micromechanical properties of bone. This technique allows the decoupling at the microscopic scale of the mechanical properties in multiple directions [28].

Critical assumptions of this technique are:

- The constitutive behaviour of the specimen is elastic with time-independent plasticity;
- The solution for the elastic deformation of an irreversibly indented surface geometry is like the one of a flat semi-infinite half space;
- The Poisson ratio ν of the specimen is known.

With the possibility to evaluate elastic and plastic deformation at the tissue level, micro-indentation is an attractive technique to evaluate to which extent microdamage is associated with tissue mechanical properties. Micro- and nanoindentation tips are often made of black diamond and can be found in spherical, conical, and most commonly, three-sided pyramidal (Berkovich) shapes [4].

Spherical tips minimize plastic deformation and damage but are difficult to manufacture, flat punches lead to high stress concentrations, conical tips have an axial symmetry that remains in the assumption of most theoretical contact models, and Berkovich tips are the easiest to manufacture and resemble conical tips [29].

A Berkovich tip (Fig.12), used in this project, is a three-sided pyramid which is geometrically self-similar. The popular Berkovich has a very flat profile, with a total included angle of 142.3 degrees and a half angle of 65.27 degrees, measured from the axis to one of the pyramid flats. The original tip shape was invented by Russian scientist *E.S.*

Berkovich in the USSR c. 1950, which has a half angle of 65.03 degrees. It is typically used to measure bulk materials and films greater than 100 nanometres (3.9×10−6 in) thick [30].

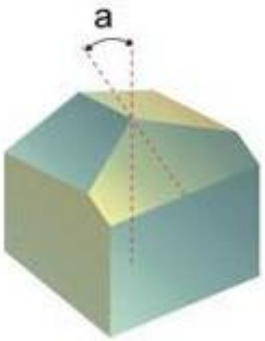

Figure 12: Berkovich tip [30]

The theoretical basis of the method relies on the Boussinesq solution of indentation of an elastic half-space by a rigid, axisymmetric indenter derived by Sneddon [31]. The relationship between contact stiffness and the elastic properties of the specimen is shown in the below equation:

$$\frac{dP}{dh} = \frac{2}{\sqrt{\pi}} \sqrt{A} \frac{E_b}{(1-\nu_b^2)} \tag{1}$$

where P is the load, h is the penetration depth, A is the projected contact area of the indenter as a function of depth h, E_b is the elastic modulus and ν_b is the Poisson ratio of the specimen. Application of this solution to the unloading procedure of nanoindentation with a deformable pyramidal Berkovich tip was then proposed by Oliver and Pharr (1992). The relationship between contact stiffness and the elastic properties of the specimen becomes:

$$\frac{dP}{dh} = \beta \frac{2}{\sqrt{\pi}} \sqrt{A}\, E_r \tag{2}$$

where β is an empirical indenter shape factor and the reduced modulus E_r is given by

$$\frac{1}{E_r} = \frac{(1-\nu_b^2)}{E_b} + \frac{(1-\nu_i^2)}{E_i} \tag{3}$$

with the indices *i* and *b* corresponding to the indenter and the specimen, respectively [31].

Nanoindentations measure the resistance to penetration, which is a property of the material. This information must be linked to an elastic module. There are three modulus definitions:

- Reduced modulus E_r
- Indentation modulus E_{ind}
- Elastic modulus of the specimen E_b

The reduced modulus is obtained from the indentation curve and it concerns the indentation made in that material in that particular position. The definition of the reduced modulus is:

$$E_r = \frac{\sqrt{\pi}}{2\beta\sqrt{A_c}} \frac{dP}{dh} \tag{4}$$

where β is an empirical indenter shape factor, A_c is the indentation projected area and dP/dh is the slope of the curve P-h in h_{max}. E_r evaluates stiffness, but according to the geometry of that indentation.

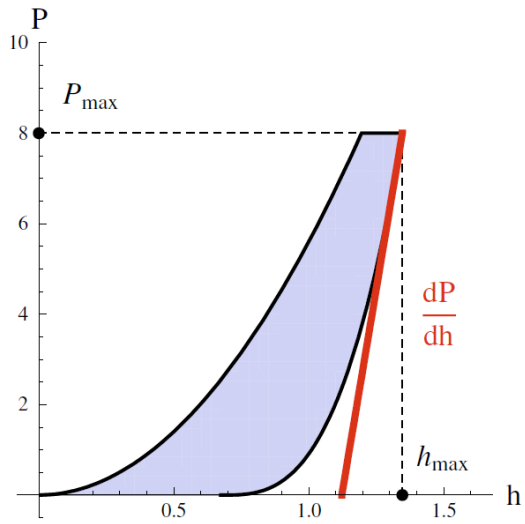

Figure 13: Indentation curve with the unloading stiffness and the dissipated energy [4]

Indentation modulus: although the indenter is much stiffer than the material, the tip is slightly deformed during the indentation, and this will partially influence the curve P-h. The indentation modulus is obtained from this equation:

$$\frac{1}{E_r} = \frac{1-\nu_i^2}{E_i} + \frac{1-\nu_t^2}{E_t} \quad (5)$$

where E_t and ν_t are the elastic modulus and the Poisson ration of the tip, respectively. E_i is obtained from the previous equation and it still depends on the material and on the indentation location. To compute the elastic modulus, we must consider the intrinsic properties of the material, so we make the big assumption that the material is locally isotropic. We should use the following equation to obtain the specimen elastic modulus E_b:

$$E_b = \frac{\left(1-\nu_b^2\right) E_r\, E_i}{E_i - E_r\,(1-\nu_i^2)} \quad (6)$$

For the indentation of isotropic materials, the Oliver-Pharr method can predict intrinsic material properties, such as Young modulus, within 4% of literature values. For anisotropic materials, the indentation modulus represents a weighted average quantity, as the formation of the contact impression involves deformation in all three principal directions. Therefore, the modulus is not easily interpreted by conventional methods [32].

While the reduced modulus represents the elastic behaviour of the tissue, the hardness is related to failure mechanisms such as slippage at the collagen–mineral interface, phase transformation of the mineral phase and sacrificial bond disruption between fibrils that determine its inelastic deformation. As the hardness of the tissue is less anisotropic than its reduced modulus, there is evidence that these inelastic phenomena contribute to a reduction in the anisotropy in the failure behaviour compared with the elastic behaviour [33]. Hardness was generally found to be homogeneous, but along a long bone, hardness tended to be higher in the diaphysis than in the metaphysis and epiphysis. Hardness of trabecular bone was shown to be somewhat lower (10–15%) than the interstitial bone of the adjacent cortex. Hardness was found to correlate with mineralization. More specifically, microhardness was found to be 20–25% higher along collagen fibre orientation than across. The difference in hardness did therefore not depend exclusively on the degree of calcification but also on the arrangement of the collagen fibres [4].

For all methods, the tip shape and indentation depth define the volume of material participating in the mechanical response. According to Hertz theory, the extent of this volume is approximately nine times the indentation depth along the loading axis and seven

times along the radial direction. The region of interest determines therefore the selected depth of indentation [29]. The nanoindentation technique could be used to investigate the behaviour of packages of lamellae (penetration depth is >1.5μm) or single lamella (penetration depth is <1μm). In this project we investigated the behaviour of a single lamella.

The storage of the specimens may have an important effect on its mechanical characterization. The gold standard for mechanical testing of bone tissue is fresh but freezing was found to have a minimal impact on indentation results. Dehydration in ethanol increased hardness by 10% and indentation modulus by 15–20%. Nevertheless, due to the rapid evaporation of water at the bone surface, the use of a liquid cell where the specimen is fully submerged during indentation seemed to give the most reliable results provided a calcium phosphate buffer solution is used to prevent superficial demineralization [4].

Controlling environmental conditions, including humidity and temperature, interferes with the stability of most nanoindentation systems. More importantly, nanoindentation is a measurement performed on such a fine scale that its accuracy is affected by minimal disturbances at the surface or near surface of the specimen. This includes surface roughness, swelling, leaching of bone mineral or formation/precipitation of mineral salts when the specimen is immersed in solution, or even a thin film of water that, through capillary forces, may prematurely pull the indenter tip into the specimen surface prior to the start of the test. Many of these factors may have a negligible effect in larger scale mechanical testing but are fundamental to control in nanoindentation tests [34].

1.3.2 Nanoindentation on human bone tissue

Nanoindentation tests on human bone are conducted to investigate different mechanical properties of the bone, such as the elastic modulus or the hardness. Zioupos et al. showed that micro-indentation is used to evaluate the elastic properties of bone structural units (BSUs) in both trabecular and cortical sites. This technique has been used *in vitro* to evaluate variations among different anatomical sites, the effect of pathologies on the mechanical properties of BSUs, the bone matrix quality close to implants and the effect of tissue condition (hydrated, dried or embedded) during the test [35]. The isotropic and anisotropic indentation analyses can be used for moderately rate-dependent (viscoelastic and/or viscoplastic) materials such as bone. For that reason, a typical micro- or nano-indentation

experiment consists in a loading ramp with constant load rate followed by a holding period (5–120 s) at constant load and an unloading ramp [36].

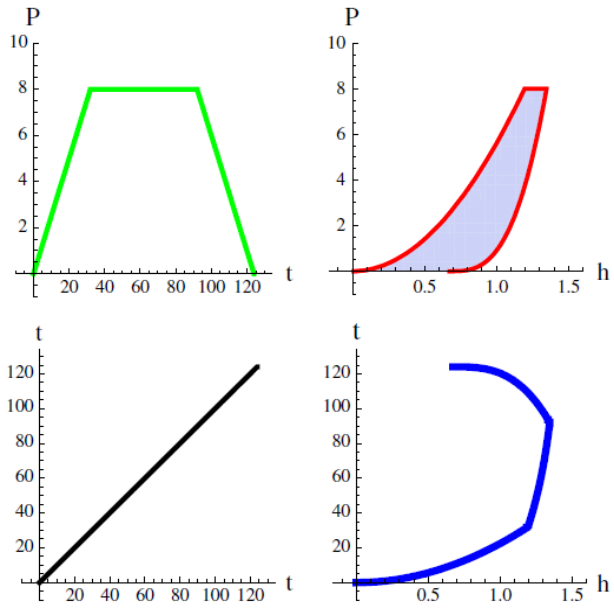

Figure 14: A typical load-controlled indentation schedule with the resulting displacement of the tip. P is the applied force, h is the penetration depth and t is the time [4]

Zysset et al. (1999) quantified the elastic modulus and hardness of human femurs at the lamellar level (penetration depth: 500 nm). They performed the nanoindentations on rehydrated tissue. The definition of hardness was the mean pressure under the indenter at maximal depth and they calculated the parameters according to the previous equations (Eqs. (2), (3)). They found that the mechanical properties of trabecular bone were significantly lower than those of cortical bone. They showed that the elastic modulus of human femur tissue depended strongly on tissue type anatomical location and individual. The average elastic moduli of cortical and trabecular bone measured by nanoindentation were 20.1 ± 5.4 GPa and 11.4 ± 5.6 GPa, respectively [31]. In Figs.15-16, the nanoindentations on the bone and a typical load-displacement curve for both cortical and trabecular bone (obtained from the nanoindentation software) are reported.

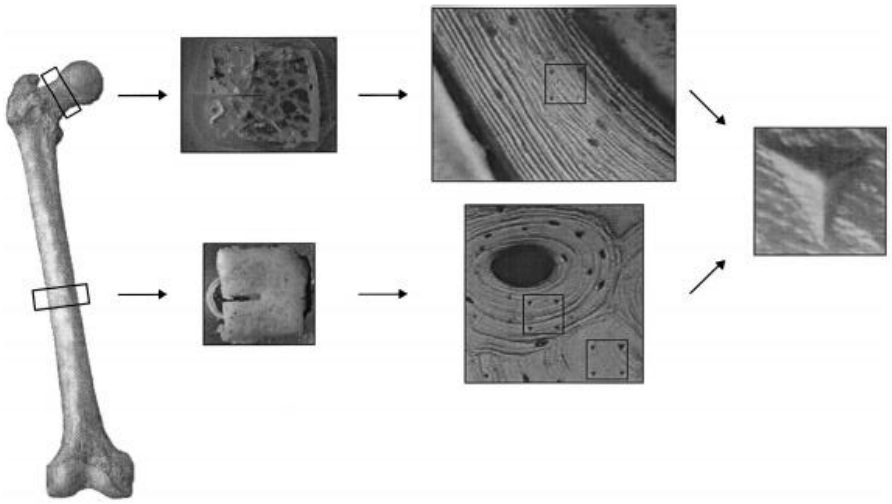

Figure 15: Indentations were made in osteonal, interstizial or trabecular lamellae from the diaphysis and the neck [31]

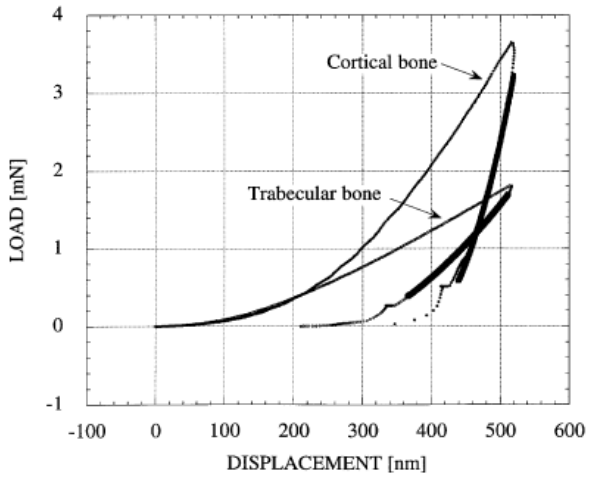

Figure 16: Typical force-displacement curves on human bone [31]

For deeper indentation, multiple lamellae were involved in the deformation mechanism. Wet lamella was substantially more compliant than dry ones, but a quantitative comparison cannot really be made, since distinct BSUs were evaluated [31]

Micro-indentation on human bone can discriminate also between damaged and intact bone tissue. For example, Dall'Ara et al. (2012) found significant differences for E_{ind} and H between damaged and intact regions. They performed their tests in wet conditions and the penetration depth was 2.5 µm. They found that E_{ind} of the intact trabecular bone in the axial direction (11.4 ± 4.3 GPa) was 16% lower than the intact interstitial bone (13.2 ± 4.4 GPa) but not significantly different than the intact osteonal bone (10.9 ± 3.8 GPa).

The ability of micro-indentation to detect the reduced mechanical properties in damaged bone, is probably due to the lower tissue resistance against the local pressure induced by the indenter when microcracks are present underneath the bone surface. The positive interaction between damage and structure showed that the reduction of mechanical properties affected trabecular bone slightly more than the cortical bone. Probably, this difference is due to the more compliant trabecular arrangement compared to the stiffer cortical shell during the macro-mechanical testing (i.e. before embedding). However, severe damage seems to reduce by 45–55% both hardness and indentation moduli of the different BSUs. The larger difference between interstitial and osteonal tissues might be due to the different indentation level (bone structural unit vs lamellae), different anatomical site and the different methodology of hydration of the specimens during the test (submerged vs irrigated) [37].

Then, in a subsequent study of Dall'Ara et al. (2013), they investigated the anisotropic indentation moduli of the cortical shell, endplate, trabecular centrum and spondylophytes in the human vertebral body. Their nanoindentations were performed on rehydrated tissues and the penetration depth was 2.5 μm. The results showed that the cortical shell was systematically stiffer along the axial direction (14.6 ± 2.8 GPa) compared to the circumferential (12.3 ± 3.5 GPa, 16%) and radial (8.3 ± 3.1 GPa, 43%) ones. Moreover, E_{ind} along circumferential direction was 32% higher than E_{ind} along the radial one. In that study the cortical shell was found to behave as an orthotropic material with different mechanical properties along axial, circumferential and radial directions. Similar conclusion can be drawn for trabecular bone that showed a transverse isotropic behaviour with properties along axial and circumferential direction only slightly lower than the ones of the cortical shell [38].

The fibril organization in bone lamellae is supposed to dictate the degree of anisotropy of osteons. Predominately longitudinally aligned fibrils lead to osteons that are strong in tension and mainly transverse fibrils to good compression capabilities. Oblique fibril angles could result in a main stiffness alignment that possesses a helical winding around the osteon, inducing a spring-like deformation mechanism under axial load (Fig.17). A completely different point of view suggests that the bone mineral particle orientation is mainly axial and largely independent of the collagen organization. This mineral alignment is supposed to play the dominant role for bone anisotropy. To shed more light on this issue, detailed measurements of the anisotropic elastic properties of osteons must be related to the

underlying fibril orientation patterns. Such measurements are difficult to perform as they must be applied in multiple directions relative to the osteon lamella plane.

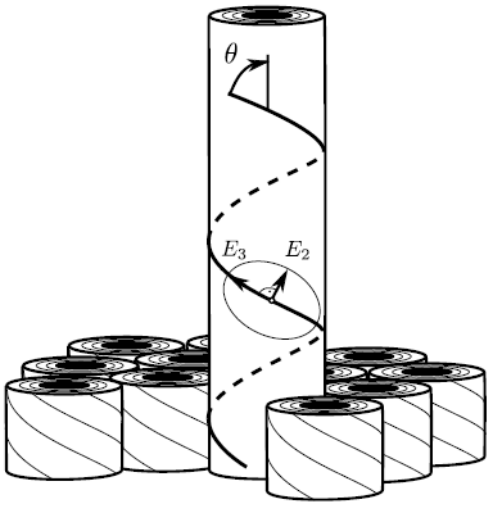

Figure 17: Helix shaped alignment of the main principal material axis around the haversian channel in the ideal cylindrical osteon. With ϑ being the helix angle and E3 and E2 being the Young's modules in the major and minor principal axis of the lamella assembly material, respectively [39]

The two indentation directions (axial and circumferential) are enough to estimate the degree of anisotropy of osteons but not a potential helical winding of the main stiffness direction. The lamella assembly-material is considered as the homogenized material of 7–10 osteon lamellae and this number of lamellae could be covered by the 50 μm long nanoindentation patterns. From this point of view, the study performed by Reisinger et al. (2011) showed that osteons are generally stiffer in longitudinal than in circumferential direction. They performed the tests in wet conditions and the penetration depth was 250 nm. The direction of maximum stiffness is slightly rotated relative to the osteon axis leading to an evident but moderate helical winding. This outcome contradicts the widely known 'twisted plywood' collagen fibril orientation pattern in lamellar bone that would lead to a more isotropic behaviour. Additionally, the often-reported transverse osteons, holding a mainly transverse fibril orientation, were not observed from the mechanical point of view [39].

Another aspect was investigated by Spiesz et al. (2013). They performed indentations on dehydrated tissue and the penetration depth was 500 nm. They compared the results from measurements performed in the osteonal and interstitial regions. The values of E_{ind} in the osteonal and interstitial tissues were 24.22 ± 4.80 GPa and 23.66 ± 5.56 GPa, respectively. The significant difference in mineralization between the osteonal and

interstitial regions is attributed to the local age of the tissue. In the ongoing mineralization process, the younger osteons are less mineralized compared to the older interstitial regions. In this study, the results suggest that the variation of indentation modulus among lamellar bone structural units cannot be explained by mineral mass fraction and mean collagen orientation, which points towards the role of the other factors such as nano-porosity, damage, collagen cross-linking and no collagenous proteins [40].

These studies are focused on many possible applications of nanoindentation techniques for the study of the mechanical properties of human bone tissue. It has been shown how nanoindentation can be used to investigate the difference between cortical and trabecular bone, the dependence of the mechanical properties on the anatomical sites, the difference between damaged and intact regions or the degree of anisotropy of osteons.

1.3.3 Nanoindentation on mouse bone tissue

Many insights into the biology and biomechanics of bone tissue at multiple hierarchical levels have emerged from animal experiments. Rodent models are of prime importance as they are inexpensive, easy to breed and a relatively high number of animals can be bred concurrently. Moreover, inbred rodents have negligible genetic variation, which drastically reduces biological variance. Mouse models can be used for gene targeting technologies and antibody-mediated suppression of protein functions, which are crucial for investigating the genetic fingerprint of bone cells expression. Rodent bone does not present an osteonal structural organization, but their collagen fibres are also mainly oriented in an axial direction in their long bones. Although mouse cortical bone does not present an osteonal structure, microcracks have also been shown to occur in rodents, and to form preferentially along longitudinal canals [41].

Casanova et al. (2017) for example, made the nanoindentation experiments along the transverse and longitudinal direction on the proximal, central and distal locations in the mouse femoral shaft. They performed their nanoindentations on rehydrated bone tissue and the penetration depth was 500 nm. Two examples of indentation curves along the longitudinal and transverse direction are reported in Fig.18. Mean results for reduced modulus of the set of six indents for the transverse and longitudinal directions ranged between 6.75 ± 0.50 GPa (transverse direction, proximal region) and 23.81 ± 2.47 GPa

(longitudinal direction, proximal region). Mean hardness for the set of six indents along transverse and longitudinal directions ranged between 0.38 ± 0.068 GPa (transverse direction, central region) and 0.82 ± 0.092 GPa (longitudinal, proximal region).

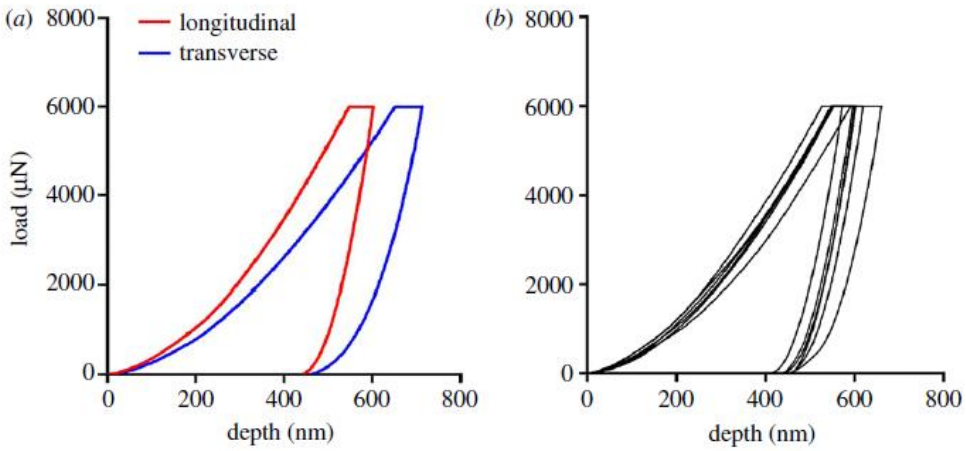

Figure 18: (a) Representative indentation curves along the longitudinal and transverse directions in the central regions of specimen (left leg). (b) Load–depth curves obtained for the six indents along the longitudinal direction in the proximal region on the right [42]

Casanova et al. observed significant differences between the longitudinal and the transverse direction for both reduced modulus and hardness. There was no correlation between longitudinal and transverse directions for either reduced modulus or hardness. It is hypothesized that the collagen fibres tend to structure themselves in bundles which might be cemented together owing to non-collagenous proteins. Therefore, the larger variability in mechanical responses when indenting perpendicularly to them might be because of the presence of a less heterogeneous structure in the transverse compared with the longitudinal direction [42].

1.3.4 Nanoindentation on bovine bone tissue

Bovine bone is usually used to characterize bone properties because it has characteristics similar to human bone. For example, Lucchini et al. (2011) conducted indentation tests on bovine dehydrated osteonal bone. The maximum depths were between 50 and 450 nm. Tests involved four different osteons in both the axial and the transverse directions (Fig.19).

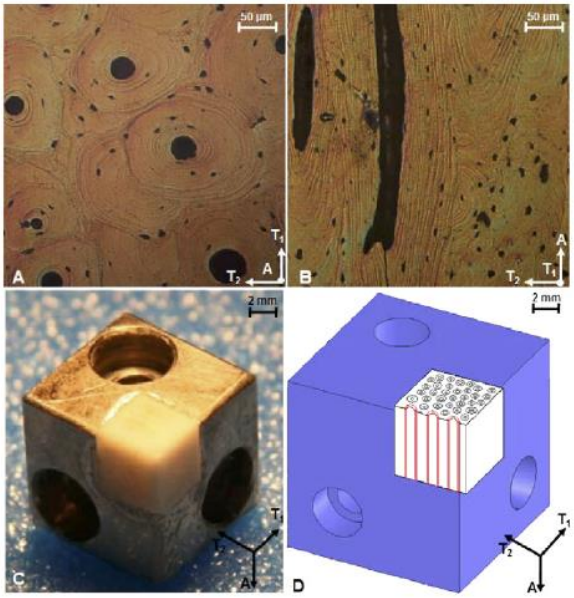

Figure 19: (A) axial section (cut perpendicularly to the long axis of bone); (B) transverse section (cut parallel to the long axis of bone). (C) Home-built specimen preparation stage designed to test two orthogonal orientations on the same osteon. (D) Sketch of the indentation test directions with respect to the tissue microstructure; individual osteons with the sliced Haversian canals are the ones where nanoindentation testing was performed [43]

They also reported the curves (Fig.20) that show how the indentation response of the tissue depends on the orientation direction. The pronounced hysteresis of the loading–unloading cycles indicates the arising of a dissipative inelastic material behaviour during testing.

A decrease in the indentation moduli mean values was observed between 50 and 450 nm maximum depths; this decrease was more pronounced along the transverse direction (from 23.02 ± 3.48 GPa to 16.41 ± 1.71 GPa, 29% reduction) than in the axial direction (from 28.15 ± 3.47 GPa to 22.30 ± 1.78 GPa, 21% reduction) direction. A similar trend has been found in terms of tissue hardness which varies from 1.02 ± 0.22 GPa to 0.73 ± 0.04 GPa along the axial direction and from 0.92 ± 0.18 GPa to 0.61 ± 0.09 GPa along the transverse direction [43].

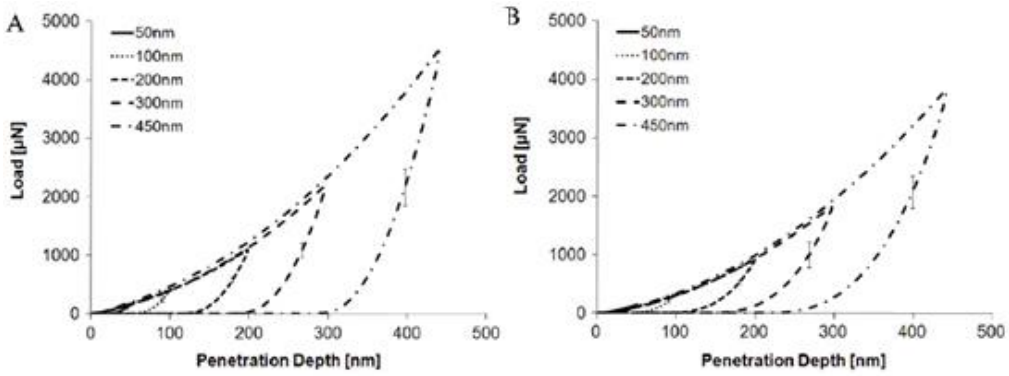

Figure 20: Averaged force vs. penetration depth nanoindentation data for bovine cortical bone tissue in the osteonal region along the axial (A) and transverse (B) directions at the five tested maximum depths [43]

Another application is shown in the work of Carnelli et al. (2013) where the nanoindentations were performed on the secondary osteons of bovine cortical bone (dehydrated tissue). Experiments were carried out in two orthogonal orientations within the same individual osteon at four different maximum penetration depths. The average loading/unloading indentation curves obtained in the two orthogonal directions at the four maximum penetration depths are reported in Fig.21. The curves show how the indentation response of the tissue depends on the global orientation direction (axial versus transverse).

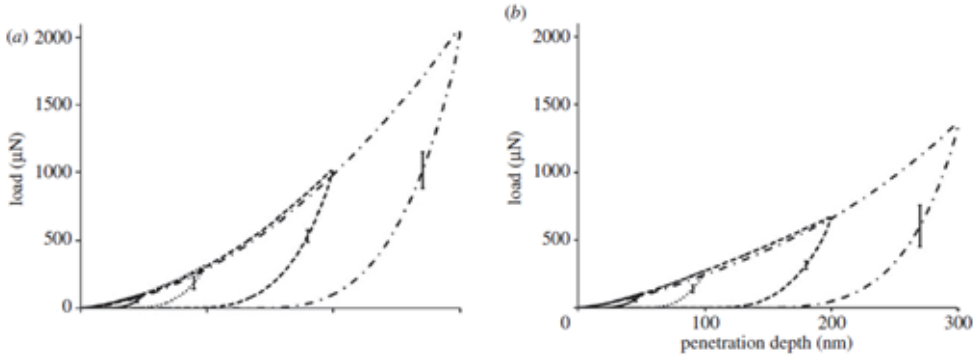

Figure 21: Averaged load versus penetration depth plots in the (a) axial and (b) transverse directions at the four tested maximum depths [44]

The tissue indentation modulus ranges from 26.24 ± 1.68 GPa to 19.73 ± 0.73 GPa along the axial direction and from 23.59 ± 3.55 GPa to 15.39 ± 1.04 GPa along the transverse direction. A decrease in the indentation moduli mean values is observed between 50 and 300 nm, this reduction being more pronounced along the transverse (approx. 35%) than along the axial (approx. 22%) direction [44].

An indentation study conducted to investigate the local anisotropic mechanical behaviour on bovine bone was made by Dall'Ara et al. (2015). The authors studied this anisotropic behaviour of plexiform bone at two dimensional levels with two indentation techniques: depth sensing micro-indentation (BSU level, penetration depth equal to 2.5 μm) and reference point indentation (RPI, at tissue level, penetration depth approximately 50 μm). They performed the nanoindentations on dehydrated tissue and they found that all microindentation parameters were dependent on direction. The local indentation modulus E_{ind} was found to be highest for the axial direction (24.37 ± 2.5 GPa) compared to the one from circumferential indentations (19% less stiff) and from the radial direction (30% less stiff) [45].

1.3.5 Nanoindentation to characterize tissue from Osteogenesis Imperfecta subjects

Aging produces a general decline in the mechanical integrity of bones, but diseases such as osteoporosis and OI accelerate bone deterioration thereby causing them to become more prone to fracture. In the study performed by Albert et al. (2013), bone material properties were compared between young individuals (11 paediatric patients between 5 and 18 years of age, male and female) with OI type I and OI type III. The indentations were made on the osteonal bone and on the interstitial lamellar bone of tibia or femur (on dehydrated tissue). Typical indent sites are shown in Fig.22.

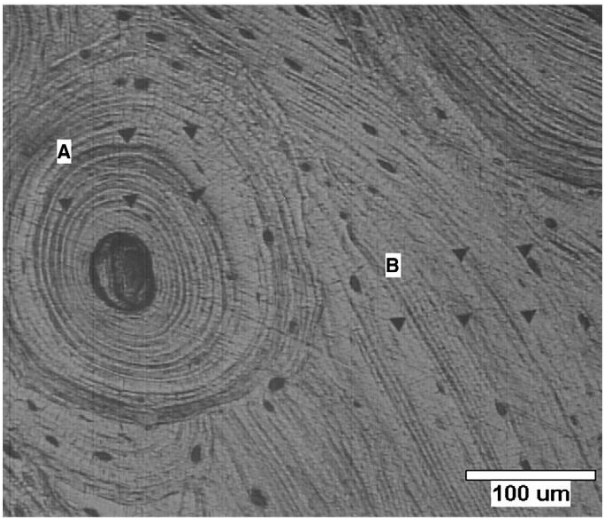

Figure 22: Location of typical indentation sites. (A) Osteonal bone region. (B) Interstitial lamellar bone region. The bone cross section shown was obtained from the femoral diaphysis of a 16-year-old male with OI type I [46]

They found that OI disease severity had a significant effect on elastic modulus and on hardness. The bone from individuals with OI type III had lower moduli (approximately 7% difference, 16.3GPa vs 17.5 GPa) and lower hardness (approximately 8% difference) than the tissue from individuals with OI type I. Bone microstructure also had a significant effect on modulus and hardness, with osteonal bone having lower modulus and hardness than interstitial lamellar bone (osteonal regions tend to be less mineralized than interstitial ones, and a relationship has been observed between local bone modulus and degree of mineralization). Finally, the effect of anatomic site was also significant with the modulus being higher in the tibia than the femur by approximately 8%. Therefore, the effect of OI severity on modulus and hardness may be related to factors other than mineralization density, such as: size, shape and composition of the mineral crystals, collagen structure, and/or mechanical interaction between the collagen fibrils and the mineral crystals [46].

Similar results were found in the study by Fan et al. (2006), in which they measured the intrinsic mechanical properties of OI type III bone tissue (8 OI type III bone specimens, aged 3.2–12.4 years) from low extremities. They performed the indentations both on the cortical and on the trabecular bone (on dehydrated tissue) and they found that there is no difference between them (E_b=13.9 vs E_b=13.6 GPa; H=0.42 vs H=0.42 GPa). The difference between cortical and trabecular bone might be due to the variations in canalicular porosity or mineralization of the extracellular matrix. Compared with adult healthy subject, OI type III has decreases in both modulus and hardness (around -32%) of both cortical and trabecular bone tissue and the decrease in cortical bone is larger than trabecular bone. This phenomenon might be due to the fact that collagens are more densely compacted in cortical bone than trabecular bone [40].

Then, in a subsequent study by Fan et al. (2007), similar tests were performed to compare the mechanical properties of OI type III and OI type IV patients (10 subjects, aged 1.9 to 13.2 years old). They performed their tests on dehydrated tissue. For both cortical and trabecular bone, modulus and hardness did not show any significant difference between these two patients. They reported also that OI bone tissue has a relative homogenous property compared with normal bone. These findings indicate that nanoindentation may offer a method to technically classify OI types in children [47].

1.4 Micro-Computed Tomography

The use of Micro–Computed tomography (μCT) imaging for the trabecular and cortical bone morphology in animal and human specimen has grown a lot in the last few years [48]. μCT has become also the ‘‘gold standard’’ for evaluation of bone morphology and microarchitecture in rodents *ex vivo*. μCT uses X-ray attenuation data acquired at multiple viewing angles to reconstruct a 3D representation of the specimen that characterizes the spatial distribution of material density (Fig.23). Currently available μCT scanners achieve an isotropic voxel size of as low as a few micrometres, which is enough for investigating structures such as mouse trabeculae that have widths of approximately 30 to 50 μm [49].

The μCT is based on the interaction of the X-rays with the specimen and the system is composed by three elements: the X-ray source, the specimen rotation system and the detector (a charge-coupled device, CCD). Usually, the specimen is placed between the source and the detector. The detector measures the intensity of the X-rays after they have passed through the specimen. At each rotation the detector acquires a two-dimensional image (projection) and the set of projections acquired at different angles is used to reconstruct a three-dimensional image of the scanned object [48].

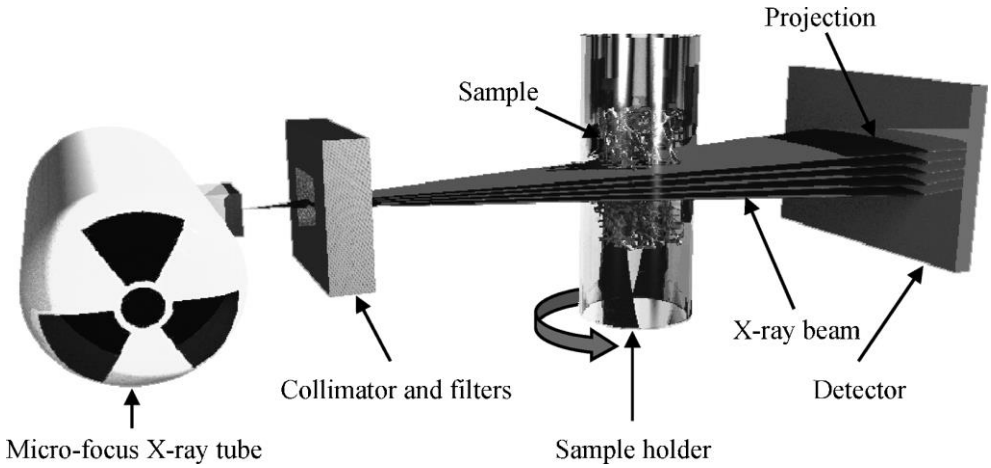

Figure 23: A microfocus X-ray tube emits X-rays that are collimated and filtered to narrow the energy spectrum. The X-rays pass through the object and are recorded by a 2D charge-coupled device (CCD) array [48]

The excellent reproducibility and accuracy of µCT measurements of bone morphology have been established in several studies. There are numerous advantages to using µCT for assessment of bone mass and morphology in excised specimens:

- It allows for direct 3D measurement of trabecular morphology, such as trabecular thickness and separation;
- Significantly large volume of interest is analysed;
- Measurements can be performed with a much faster using undecalcified bone specimens;
- Assessment of bone morphology by µCT scanning is non-destructive; thus, specimens can be used subsequently for other assays.

Finally, µCT scans may be used to provide an estimate of bone tissue mineralization by proper calibration of the images after comparison of the X-ray attenuation with the known density values of hydroxyapatite standards (phantoms).

1.4.1 Image acquisition, reconstruction and processing

The first step is the preparation and positioning of the specimen on the holder. the specimens must be oriented consistently within the holder and scanner. Commonly, specimens are aligned with the vertical axis of the scanner, although alignment with the horizontal axis is possible as well. It is possible to scan specimens in various media [48]. The sample should be well fixed to the rotation stage to avoid moving artifacts in the image.

A *voxel* is the discrete unit of the scan volume that is the result of the tomographic reconstruction. The information content of a voxel depends on the signal-to noise ratio (SNR), and this is governed by the number of incident photons and the sensitivity of the detector. The total number of photons for each projection during a tomographic scan depends on the tube current. Ideally, the smallest voxel size (i.e., highest scan resolution) available would be used for all scans; however, higher-resolution scans require longer acquisition times because they must collect more projections and generate large data sets.

The integration time (time during which the X-Rays source is shooting photons toward the specimen) and the number of frames per projection directly influence the duration of the scan and the SNR.

Another important issue pertains to the definition of the ROI when comparing bone specimens of varying size (i.e., bone length). The usual goal is to choose an ROI that is anatomically and biomechanically comparable among specimens. Thus, in situations where the bone length differs between groups, a uniformly sized ROI will relatively over specimen the shorter bones and under sample the longer bones.

Reconstructed µCT data inherently include signal noise that should be reduced by filtering while maintaining sharp contrast between bone and marrow. Removal of image noise is best accomplished by a low-pass filter, but this essentially blurs the image. Edge enhancement requires a high-pass filter, yet this may result in increased noise. Generally, a Gaussian filter does well at balancing these competing objectives, is easy to implement, and is fast, even for large data sets. It is perhaps the most commonly used filter, but other options such as median filtering also provide good results.

The segmentation process is a critical step and an important issue relates to the contouring method employed to define the area in each slice to be included for segmentation. The easiest approach is to create a constant circular or rectangular area that captures all the bone of interest. The simplest approach is to use a global threshold that extracts all voxels from the µCT data exceeding a given CT value (density). The advantage of using a global threshold is that it is efficient and requires setting only one parameter [48].

1.4.2 Image analysis

The standard method of quantitatively describing bone architecture is the calculation of morphometric indices. The cortical and the trabecular bone are characterised by different parameters. The most important outcomes for the trabecular bone microarchitecture are, for example, the measurement of bone volume (BV) and the total volume of interest (TV). The ratio of these two measures is termed bone volume fraction (BV/TV). Trabecular thickness (Tb.Th), trabecular separation (Tb.Sp.) and trabecular number (Tb.N) can be derived indirectly after assuming a fixed-structure model. The connectivity (Conn) characterize the redundancy of trabecular connections. Connectivity is derived from the Euler number, which is a fundamental topologic measure counting the number of objects, the number of marrow cavities fully surrounded by bone, and the number of connections that must be broken to split the structure in two parts. Since the connectivity depends on structure size, it is more

appropriate to present this index as a density (Conn.D, $1/mm^3$) by dividing it by the total volume.

For the cortical bone, the most common morphological parameters are total cross-sectional area inside the periosteal envelope (Tt.Ar, mm^2), cortical bone area (Ct.Ar, mm^2)=cortical volume (Ct.V)/(number of slices*slice thickness) and marrow area (Ma.Ar, mm^2) [48]. Another basic measure is the bone surface (BS); the bone surface density (BS/TV) and specific bone surface (BS/BV) then can be derived easily by dividing the total volume or bone volume, respectively [51]. Although µCT has been used primarily to generate information about bone structure, it also can be used to estimate tissue mineral density (TMD) [48].

1.4.3 Micro-Computed Tomography and Osteogenesis Imperfecta

Micro-computed tomography allows for the 3D analysis of BMD and bone microstructure. This modality is especially useful for OI research because patients routinely undergo corrective surgeries that involve removal of small bone fragments, which would normally be discarded post-operatively. The purpose of the study of Jameson et al. (2011) was to investigate µCT as a method to characterize properties of OI human bone. A total of 8 fragments were collected from lower extremity long bones (femur or tibia) in 5 patients (sex: 2M, 3F; age range: 1.5-11.5 years). Specimens were thawed and scanned in continuous mode (33 kVp, 231 µA, 360 views, 7-frame average) in saline solution at 35 µm isotropic voxel resolution. In each VOI the morphometric parameters were measured (BV/TV, BS/TV, Tb.Th, etc.). Examination of the reconstructed cubic VOIs showed a general plate-like structure, which is common for lower extremity long bones (Fig.24). Unlike healthy bone, the OI trabecular plates did not seem to follow any preferential orientation, suggesting a less organized architecture. Surprisingly, the specimens from one of the severe (type III) OI patients seemed to best follow the parallel plate bone model (Fig.24, G-H).

The results report that both Tb.N and Conn.D have an indirect relationship with severity of OI, where type III patients seemed to have less trabeculae and lower connectivity than those with either type IV or III/IV. The BMD tests did not reveal any clear relationships between OI severity and bone mineral metrics.

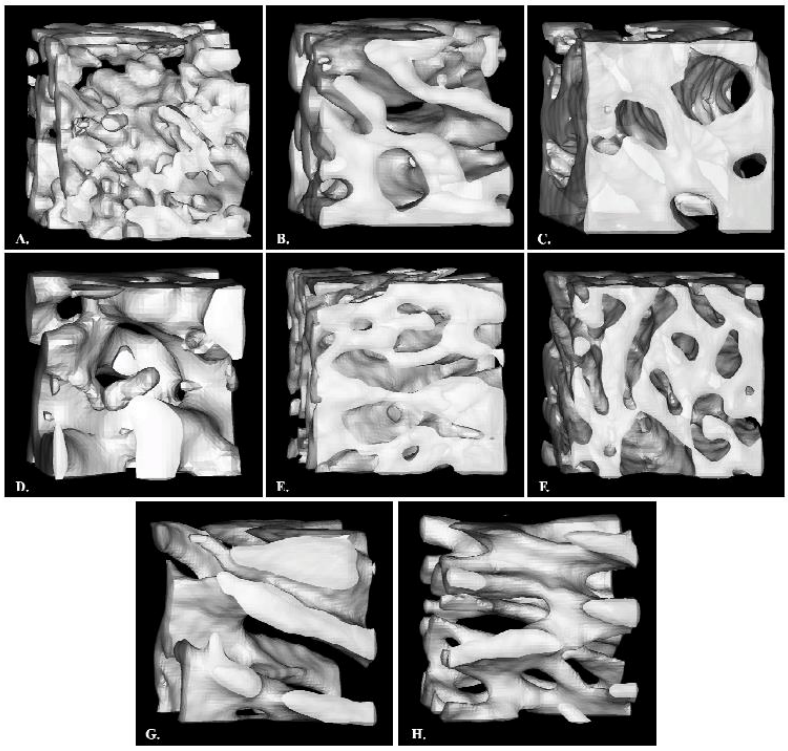

Figure 24: Surface-shaded renderings of trabecular VOIs. A-B: Patient 1; C: Patient 2; D: Patient 3; E-F: Patient 4; G-H: Patient 5 [50]

Minimal differences in trabecular parameters were reported between types III and IV OI. One interesting observation from this study was that connectivity density and Tb.N were highly correlated and seemed related to severity of OI. This could be an important diagnostic tool for distinguishing OI type in patients who present heterogeneous symptoms [50].

In another study, Ranzoni et al. (2018) described a dataset of µCT reconstructed scans of the proximal part of 21 tibiae from wild type mice, and *oim* mice. Their results reported that *oim* model exhibits characteristics of the severe human bone phenotype such as reduced size, skeletal fragility, frequent fractures, and abnormal bone microarchitecture, including reduced cortical and trabecular thickness, reduced trabecular number and increased porosity. In Fig.25 there is an example of reconstructed images obtained from the scans [51].

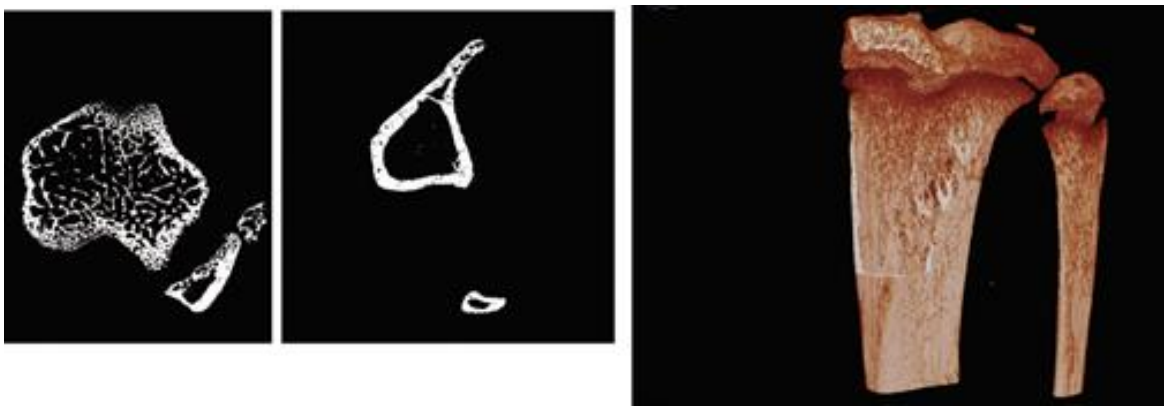

Figure 25: Example of reconstructed images: binarized cross-sectional images of trabecular and cortical bone of the tibia on the left and 3D rendering of the bone on the right [51]

1.5 Aims of the study

In recent years, nanoindentation has emerged as a powerful technique for investigating the micromechanical properties of bone.

The aim of this project was to develop a procedure to perform nanoindentation tests on bone tissue in order to study the elastic and inelastic properties of different bone structures. The main goal was to characterize the local reduced modulus, hardness, indentation modulus and elastic modulus of the bone. The nanoindentation on mouse bone tissue had as aims:

- Fine-tune method;
- Test repeatability on tightly repeatable bone samples (same bone from same mouse strain);
- Investigation of the potential differences between strains, spatial location or spatial orientation.

The nanoindentation on an OI specimen had as goal the characterization of the heterogeneous material properties across the specimen. The mechanical properties were investigated in order to compare them with the properties of the healthy bone and the OI bone reported in literature. The microCT scans were used in order to have scans of the sections on which the nanoindentations were performed and a scan of the whole specimen.

CHAPTER 2

MATERIALS AND METHODS

2.1 Specimens Collection

In this project it was decided to use first specimens of mouse tibio-fibular complex and then one specimen from OI human bone. We indented first the mouse bone to fine-tune the method and to avoid wasting extremely rare OI specimens.

All procedures performed in this study were approved by the local ethic committee (the NHS by the Yorkshire and Humber Research Ethics Committee). It has also been approved by the Research Department Sheffield Children's Hospital. Researchers at Sheffield Children's NHS Foundation Trust are organising this study.

2.1.1 Murine bones dissection

Four tibiae were prepared, two from C57B1/6 mice (wild type, 16 weeks old, female) and two from Balb/C mice (wild type, 16 weeks old, female) used in previous studies [52] and kept fresh frozen until sample preparation. Two left legs (per strain) were thawed at room temperature, and the tibiae were dissected from them (Fig.26).

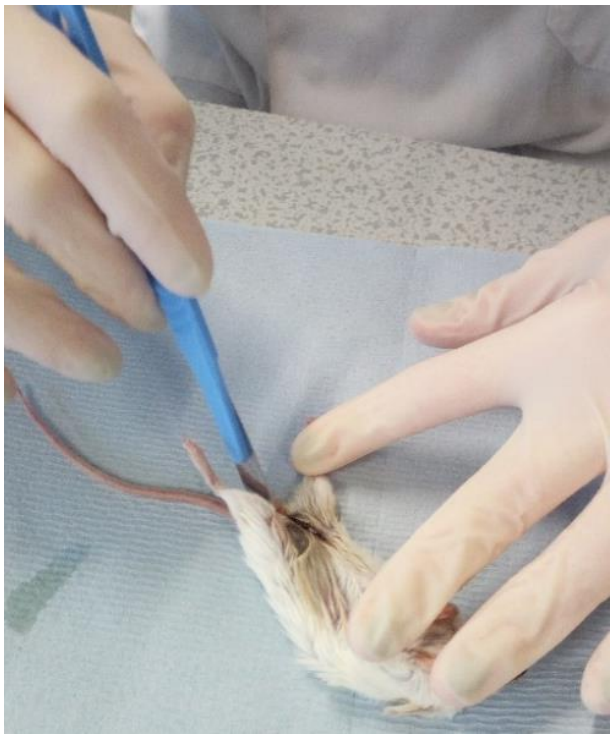

Figure 26: Dissection of a Balb/C mouse's leg

The skin and muscles around the tibia were removed using a scalpel. Then tendons around the ankle were cut and muscles were pulled using tweezers. The ligaments of the knee were cut to separate the femur from the tibia. Then the foot was cut as close as possible to the ankle joint. After removing all muscles and soft tissues, tibiae were stored in the freezer at approximately -20° C.

2.1.2 Human bone specimen

The human bone specimen used in this project was extracted during a surgical procedure (GC 25926 – 11/01/2018) performed on 9-year old boy with osteogenesis imperfecta (C-propeptide cleavage variant in COL1A1). The specimen, mainly of cortical bone, was obtained from the upper limb.

2.2 Specimens Preparation

A similar procedure was used for both mouse tibiae and human specimen, which consisted of several steps, as described in the following paragraphs.

2.2.1 Dehydration

Specimens were defrosted in saline solution at room temperature. Afterwards, specimens were placed in a fume cupboard for at least 2 hours for dehydration (Fig.27).

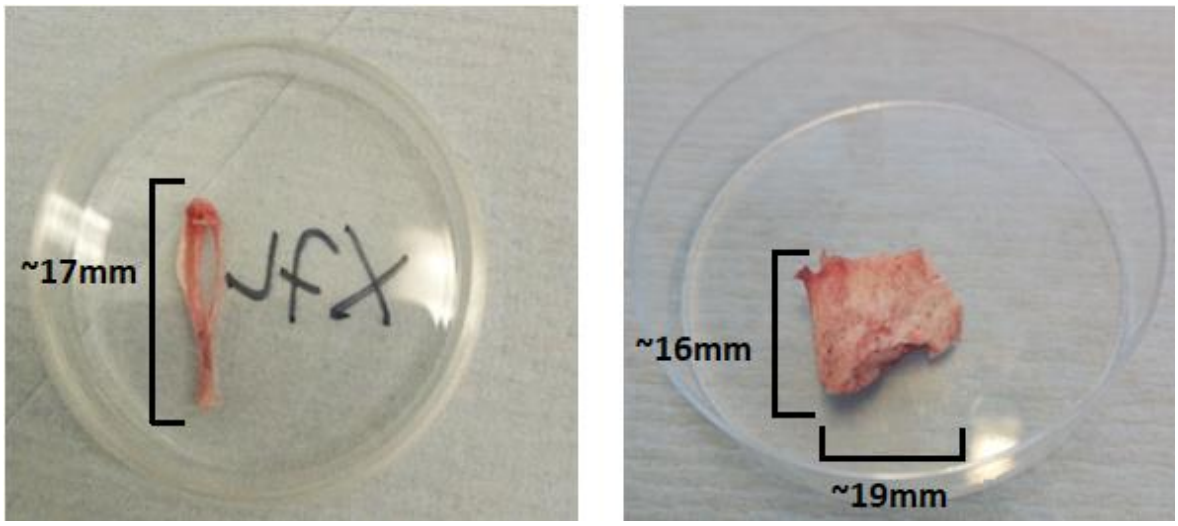

Figure 27: Dehydration procedure under the fume cupboard. Mouse tibia (C57B1/6) on the left and human bone on the right

2.2.2 Embedding

The embedding procedure consists in including the specimen with acrylic resin to support the bone tissue during the nanoindentation tests. The procedure for the mouse and the human bone was similar, but with a small difference in size of the embedded portion (the human specimen is largest and requires a larger amount of resin).

2.2.2.1 Mouse tibiae embedding

Mouse tibiae were placed in 2 ml Cryovials (Simport, Montreal, Quebec, Canada) using a small amount of plasticine at the bottom.

The EpoFix Resin (Struers, Catcliffe, UK) was prepared using the procedure suggested by the manufacturer: 10 ml (± 0.1) of resin were mixed with 1.(3) ml of hardener for one minute. After resting for a few minutes, the epoxy mixture was carefully placed in a syringe, in order

to reduce the formation of air bubbles. Each cryovial was filled with epoxy mixture and the tibia was re-aligned with the tweezers if necessary.

The specimens in the open containers were placed in a vacuum chamber and kept for five minutes to remove the bubbles from the internal portion of the specimen. The specimens were left overnight under the fume hood for the resin to dry (Fig.28).

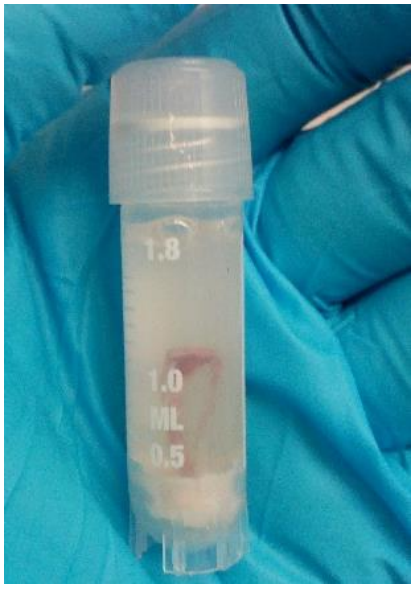

Figure 28: Tibia embedded in the resin

The tibiae were four; the specimens name and the number of slices obtained from each tibia are shown in Table 2.

Mouse tibiae		
Strain	**Specimens name**	**Slices**
C57B1/6	X7L	5
C57B1/6	X9L	4
Balb/C	L1	5
Balb/C	L3	5

Table 2: Specimens name and slices obtained from each tibia (two per strain) are reported

2.2.2.2 Human bone embedding

For the human specimen, a similar procedure was used, but with some minor changes. A Petri dish was used because of the larger dimension of the specimen. To make sure that the specimen was completely included in the resin three little portions of plasticine were placed on the three corners of the specimen before pouring the resin, as shown in Fig.29.

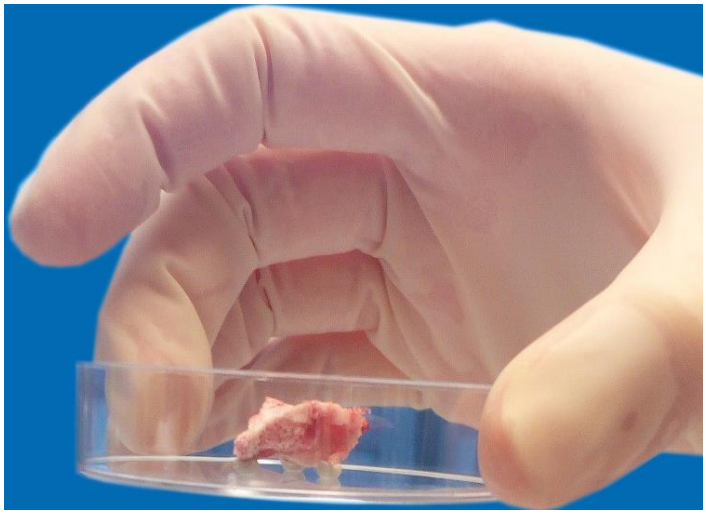

Figure 29: Human specimen with plasticine on three corners

The same epoxy resin was used but the amount has been tripled (30 ml of resin with 3.9 ml of hardener). Then the specimen was placed in the vacuum chamber following the same procedure used for the mouse tibia (Fig. 30).

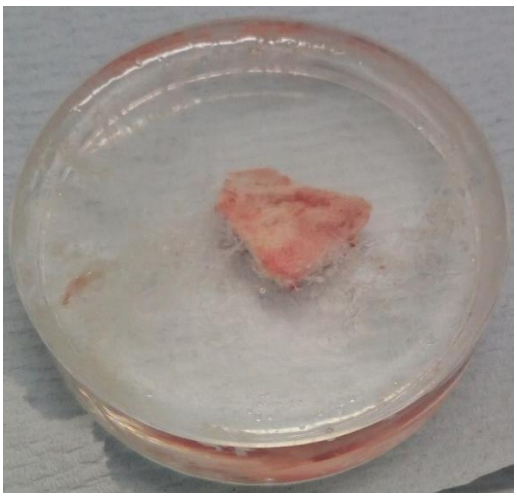

Figure 30: Human bone embedded in the resin

It was decided to scan the human specimen in order to have scans of the whole specimen and of the four sections on which the nanoindentations were performed. The first thing to do before the scanning was cutting the specimen in order to fit the microCT scanner. Using a hand saw, the disk has been cut to obtain a rectangle (Fig.31). The final dimensions were 20.38x19.65x10.88 mm.

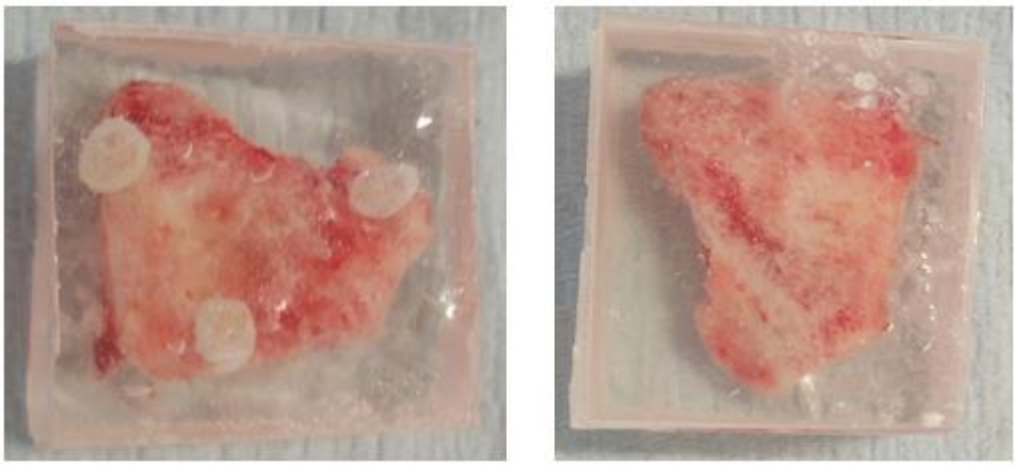

Figure 31: OI bone specimen before scanning

2.2.2.3 Human bone scans

Before cutting, the human specimen was scanned with a micro-CT system (Skyscan 1172, Fig.32).

Figure 32: Specimen mounted securely inside the Micro-CT machine

The following scanning parameters were used: voltage 100 kV, current 90 μA, voxel size 8.88 μm, exposure time 885 ms, rotation step 0.700 deg, medium camera binning (2000x1048), frame averaging ON (2), 1.0 mm Al beam hardening-filter. Then, the scans were reconstructed using a ring artifact correction equal to 10. The total reconstruction time (2394 slices) was 899 s.

The reconstructed image was post-processed in MATLAB for segmentation. A gaussian filter (kernel 3x3x3, standard deviation=0.65) was applied in order to remove the high frequency noise [53]. A global threshold was used for segmentation, which was calculated as the average of the grey levels corresponding to the bone and background peaks in the image histogram. The segmented images were visualised in Amira v6.01 (Thermo Fisher Scientific, Fig.33).

Figure 33: 3D image of the human specimen in a xy view

2.2.3 Cutting

Specimens were cut using a Low Speed Saw (IsoMet, Manassas, Virginia, USA), equipped with a diamond coated blade, under constant distilled water irrigation (Fig.34).

Figure 34: Low Speed Saw (IsoMet)

For the mouse bone, 3 mm thick sections were cut. The human specimen embedded in the resin was cut in four slices with a thickness of 4 mm (Fig.35).

Figure 35: Cutting of the specimens by the blade. Mouse tibia on the left and human bone on the right

After each cut, the thickness was measured with a digital calliper (Fig.36).

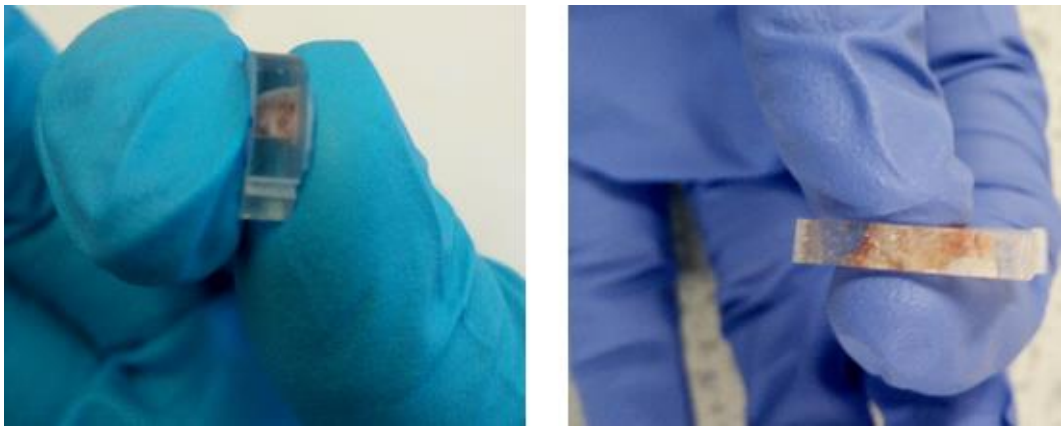

Figure 36: Slices after cutting. Mouse tibia on the left and human bone on the right

For the mouse tibiae, the most proximal cut contained trabecular bone. The X7L, L1 and L3 specimens were cut into five slices while the X9L specimen in four, according to the available tibia length. The slices were assigned to different groups (proximal, central and distal; one-third for each section) according to their spatial location in the tibia.

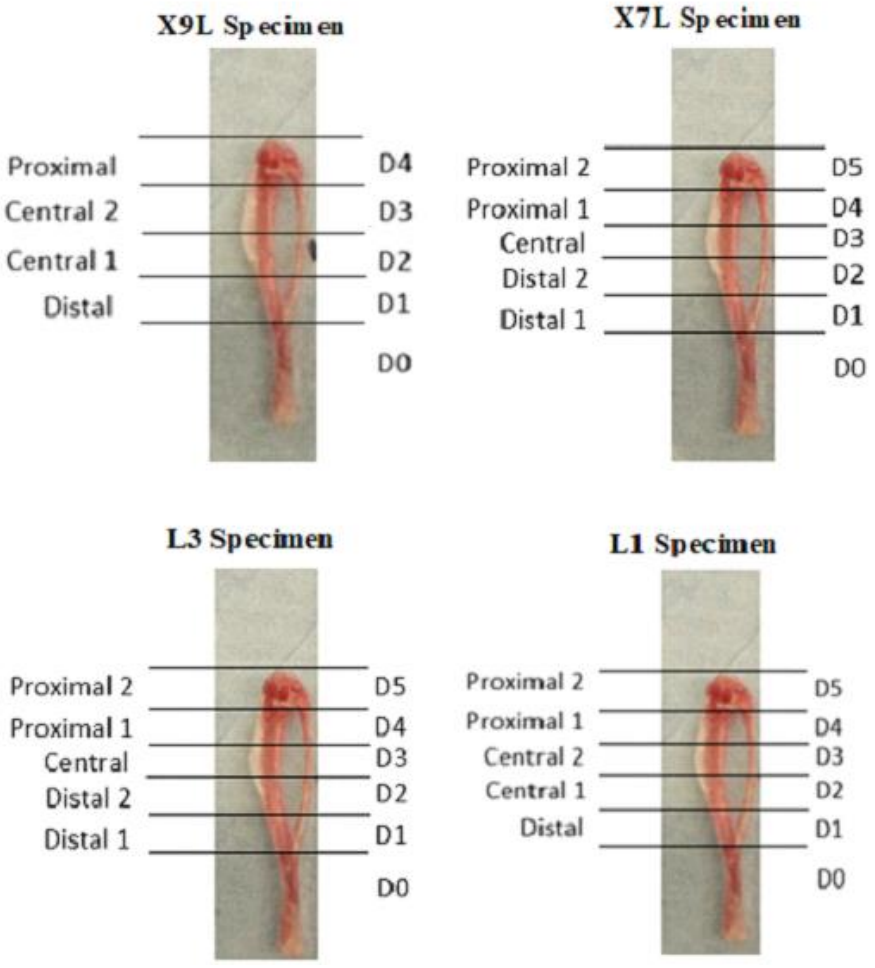

Figure 37: Cutting scheme of the four tibiae

Dimensions of the four tibiae (mm)				
Slices	**X9L**	**X7L**	**L3**	**L1**
D1	2.7	2.59	2.61	2.53
D2	2.65	2.52	2.60	2.61
D3	2.66	2.56	2.59	2.57
D4	2.63	2.35	2.58	2.61
D5	/	2.82	2.52	2.56

Table 3: Thickness of each slice (mm)

According to the length of the tibia (and therefore according to the part of tibia that was in the plasticine), the different slices were attributed to a section (for this it is possible that there are corresponding slices belonging to different sections in the four tibiae).

Since we did not know the anatomical orientation of the human specimen, it was decided to carry out the polishing and therefore the nanoindentations on the inner face with respect to the cut.

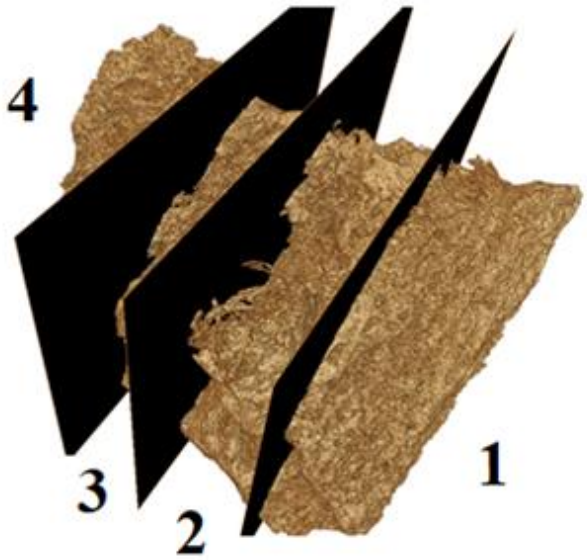

Slice	DIMENSION (mm)
1	3.84
2	3.61
3	3.59
4	8.36

Figure 38: Cutting scheme and dimensions of the human bone specimen

2.2.4 Polishing

The specimens were glued to the metallic holders before polishing. The polishing procedure aims at reducing the surface roughness before nanoindentation. Three types of silicon carbide papers have been used for the polishing (P400, P800 and P1200, Struers, Willich, Germany) followed by a step with alumina 0.05 µm size particles (MasterPrep polishing reagent).

The polishing was made on the proximal surface for the mouse bone for each slice (except for the most proximal slice where the polishing was made on the distal surface) and on the "internal" surface for the human bone. The 400 grade paper was used to grind the back and the front of each specimen to eliminate surface imperfections. 8-like movement was made while pushing the specimen by hand against the polishing paper in the same way throughout the process to ensure the surface was planar. Then the specimen was observed under a reflection microscope (10x objective), (Olympus, Shinjuku, Tokyo, Japan).

The polishing was performed with some distilled water as lubricant. The specimens were polished with P400 paper for approximately 30 s until approximately 20-30 µm were removed. The specimen was observed again under the microscope (Fig.38a and 40a). The same steps have been made on the P800 paper (this operation removed about 20 µm; make 8-like motions for one minute, (Fig.38b and 40b)). The same steps have been made also on the P1200 paper (this operation removed around 20 µm; make 8-like motions for two minutes (Fig.38c and 40c). The MasterPrep (Buehler, Lake Bluff, Illinois, USA) polishing reagent was placed on the micro cloth and the same polishing procedure (make 8-like motions for seven minutes) was used. The MasterPrep reagent contains microgranules of 0.05 µm size which improve final polishing. After this last step, the lamellae and the osteons in the specimens were visible (Fig.38d and 40d). These operations were made for each specimen.

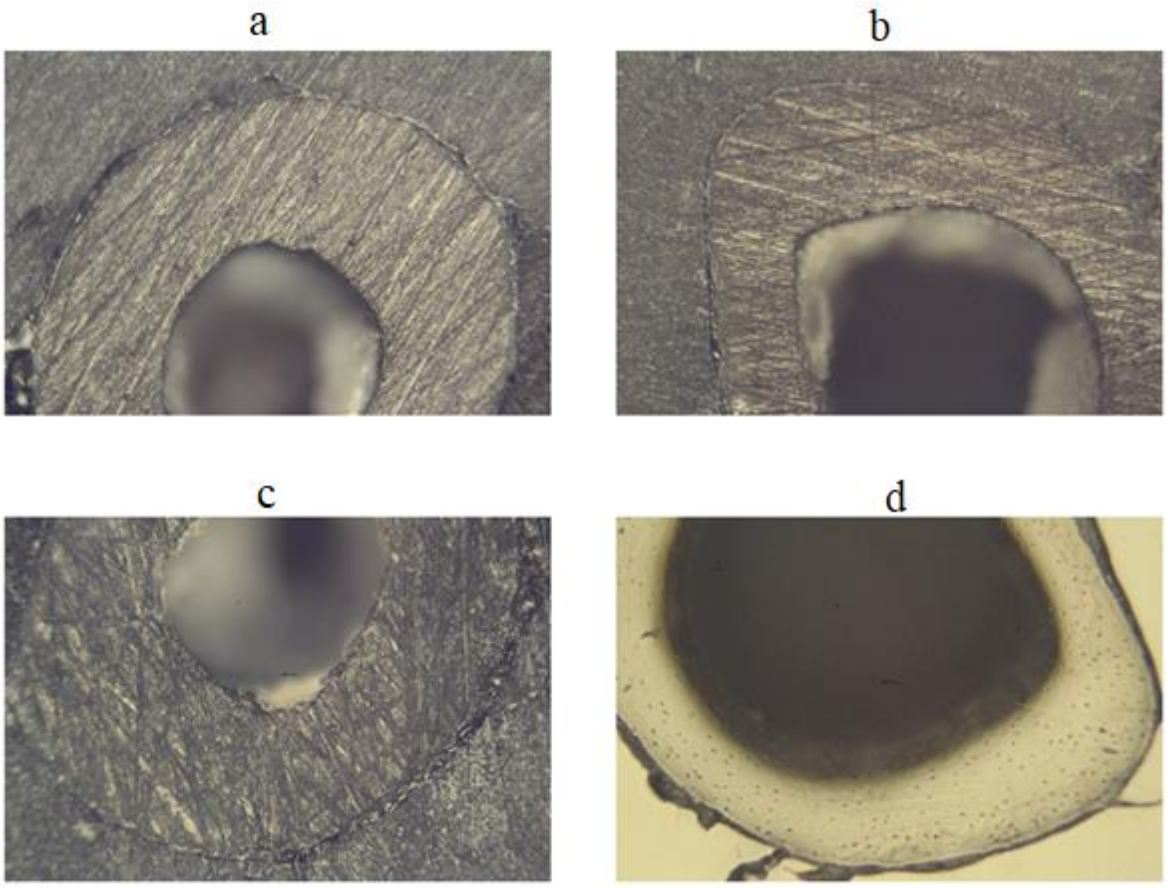

Figure 39: Mouse cortical bone under the microscope after polishing by P400 (a), P800 (b), P1200 (c) papers and Alumina paste solution (d)

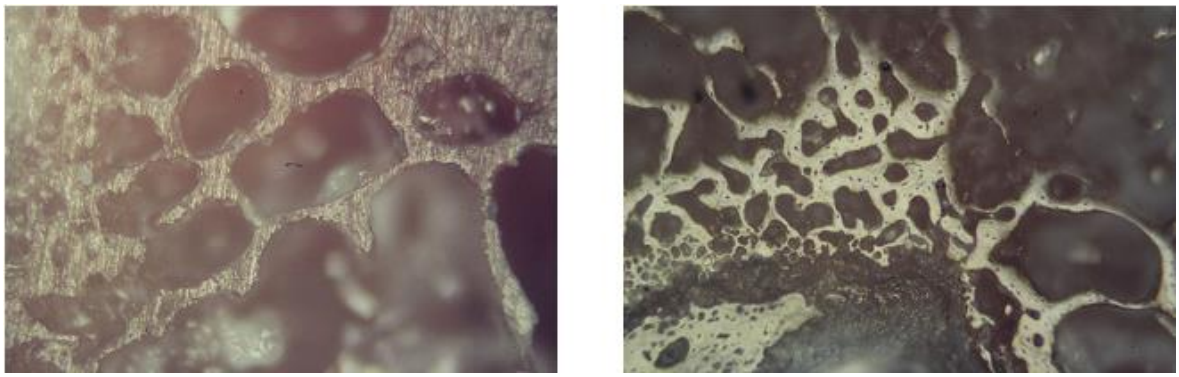

Figure 40: Mouse trabecular bone under the microscope after polishing by P1200 (left) and Alumina paste solution (right)

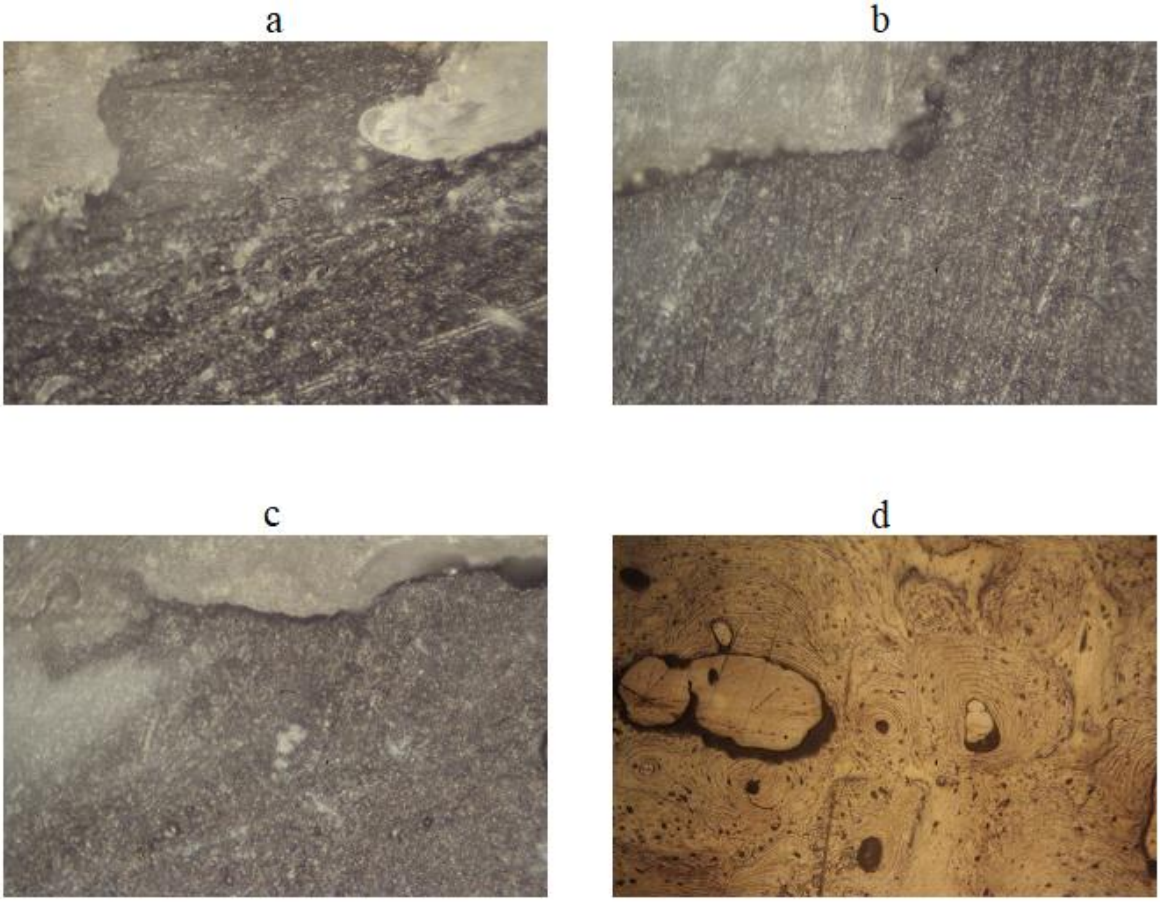

Figure 41: Human cortical bone under the microscope after polishing by P400 (a), P800 (b), P1200 (c) papers and Alumina paste solution (d)

2.3 Nanoindentation tests

2.3.1 Location of the nanoindentation on murine bone

In total, nineteen specimens (slices) were prepared for nanoindentation from the four tibiae. On the cortical bone, twenty-four indentations were performed, divided in four groups in the medial, lateral, anterior and posterior regions of the tibia.

Six indentations per region were performed. On the most proximal slices 5 trabeculae were chosen and 3 to 5 indentations per trabecula were performed according to its length.

The indentation procedure was adapted from Casanova et al. (2017). In particular, indentations were performed up to a maximum load of 6000 μN that leads to a penetration depth of approximately 500 nm and radius of approximately 3500 nm (indentations within a lamella). The distance between the indentations within the same pattern was set equal to

15 µm and the distance from the edge was approximately 30 µm in order to leave enough space between indentations and from the border. More detail about the indentation procedure is reported in section 2.3.4.

During the positioning of the indentation chosen under the indenter microscope, macro-porosity (e.g. Haversian or Volksman chanals), micro-porosity (e.g. osteocyte lacunae) or bone defects were avoided.

In total, 542 nanoindentations were performed on the mouse tibiae (442 on the cortical and 100 on the trabecular bone, Fig.42).

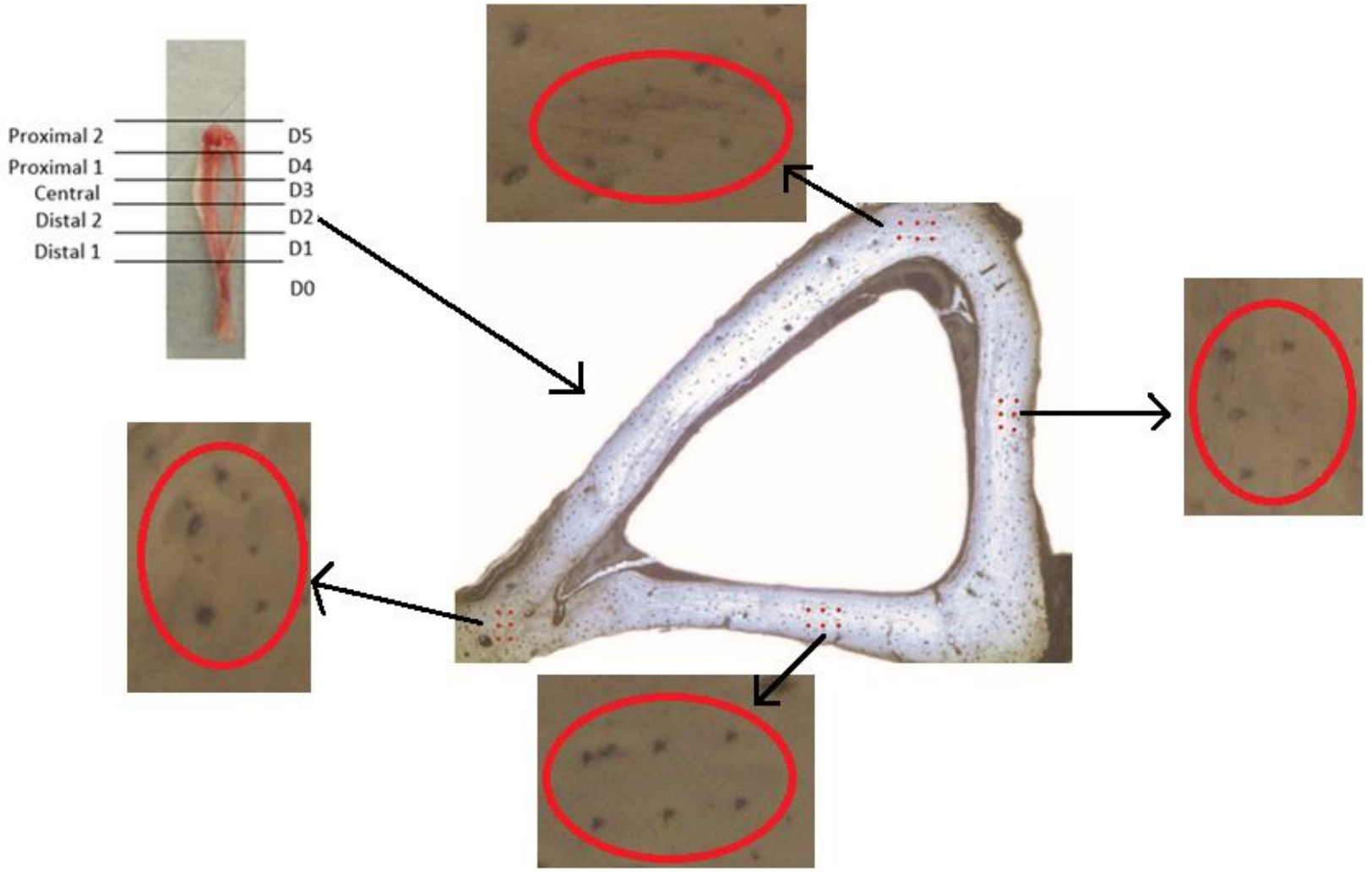

Figure 42: Scheme of the four indentation groups on the mouse cortical bone

2.3.2 Location of the nanoindentation on human bone

In the human specimen forty-eight indentations were performed on the cortical bone in each slice with the same indentation procedure presented for the mouse bone.

Nanoindentations were performed in two different spatial locations opposite to each other with two 12x2 grids. The distance between the indentations within the same pattern was set equal to 15 μm and the distance from the edge was approximately 30 μm. In total 192 nanoindentations were performed on the human specimen. The indentation groups are shown in Fig.43.

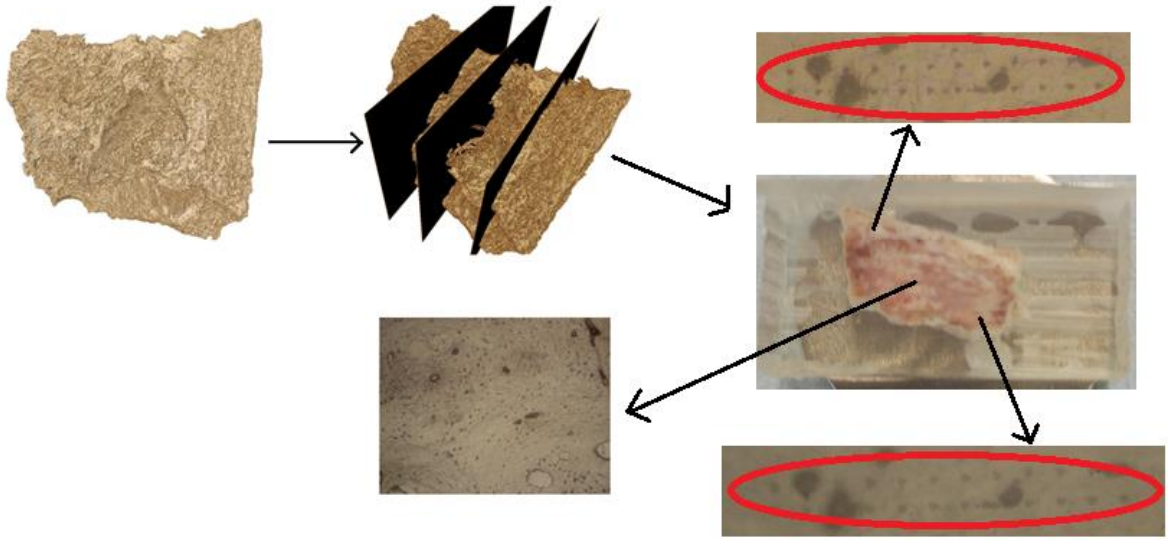

Figure 43: Scheme of the two indentation groups on the human cortical bone. The human bone was cut in four slices and then on each slice two groups of indentations were performed (in two different spatial locations). In the middle, the nanoindentations on the two spatial locations are shown and there is also a picture of the intact human bone under the microscope (on the left)

2.3.3 Nanoindentation procedure

The Hysitron TI Primer nanoindenter (Bruker, Billerica, Massachussetts, USA, Fig.43) has been used for the nanoindentation tests. This nanoindenter is ideal for the characterization of the heterogeneity of the local mechanical properties of the bone.

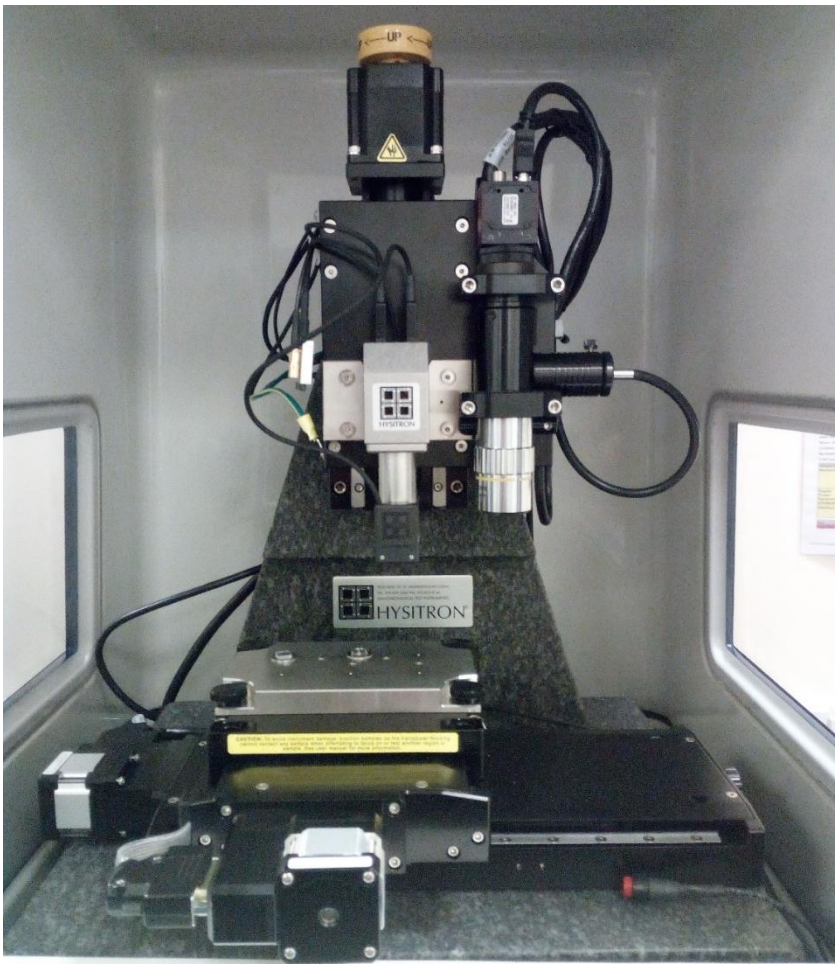

Figure 44: TI Premier Nanoindenter

The stage of the Hysitron TI Premier system uses magnetic forces for securing the specimens, which are glued to metallic discs.

The bone specimens, the polycarbonate sample (used for the calibration) and the fused quartz sample (used for calibrating the area function) were placed on the magnetic stage. During the positioning, care was taken in order to avoid contact between the tip and specimens. A Berkovich diamond indenter was used for all tests.

For these tests, (quasi-static) Trapezoid Load Functions were used (Fig.45). We replicated the testing procedure reported in Casanova et al. (2017) for the mouse femur. The following parameters were set:

- Maximal load: 6000 µN
- Loading time: 20 s (corresponding to a speed of 300 µN/s)
- Unloading time: 6.65 s (900 µN/s)

- Holding time: 30 s (in order to standardize timing to reduce the consequences and the variability due to the creep)

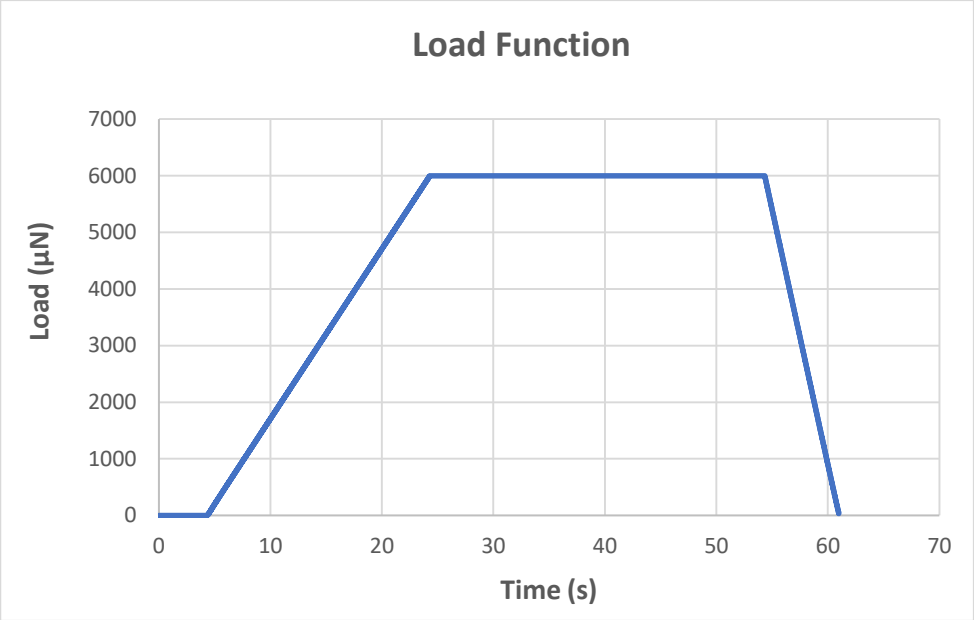

Figure 45: Trapezoidal Load Function

Usually, each indentation required about 4 minutes (around 3 minutes for the positioning and little more than one minute for the indentation). All indentations to be performed on a group of specimens (i.e. a mouse tibia or the human specimen) were first programmed in the nanoindenter and all indentations were performed after each other (typical total time for the indentations for one mouse tibia was between 8 and 12 hours).

2.3.4 Calibration procedure

The polycarbonate was used for the calibration and it was placed on the magnetic stage into the TI Premier. The first indentation was in the air; the second one was on the polycarbonate. During this phase seven indents in the shape of an H (three on each side for the legs and one in the middle) on the polycarbonate were performed. Then another indentation in the middle of the H (between the two points at the top) was performed. If this last indentation is in the right location it means that the calibration went well, and the tip can move to the bone specimens.

2.4 Data analysis

2.4.1 Analysis on the mouse tibia

A typical Load-Displacement curve for a successful indentation is shown in Fig.46:

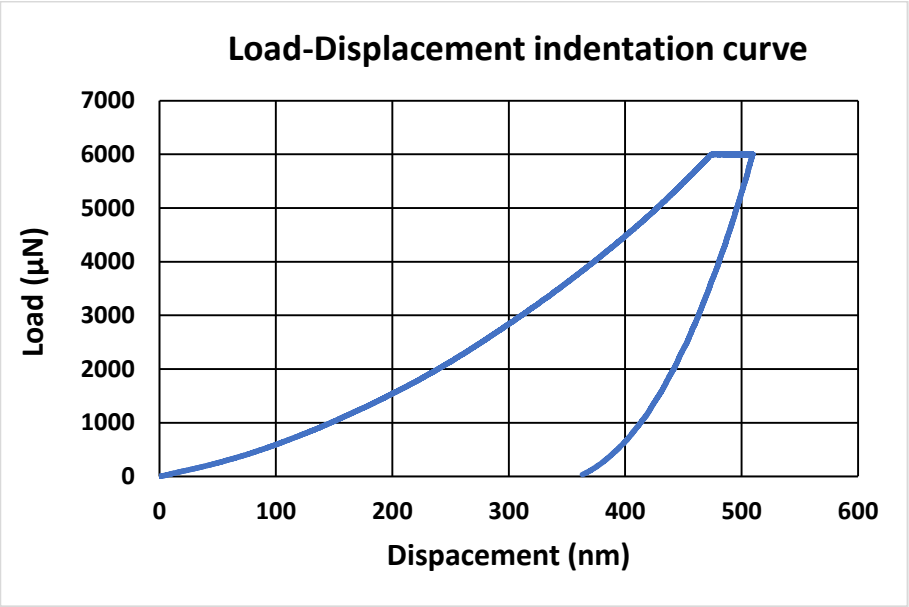

Figure 46: Load-Displacement curve obtained from one indentation

A typical curve has an initial concave curvature, an almost parallel return and it reached a penetration depth of approximately 500-600 nm. An example of a group of the six curves performed in one region of the cortical bone of one slice of one tibia is reported in Fig.47.

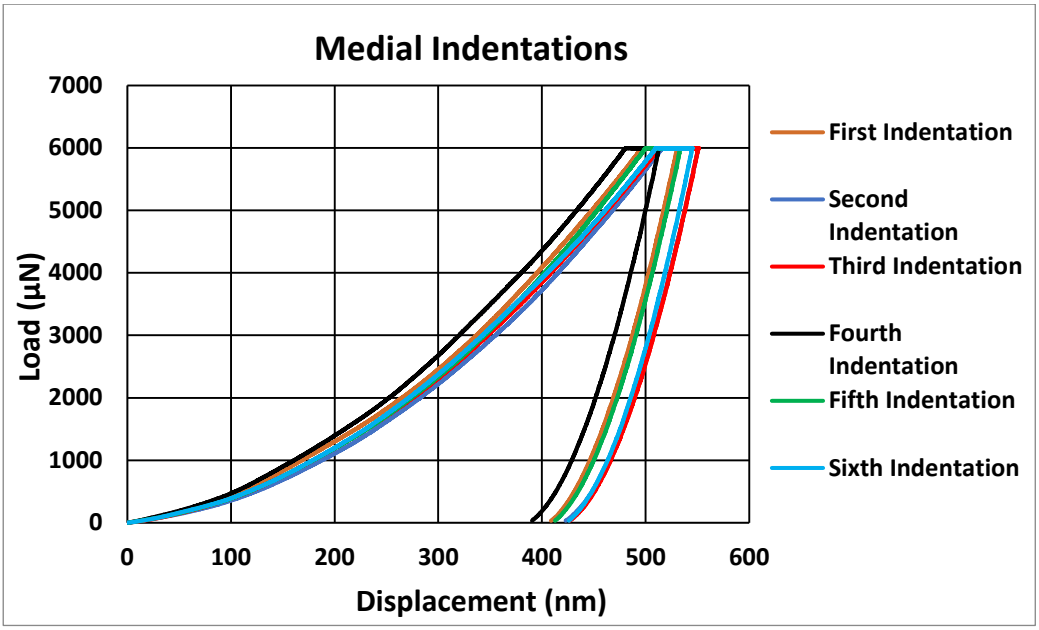

Figure 47: Load-Displacement curves obtained from six medial horizontal indentations (Balb/C L1 specimen-first slice)

Fig.48 shows a typical pattern 3x2 indentations in one region of the cortical bone of a mouse tibia (indentations are referring to the curves reported in Fig.47).

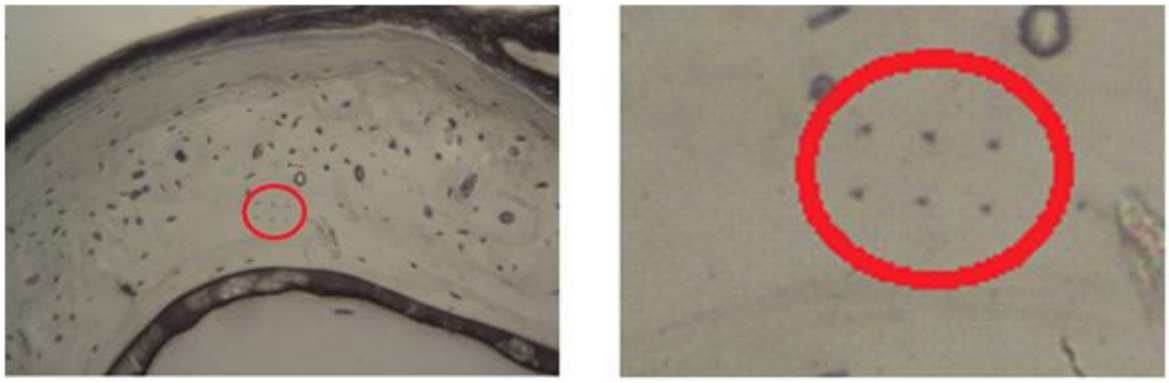

Figure 48: Balb/C (L1), first slice (the distal one). The indentations have been made on the top of the bone in the medial part of the tibia. Example of six horizontal indentations

Some curves showed a different shape, due to contact problems and were excluded from the data analysis. Typical shapes of excluded curves are reported in Fig.49 and in the appendix (Figs.1A to 14A). Possible causes include:

- A hyper mineralized zone, if the penetration is small;
- Contact problems;

- Presence of a dirty layer with a much lower density, the tip goes down and when it passes from the air to this thin and soft layer, it sees a change of inclination and considers that as contact. For example, the last curve in Fig.49 does not have the initial concave part and the parallel return, and the penetration stopped at almost 200 nm.

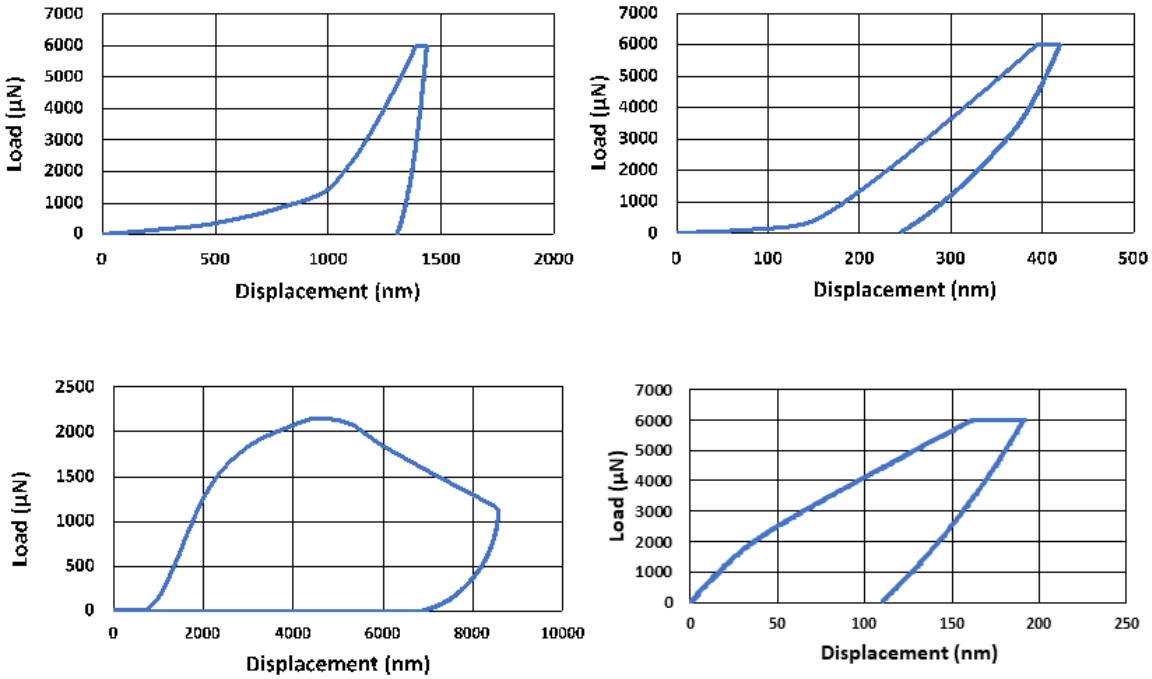

Figure 49: Example of Load-Displacement curves of wrong indentations

The data from the wrong curves reported in Table 4 were removed from the data analysis.

ID	File name	Strain	Bone type	Sec	Region	Sector	E_r (GPa)	H (GPa)	E_{ind} (GPa)	E_b (GPa)
386	L1-1-horiz_00000	Balb/C-2	Cortical	1	Distal	M	29.23	1.05	30.00	27.30
428	L1-2-vert_00006	Balb/C-2	Cortical	2	Distal	P	103.92	9.00	114.28	104.00
440	L1-3-horiz_00006	Balb/C-2	Cortical	3	Central	L	35.32	2.42	36.45	33.17
282	L3-2-vert_00006	Balb/C-1	Cortical	2	Distal	P	26.06	0.84	26.67	24.27
369	L3-5-trab_00009	Balb/C-1	Trabecular	5	Proximal	trab	2.83	0.04	2.83	2.58
370	L3-5-trab_00011	Balb/C-1	Trabecular	5	Proximal	trab	7.03	0.11	7.07	6.44
383	L3-5-trab_00024	Balb/C-1	Trabecular	5	Proximal	trab	32.29	1.80	33.22	30.23
174	X9L-3-horiz_00006	C57B1/6-2	Cortical	3	Central	L	66.16	6.25	70.21	63.89
213	X9L-4-vert_00009	C57B1/6-2	Cortical	4	Proximal	P	10.59	0.29	10.69	9.73
185	X9L-3-vert_00005	C57B1/6-2	Cortical	3	Central	A	10.28	0.14	10.37	9.44
130	X9L-1-horiz_00010	C57B1/6-2	Cortical	1	Distal	L	42.64	1.55	44.29	40.31
516	L1-5-trab_00010	Balb/C-2	Trabecular	5	Proximal	trab	7.21	0.64	7.25	6.60

Table 4: Data from the excluded indentations

The load-displacement data have been used to determine mechanical properties according to the theory reported in sections 1.3.1. The following parameters were calculated for each indentation:

- Reduced modulus E_r
- Hardness H
- Indentation modulus E_{ind}
- Bone elastic modulus E_b

2.4.2 Analysis on the human bone

A typical Load-Displacement curve for indentation on the human bone is shown Fig.50.

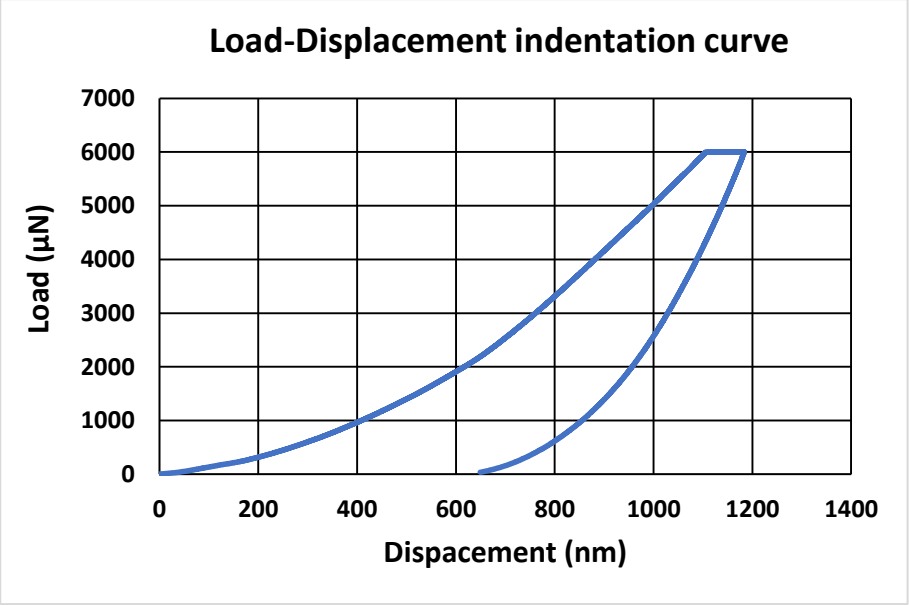

Figure 50: Load-Displacement curve obtained from one indentation

Typically, indentations achieved greater penetration depth compared to those obtained for the mouse bone. An example of a group of twenty-four curves is reported in Fig.51.

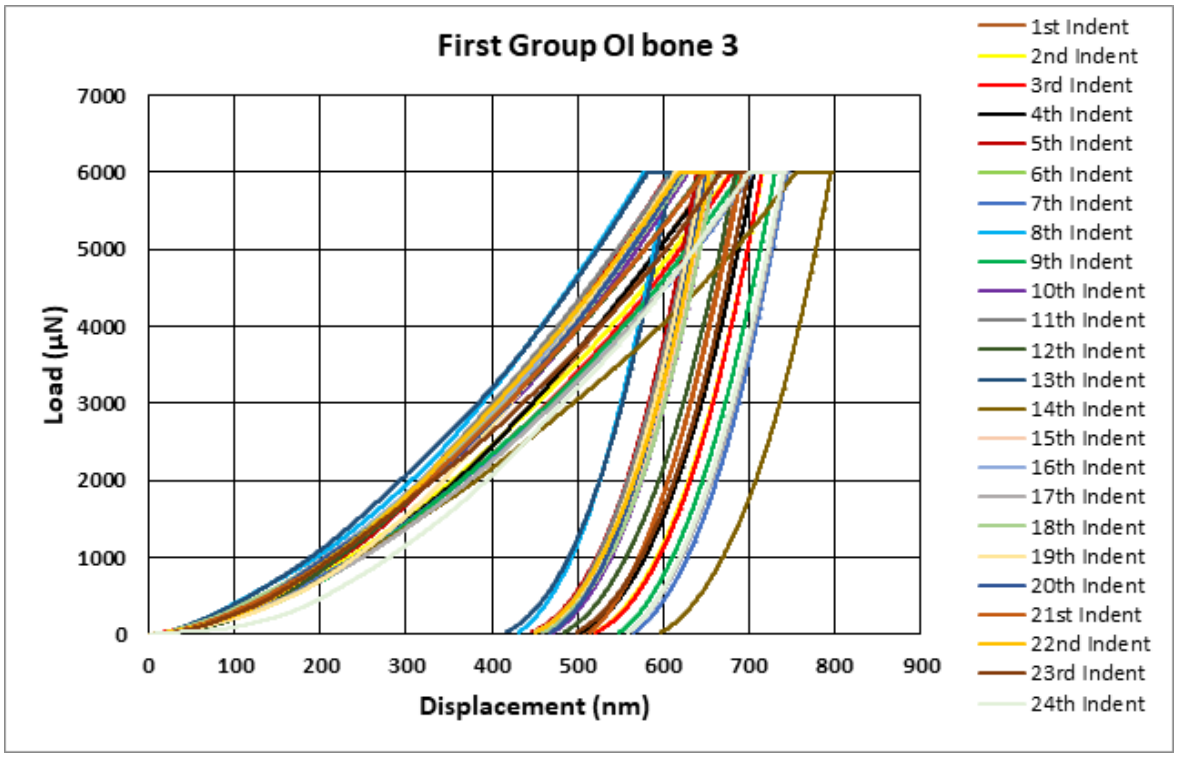

Figure 51: Load-Displacement curves obtained from twenty-four indentations

Just one curve among the 192 indentations performed on the human bone specimen showed an unsuitable shape and was therefore excluded from the data analysis (Fig.52).

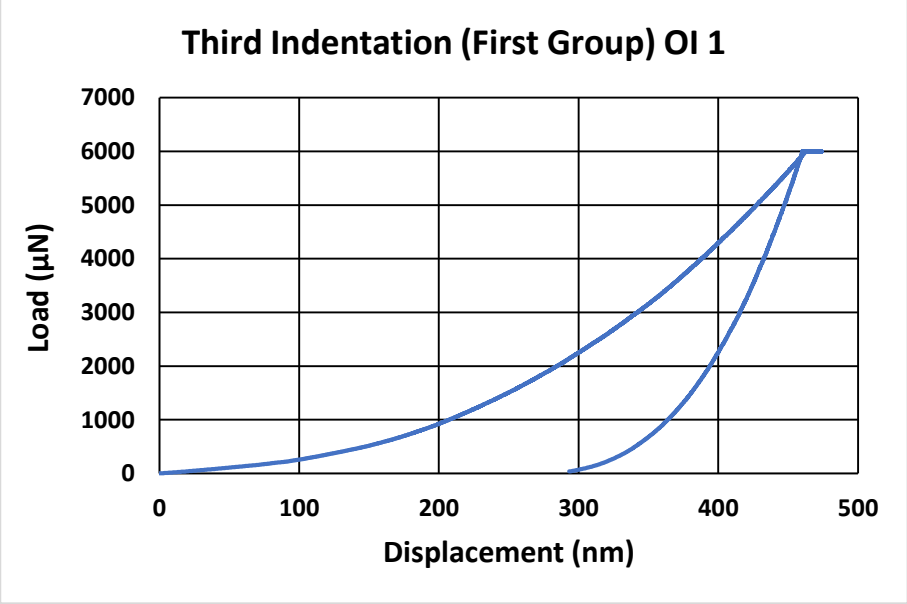

Figure 52: Load-Displacement curve of an excluded indentation. First slice. The indentations have been made on the top left corner of the bone. The wrong curve concerns the third indentation

2.5 Statistical analysis

2.5.1 Statistical analysis on the mouse tibia

The statistical analysis was performed in order to investigate potential differences in reduced modulus (E_r) and hardness (H) due to different factor (using IBM SPSS software, SPSS Statics Version 25).

The reduced modulus (E_r) and hardness (H) values were not normally distributed (Kolmogorov-Smirnov, $p<0.05$, Fig.53). Therefore, the non-parametric Kruskal-Wallis tests (significance threshold=0.05) were used to investigate potential statistically differences.

If a factor was significant, a Bonferroni Post Hoc analysis was done.

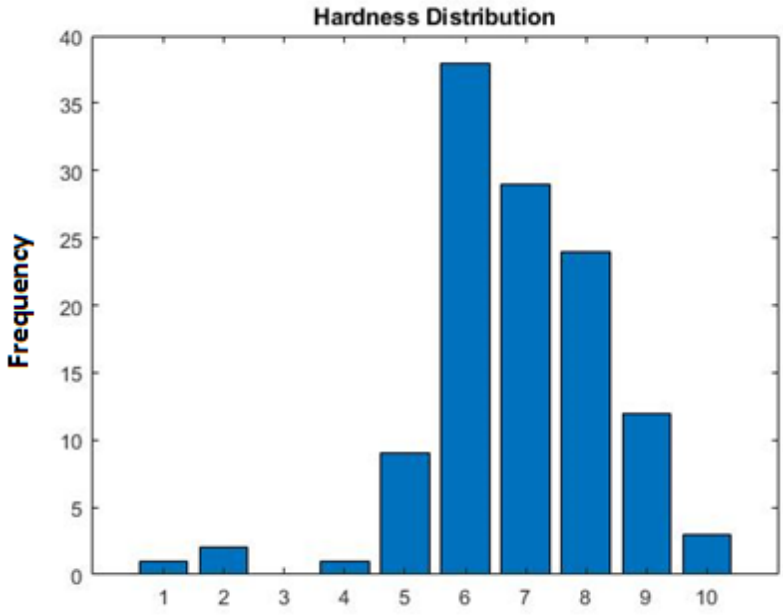

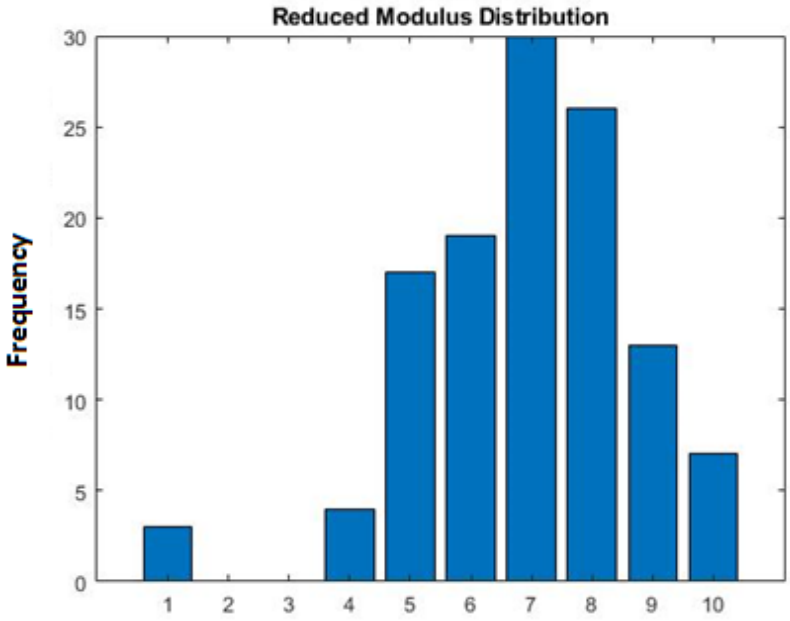

Figure 53: Example of not normally distributed data (the specimen is Balb/C L3)

Potential significant differences were investigated between mouse Strains (Balb/C vs C57B1/6), individual mice (two mice per strain), Sectors (Anterior, Posterior, Medial and Lateral) and Sections (Distal, Central and Proximal) for cortical bone measurements.

For the trabecular bone differences between Strains (Balb/C vs C57B1/6) and mice (two mice per specie) were analysed.

2.5.2 Statistical analysis on the human bone

In most cases, both E_r and H were not normally distributed (Kolmogorov-Smirnov test, $p<0.05$), therefore Kruskal-Wallis tests (significance threshold equal to=0.05, Fig.54) were used to investigate potential differences. Exceptions were the data obtained for slice 4 (Kolmogorov-Smirnov test, p-value equal to=0.2 for both E_r and H) and Region 1 (E_r normally distributed, Kolmogorov-Smirnov test, p-value equal to=0.069). If a factor was significant, a Bonferroni Post Hoc analysis was done.

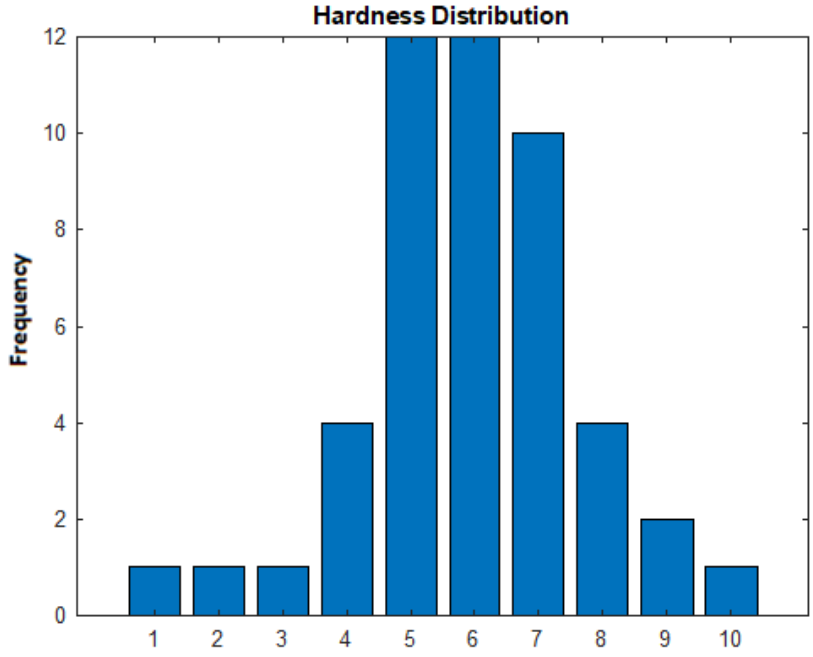

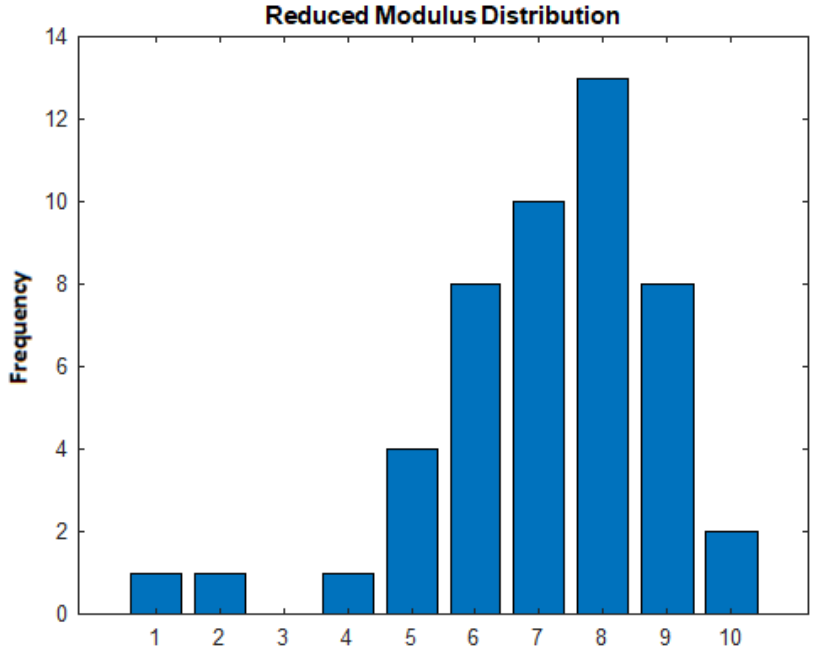

Figure 54: Example of not normally distributed data

Significant differences between different spatial locations (Region 1 and 2 and Sections 1, 2, 3 and 4) were investigated.

CHAPTER 3

RESULTS

3.1 Mechanical properties of the mouse tibia

In total, 542 indentations curves were obtained from mouse tibia specimens. Twelve of them were excluded from the data analysis because of the criteria mentioned in the previous chapter. As mentioned before, the statistical analysis on the cortical bone was made on four factors: mouse strain (C57B1/6 vs Balb/C), mouse subject (Mouse1 and Mouse2), sector (Anterior, Posterior, Medial and Lateral) and section (Distal, Central and Proximal). On the trabecular bone it was made using two factors: mouse strain and mouse subject.

3.1.1 Effect of "mouse strain"

No significant differences were observed between the two strains for the cortical bone (p=0.803 for E_r and p=0.078 for H). In Table 5, E_r and H for the two mouse strains are reported. Data is reported as mean ± standard deviation including both tibiae for each strain. For the trabecular bone, Kruskal-Wallis test for the factor strain showed significant differences for both E_r and H (p-value<0.001). In Table 5, the results (mean ± standard deviation) for E_r and hardness H for the two mouse strains are reported.

The indentation modulus (E_{ind}) and elastic modulus (E_b) for cortical and trabecular bone for the two strains are reported in the Table 1A in the appendix.

Effect of "mouse strain"				
Mechanical properties	**Bone**	**C57B1/6**	**Balb/C**	**Difference**
E_r (GPa)	**Cortical**	23.75 ± 7.14	25.08 ± 5.21	+5.3% NS
H (GPa)	**Cortical**	0.87 ± 0.25	0.96 ± 0.20	+9.4% NS
E_r (GPa)	**Trabecular**	16.50 ± 7.10	20.79 ± 4.12	+20.6% **
H (GPa)	**Trabecular**	0.62 ± 0.27	0.85 ± 0.18	+27.1% **

Table 5: Results from the indentations on the cortical bone and trabecular bone for the two different mouse strains.
*NS indicates that the differences were not statistically significant (p-value>0.078); ** indicates p<0.001*

3.1.2 Effect of "mouse subject"

There were some significant differences in the bone properties in function of the mouse subject. Mean values for E_r and H for the four mice are reported in the Table 6 (cortical and trabecular bone); the E_{ind} and E_b are reported in Tables 2A in the appendix.

For the cortical bone, C57B1/6 mice had significantly different mechanical properties (14.4% difference for E_r, p-value<0.001; 13.0% difference for H, p-value<0.001). For Balb/C mice only H was significantly different between the two subjects (4% difference, p-value=0.019).

The values obtained for the trabecular bone were significantly different between subjects, for C57B1/6 mice (p-value<0.001 for both E_r and H), but not for Balb/C mice (p-value=0.915 for E_r and p-value=0.823 for H).

Effect of "mouse subject"							
Mech prop	**Bone**	**X7L Specimen**	**X9L Specimen**	**Diff %**	**L1 Specimen**	**L3 Specimen**	**Diff %**
E_r (GPa)	**Cort**	27.56 ± 4.59	23.59 ± 6.30	-14.4 **	25.21 ± 5.83	26.64 ±3.83	+5.8 NS
H (GPa)	**Cort**	1.00 ± 0.17	0.87 ± 0.22	-13.0 **	1.01 ± 0.22	0.97 ± 0.16	+4.1 *
E_r (GPa)	**Trab**	21.26 ± 4.42	11.74 ± 6.02	-45 **	20.74 ± 4.65	20.84 ±3.59	+0.5 NS
H (GPa)	**Trab**	0.80 ± 0.14	0.44 ± 0.25	-43 **	0.84 ± 0.19	0.86 ± 0.17	+2.4 NS

Table 6: Results on the cortical bone and trabecular bone for the two different strains and mice.
** indicates p<0.05; ** indicates p<0.001; NS indicates that the differences were not statistically significant (p-value>0.082)*

3.1.3 Effect of "section"

There were significant differences in most mechanical properties in function of section (Kruskal-Wallis test for E_r and H). The labels "Distal, "Central", "Proximal" refer to the spatial position of each slice in the tibia. The mean values of E_r and H are presented in Fig.55 (error bars represent standard deviations). Mechanical properties for each slice (24 indentations/slice) for the cortical and trabecular bone for the four mice and for the two strains are reported in Tables 3A to 7A in the appendix. The E_{ind} and E_b mean values for the two strains and for the four mice are reported in Figures 15A to 19A in the appendix.

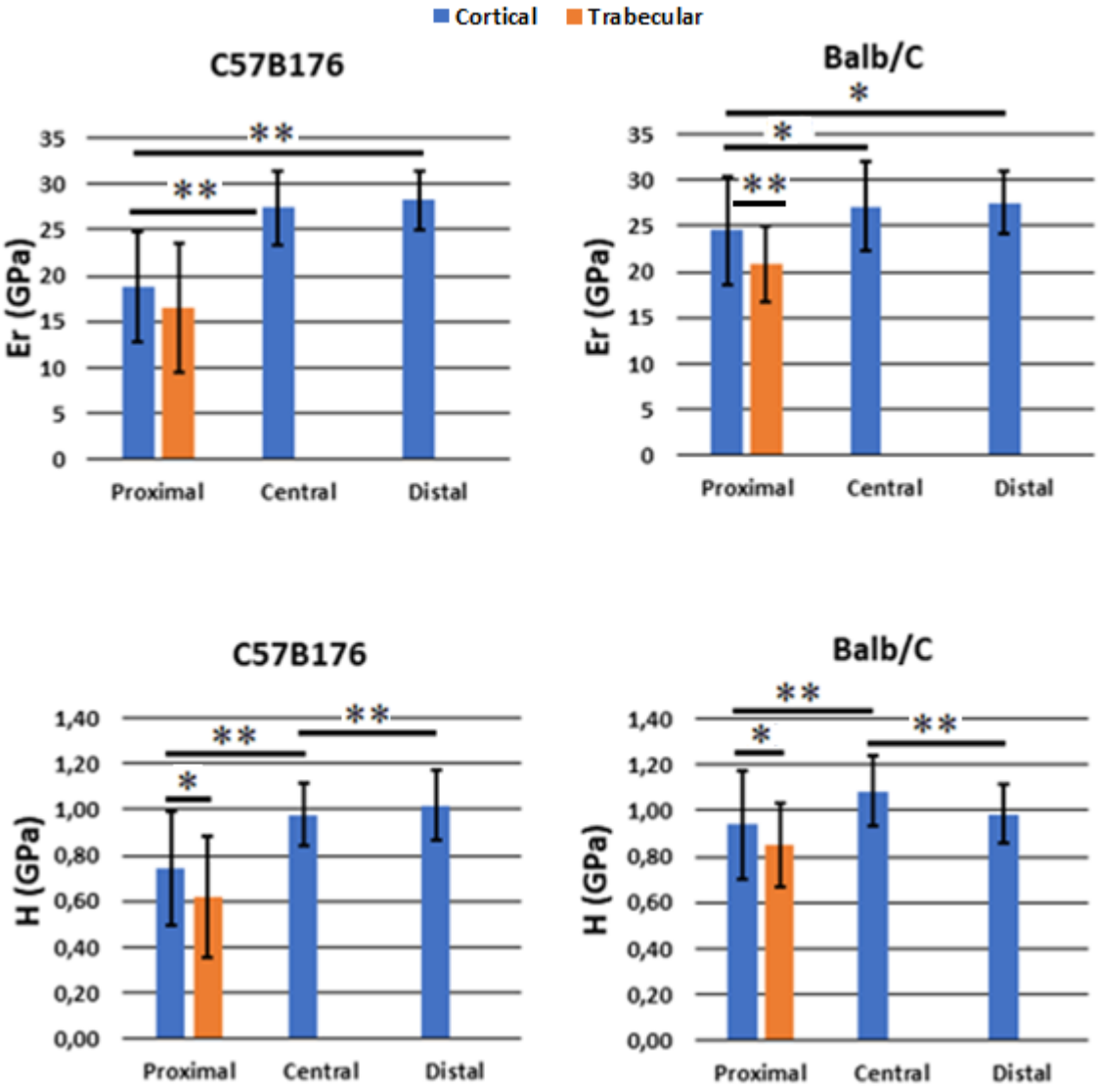

Figure 55: Reduced modulus (E_r) and hardness (H) for the two strains and three sections. Error bars represent standard deviations.
** indicates p<0.05; ** indicates p<0.001*

For C57B1/6 mice we found 31.8% difference in E_r between Proximal and Central sections (p-value<0.001); 33.9% difference E_r between Proximal and Distal sections (p-value<0.001); no significant difference between the E_r of the Central and Distal sections (p-value=0.332). Furthermore, we found 31.8% difference in H between Proximal and Central sections (p-value<0.001); 27.5% difference in H between Proximal and Distal sections (p-value<0.001); no difference between the H in the Central and Distal sections (p-value=0.095). The E_r and H in the distal and central sections were similar to each other and higher than that for proximal cortical bone, which was higher than that for the proximal

trabecular bone (11.8% difference for E_r, p-value=0.111; 16.2% difference for H, p-value=0.014).

For Balb/C mice, 10.7% difference in E_r between Proximal and Central sections (p-value=0.003), 9.1% difference in E_r between Proximal and Distal sections (p-value=0.013) and no significant difference between Central and Distal sections (p-value=0.639) were found. For the H we found: 14.9% difference between Proximal and Central sections (p-value<0.001); no significant difference between Proximal and Distal sections (p-value=0.878); 13.7% difference between Central and Distal sections (p-value<0.001). The E_r in the Distal and Central sections were similar to each other and higher than that for Proximal cortical bone which was higher than that measured in the Proximal trabecular bone (15.1% difference, p-value<0.001). The H values were similar in the Proximal and Distal sections and lower than that for Central cortical bone. We found also 9.6% difference between the H in the proximal cortical and trabecular bone (p-value=0.004).

3.1.4 Effect of "sector"

The labels "Anterior, "Posterior", "Medial" and "Lateral" refer to the spatial orientation in the tibia. The E_r and H histograms are reported in Fig.56. Reduced modulus (E_r) and hardness (H) for each sector (6 indentations/sector) for each strain and for each mouse are reported in Tables 8A-9A in the appendix. There were no significant differences (Kruskal-Wallis test) in E_r or H among the different sectors for Balb/C mice (p-value=0.782 for the reduced modulus and for hardness p-value=0.399). No significant differences were observed between the E_r measured among the different sectors for C57B1/6 mice (p-value=0.067). Only 8% difference in H between Posterior and Medial sectors (p-value=0.001) and 12% difference in H between Anterior and Medial sectors (p-value=0.006) were found. All the other differences were not significant (p-value>0.055).

The mechanical properties for each slice are reported in Tables 10A to 13A in the appendix.

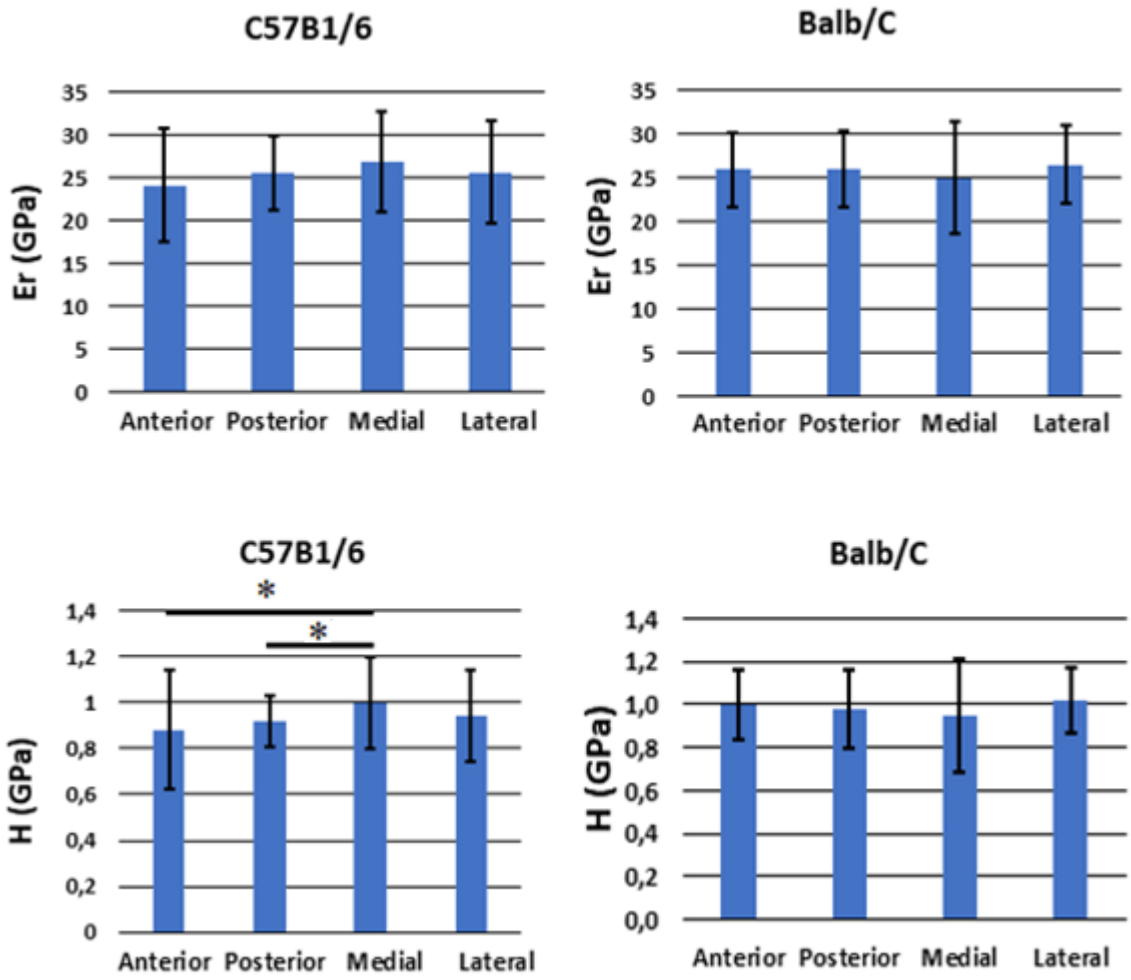

Figure 56: Reduced modulus (E_r) and hardness (H) for the two strains and four sectors. Error bars represent standard deviations.
** indicates p<0.05*

3.2 Mechanical properties of OI human bone

In total, 192 indentations were performed on the human specimen. One indentation was excluded from the data analysis based on the criteria mentioned in the previous chapter. Effect of two factors (Region, two different locations; Section, four slices) on the mechanical properties were tested. From pooled data the following mean values and standard deviations for the reduced modulus (E_r), hardness (H), indentation modulus (E_{ind}) and elastic modulus of the bone (E_b) were obtained:

OI human bone	
Mechanical properties	
E_r (GPa)	12.14 ± 5.79
H (GPa)	0.49 ± 0.21
E_{ind} (GPa)	12.30 ± 5.92
E_b (GPa)	11.20 ± 5.39

Table 7: Mechanical properties obtained from the analyses on OI human bone

3.2.1 Effect of "section"

From the statistical test the factor "section" was found to affect the mechanical properties of the bone tissue (Kruskal-Wallis test, $p<0.001$; Table 8).

Section	E_r (Gpa)	H (Gpa)	E_{ind} (Gpa)	E_b (Gpa)
1	11.85 ± 6.05	0.48 ± 0.21	12.01 ± 6.17	10.93 ± 5.61
2	8.11 ± 4.43	0.38 ± 0.20	8.18 ± 4.50	7.45 ± 4.10
3	12.85 ± 6.25	0.49 ± 0.23	13.03 ± 6.37	11.86 ± 5.80
4	15.75 ± 3.36	0.59 ± 0.15	15.98 ± 3.44	14.55 ± 3.13

Table 8: Mechanical properties obtained from each section. The reduced modulus E_r, hardness H, indentation modulus E_{ind} and elastic modulus E_b are presented. The results were obtained from the analyses on each slice of OI human bone.

The Post Hoc analyses (Tables 9) for E_r showed significance between each section. The differences are between the second section and all the others (p-value<0.001) and between the first and the fourth ones (p-value=0.022); the Post Hoc analyses for H showed significance between the second slice and the fourth one.

	Reduced modulus E_r		Hardness H	
Sections	**Difference**	**p-value**	**Difference**	**p-value**
2-1	31.6%	0.001	20.8%	0.357
2-3	36.9%	<0.001	22.4%	0.079
2-4	48.5%	<0.001	35.6%	<0.001
1-3	7.8%	1.000	2.0%	1.000
1-4	24.8%	0.022	18.6%	0.136
3-4	18.4%	0.231	16.9%	0.526

Table 9: Post Hoc analyses for E_r and H. The differences and the p-values between each section are presented

3.2.2 *Effect of "region"*

The values of E_r and H were also affected by the factor "region" ($p<0.001$, Fig.57; E_{ind} and E_b histograms are Fig.20A in the appendix).

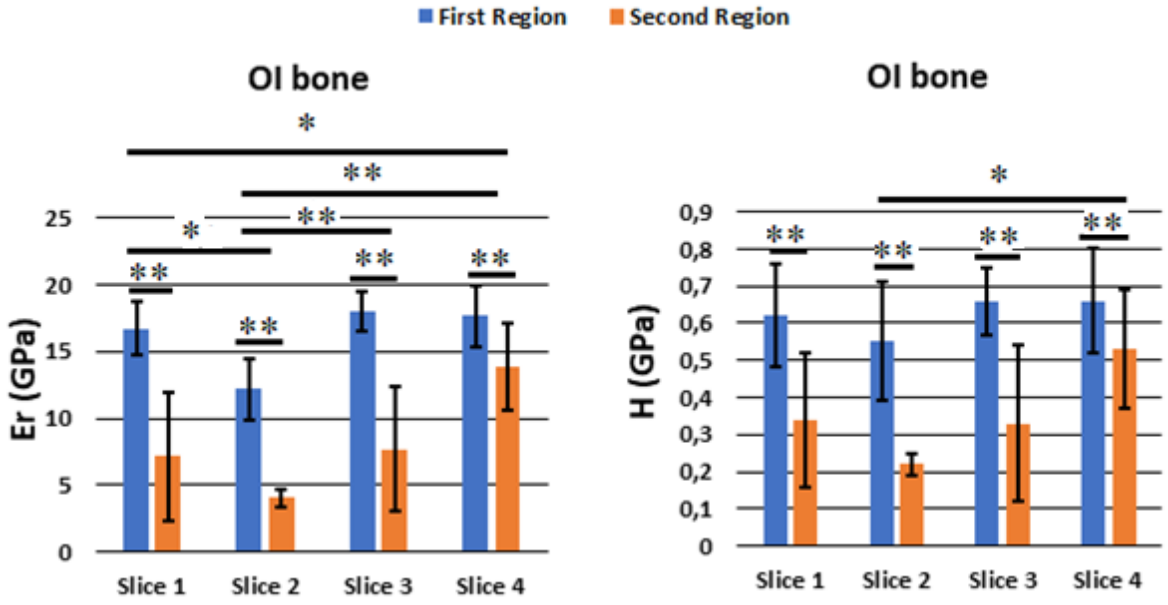

Figure 57: Reduced modulus (Er) and H histograms from the OI human bone. The histograms were divided by slice and region. Error bars represent standard deviations.

** indicates p<0.05; ** indicates p<0.001*

CHAPTER 4

DISCUSSION

The goal of this work was to develop a procedure to perform nanoindentation tests on bone tissue in order to study the elastic and inelastic properties of different bone structures. The main goal was to characterize the local reduced modulus, hardness, indentation modulus and elastic modulus of the bone.

We investigated the differences between strains (C57B1/6 vs Balb/C), spatial location (Proximal, Central or Distal regions) and spatial orientation (Anterior, Posterior, Medial and Lateral sections) on cortical and trabecular bone. We studied also the heterogeneous material properties across an OI specimen.

In this study, four mouse tibiae of two different strains (C57B1/6 and Balb/C) were analysed. An automated procedure was used to perform multiple nanoindentation tests on different spatial locations for each specimen. Both cortical and trabecular tissue were indented. Additionally, each specimen was cut into multiple slices, in order to investigate potential differences in the mechanical properties along the longitudinal direction (from the proximal to the distal end of the tibia). Moreover, potential differences in the cross-sections were investigated by indenting each slice in four locations: medial, lateral anterior and posterior sides.

Similarly, the human OI bone specimen was cut into multiple slices and each cross-section was indented in two different regions. The anatomical orientation of the specimen was unknown; however, this analysis was useful in order to investigate the potential variability of the bone mechanical properties in function of the spatial location.

In this work we mainly focused on the reduced modulus E_r and the hardness H. However, from the reduced modulus, the indentation modulus E_{ind} and the bone elastic modulus E_b were calculated too.

4.1 Discussion about the results from the mouse tibia

4.1.1 Effect of different parameters on the indentation properties

The comparison between the two strains showed that both E_r and H were higher for trabecular bone (20.6% and 27.1%, respectively) in the Balb/C mouse. Similar but not significant trend was found for cortical bone.

Three trabeculae of C57B1/6 mice showed low modulus and hardness values (E_r=4.47 GPa, E_r=6.39 GPa and E_r=8.70 GPa, H=0.21 GPa, H=0.39 GPa and H=0.27 GPa, respectively). These trabeculae may be less mineralized compared to the other indented trabeculae. In this study we used bones from young mice (16 weeks), which may have more heterogeneous bone structural units at different levels of mineralization.

Differences were found between different mice of the same strain. For the cortical bone, both E_r and H were significantly different between the two C57B1/6 mice, while the two Balb/C mice only showed different H. In fact, in one of the two C57B1/6 mice, some indentations on the fourth slice (proximal) showed lower values of mechanical properties than the other one (E_r between 5.66 GPa and 11.66 GPa, H between 0.08 and 0.58 GPa). The differences may be due to the intrinsic heterogeneity of material properties across the different subjects of a certain strain. Nevertheless, the very low sample size does not lead to a strong conclusion and more tests should be done to increase the number of tests.

Trabecular bone material properties were found to be different only for the C57B1/6 mice. These results suggest that at the tissue level the two strains have similar mechanical properties, while the potential inter-subject variability is greater. However, a limited number of specimens was used in this study (two per strain), therefore further analyses would be needed to support this conclusion.

Significant differences were found between longitudinal sections (Proximal, Central and Distal), for both E_r and H. The proximal section showed to be less stiff and less hard

than the other sections. The lower reduced modulus and hardness found at the proximal end of the tibia could be due to the fact that it is closer to the growth plate, where the tissue is younger and less mineralised. Further analyses with combined nanoindentation and mineralization measurements should be performed in order to clarify this effect. Differences between proximal cortical bone and trabecular bone were found for both E_r and H in C57B1/6 mice and for H in Balb/C mice. Trabecular tissue was found to be less stiff and less hard than cortical bone, in line with previous studies [31].

No significant differences were found between the Anterior, Posterior, Medial and Lateral sectors for Balb/C mice. Differences were found only for the hardness for C57B1/6 mice. The differences were between the medial sector and the posterior and the anterior ones. The higher values in the medial sector could be due to the curvature or the shape of the bone.

4.1.2 Comparison with literature

For the nanoindentation procedure we used a similar procedure reported in literature for indentation of mouse femurs (Casanova et al. (2017)). In that reference paper, only Balb/C bones from older mice (22 weeks) were analysed. The specimens tested in this study were younger (16 weeks) and, therefore, a lower reduced modulus was expected to be found. Conversely higher values of reduced modulus were found (E_r=18.6 GPa in Casanova et al.; E_r=25.08 GPa in our study).

This is probably due to the fact that, while the indentation parameters were the same, the anatomical site (femur vs tibia) and the condition of the tissue (hydrated vs dehydrated) were different. In fact, in the reference paper the specimens were rehydrated in PBS at room temperature for 30 minutes before the nanoindentation procedure. It has been reported in literature that the rehydrated specimens show a lower reduced modulus and hardness compared to dry specimens. Wolfram et al. (2010) showed that the reduced modulus was 20-30% lower in the rehydrated specimens extracted from the human vertebra. The reduced modulus obtained in Casanova et al. for the three sections (proximal, central and distal) and the E_r obtained in our work are summarised in Table 10. The percentage difference between the E_r found in the two studies for each section is also reported. As expected, the difference

between hydrated (Casanova et al.) and dehydrated (our study) tissue is in line with Wolfram et al.

	Casanova et al. 2017	Balb/C in our study	
Section	**E_r (GPa)**	**E_r (GPa)**	**Difference**
Cort Prox	19.40 ± 3.0	26.73 ± 2.81	+27.4%
Cort Cent	20.10 ± 1.9	27.12 ± 4.87	+25.9%
Cort Dist	16.40 ± 3.0	24.50 ± 5.84	+33.1%
Total mean	18.60 *	25.08 ± 5.21	+25.9%

Table 10: Comparison between the two Er found in Casanova et al. and in our study for each section

** E_r is reported without standard deviation due to lack of information in the paper*

Other studies reporting experiments performed in a dry environment and along the longitudinal directions found results consistent with our data. Our results are in line with the values obtained for bovine bone [31-44-45], despite the structural differences between the two species.

Lucchini et al. (2011) and Carnelli et al. (2013) reported that on one adult bovine the indentation moduli were E_{ind}=22.30 ± 1.78 GPa and E_{ind}=19.73 ± 0.73 GPa, respectively (for the cortical bone), which are comparable with our results (for the C57B1/6 E_{ind}=24.30 ± 7.40 GPa and for the Balb/C E_{ind}=25.66 ± 5.43 GPa). Similarly, Lucchini et al. reported hardness of H=0.73 ± 0.04 GPa (in this study, for the C57B1/6 H=0.87 ± 0.25 GPa and for the Balb/C H=0.96 ± 0.20 GPa). To be noted is the higher variability in our results compared to those from the mentioned literature. This difference could be due to the higher heterogeneity in the mouse tibia material properties compared to that in the bovine femur. Furthermore, in Lucchini's work, the specimen polishing was performed using a metallographic polishing wheel and more steps with successively smaller Al_2O_3 particles were employed, which could explain the smaller standard deviations in the results. It should be also noted that there were some differences in the indentation procedure (loading/unloading rates were 20 nm/s and 100 nm/s vs 300 µN/s and 900 µN/s; maximum penetration depths 450 nm in Lucchini et al. or 300 nm in Carnelli et al. vs approximately 500 nm in this study).

Our results are also comparable to those obtained with different experimental techniques. Dall'Ara et al. (2015) tested the bovine femurs (18 months old) using depth sensing micro-indentation at the bone structural unit level with a penetration depth equal to 2.5 μm. Despite the penetration depths and other indentation parameters were different, the obtained values of indentation modulus were similar to those found in the present study (E_{ind}=24.37 ± 2.5 GPa vs 24.30 ± 7.40 GPa (C57B1/6) and 25.66 ± 5.43 GPa (Balb/C)).

There are also some similarities with the results obtained on human bone studies.

For example, in the work of Zysset et al. (1999) on human femurs at the lamellar level (penetration depth equal to 500 nm, loading/unloading rate 10 nm/s; tissue condition: specimens rehydrated before indentations), the average elastic modulus of diaphyseal cortical bone was E_b=20.1 ± 5.4 GPa, similar to the results of this study on mice cortical bone (E_b=22.11 ± 6.74 GPa for C57B1/6 mice and E_b=23.35 ± 4.94 GPa for the Balb/C mice). They also tested trabecular bone from human femoral neck. They found a mean elastic modulus of E_b=11.4 ± 5.6 GPa, which is lower than that obtained in this study (for the C57B1/6 E_b=15.27 ± 6.64 GPa and for the Balb/C E_b=18.87 ± 4.73 GPa). Considering the different tissue conditions (20-30% difference between dehydrated and re-hydrated tissue) the comparison of the results suggest that while the elastic modulus of mice trabecular bone is probably similar to the elastic modulus of human trabecular bone (11.4 GPa vs 11.5 GPa (C57B1/6) and 14.2 GPa (Balb/C), corrected for the effect of re-hydration), the elastic modulus for cortical bone in mice may be lower than the one found in humans (21.2 GPa vs 16.6 GPa (C57B1/6) and 17.5 GPa (Balb/C), corrected for the effect of re-hydration).

Spiesz et al. (2013) performed nanoindentation tests on human femurs (tissue condition: dehydrated specimen) in displacement control until 500 nm depth using a loading/unloading rate of 40 nm/s and a holding time of 30 s, similarly to our experimental conditions. The measured indentation modulus was E_{ind}=23.99 ± 5.12 GPa, in line with our results.

Comparison with literature						
Authors	**Specie**	**Site**	**Bone type**	**Penetr depth**	**Tissue condition**	**Results (GPa)**
Lucchini (2011)	Bovine	Tibia	Cortical	450nm	Dehydrated	E_{ind}=22.30 (±1.78)
Carnelli (2013)	Bovine	Tibia	Cortical	300nm	Dehydrated	E_{ind}=19.73 (±0.73)
Dall'Ara (2015)	Bovine	Femur	Cortical	2.5µm	Dehydrated	E_{ind}=24.37 (±2.50)
Zysset (1999)	Human	Femur	Cortical/ Trab	500nm	Rehydrated	E_{ind}=22.09 cortical E_{ind}=12.51 trab
Spiesz (2013)	Human	Femur	Cortical	500nm	Dehydrated	E_{ind}=23.99 (±5.12)
Casanova (2017)	Mouse	Femur	Cortical	500nm	Rehydrated	E_r=18.60 *
Our study (2019)	Mouse	Tibia	Cortical	500nm	Dehydrated	E_{ind}=24.30 (±7.40) *C57B1/6* E_{ind}=25.66 (±5.43) *Balb/C*

Table 11: Summarising of E_{ind} results obtained from the different studies

** E_r is reported due to lack of information in the paper*

4.2 Discussion about the results from the human bone

The mechanical properties measured with indentations tests showed high heterogeneity across the specimen.

The mechanical properties in the four tested sections and in the different sub-regions were significantly different. In particular, one of the sections was significantly different from all the others. A possible explanation could be due to differences in local porosity, mineral arrangements and collagen properties (Fig.58). A limitation is that we did not know the exact location of origin of this bone specimen.

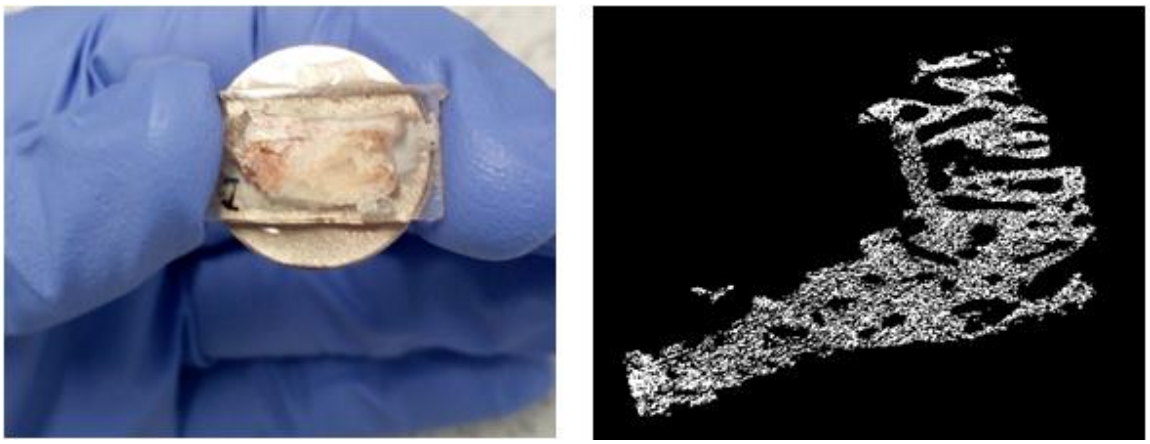

Figure 58: Second section of the human specimen (left) and corresponding microCT cross-section (right)

The difference between the first and the fourth section could depend on the morphological differences between the two sections. In fact, the fourth section was characterised by the presence of more compact tissue and more cortical bone compared to the first one (Fig.59).

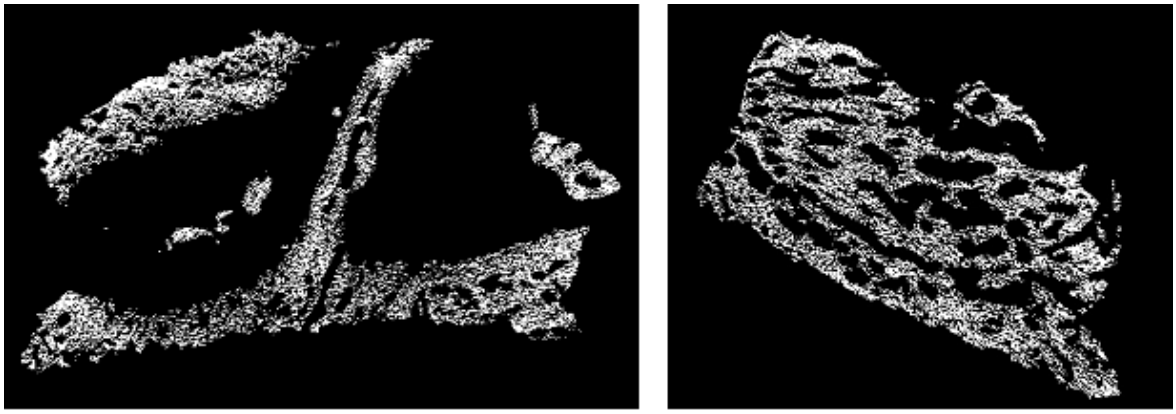

Figure 59: microCT cross-section of the first section (left) and fourth section (right)

4.2.1 Comparison with literature

In OI patients, the production and assembly of collagen fibrils that form bone are different. Because OI collagen fibrils serve as a model for mineralization, the mineralization of OI is also compromised and consequently OI has an effect on the tissue properties. Traub et al. reported that the compact lamellar bone can be found in various OI bones, but in a few and disconnected bones regions.

Numerous studies employed the OI murine model, for example in the study of Grabner et al. (2001), they showed that the bone material in the *oim* model has reduced biomechanical quality. They reported also the indicators of lower maturity and reduced crystallinity in OI bone.

The results obtained from the human OI specimen tested in this study showed E_r=12.14 ± 5.79 GPa and H=0.49 ± 0.21 GPa. These mechanical properties are lower than the values of elastic modulus and hardness found for healthy adult bone (E_r of approximately 20 GPa [31-37-38] and H between 0.234 and 0.760 GPa [31]). It should be noted that the specimen characterised in this study was collected from a 9-year old boy and therefore the differences may be due to both age and disease. It is hard to deepen the effect of age because there are no studies in literature about indentations on children bone.

Albert et al. (2013) performed indentation on OI type III and OI type I specimens from the femur or the tibia of paediatric patients (5-18 years old, N=12). They performed indentations with penetration depth of 2000 nm and on dehydrated tissue. They found that OI type III bone had E_r=16.3 GPa and OI type I had E_r=17.5 GPa. Our results were 25.5% lower than those found for the OI type III and 30.6% lower than OI type I. This difference could potentially be due to the different tested anatomical site (lower limbs long bones vs upper limbs in this study), dehydration method or age.

Similar results were also found in Fan's et al., although the testing procedure was different (loading/unloading rates of 300 μN/s and a peak load of 3000 μN). They collected 8 specimens from OI type III patients (aged 3.2-12.4 years) from lower limbs and reported E_b=15.22 ± 1.94 GPa and H=0.42 ± 0.04 GPa (in our work E_b=11.20 ± 5.39 GPa and H=0.49 ± 0.21 GPa).

The large difference between the results obtained in this study and those obtained in Fan et al. (2007), (42% difference in mean E_b and 27% difference in mean H) could be due to the disease characteristics and the different anatomical site. In fact, they indented the iliac crest, the femur and the tibia; in our study we indented the upper limb.

CHAPTER 5

CONCLUSION

The main objective of this work was to define a procedure for analysing the local elastic and inelastic properties of bone tissue in different regions within different types of specimens for both clinical and pre-clinical applications. Therefore, a new protocol was developed. This protocol was applied to mouse bones (from two different strains C57B1/6 and Balb/C) and to pathological human bone, obtained from an OI patient. The main goal of this work was to obtain from the nanoindentation measures the values of reduced modulus, hardness, indentation modulus and elastic modulus of the bone in different subregions. We performed the nanoindentations first on the mouse tibiae to fine-tune method and to avoid wasting extremely rare OI specimens. We investigated the repeatability on tightly repeatable bone samples (same bone from same mouse strain) and the potential differences between strains, spatial location or spatial orientation. The nanoindentation on an OI specimen had as goal to characterise the heterogeneous material properties across the specimen.

The procedure for performing nanoindentations tests (sample preparation, mechanical testing, acquisition of the data and post-processing of the results) was developed and is now a standard procedure applied in the host laboratory (Insigneo institute for in silico medicine and Nanolab, University of Sheffield, UK).

The results obtained from mouse bones are in line with the literature. We found that the difference between the mechanical properties measured in different mouse strains was not statistically significant, instead significant differences were found between different mice of the same strain. It the future, it will be necessary to increase the number of the

specimens to better understand the potential inter-subject variability (within the same strain). Moreover, the proximal section of the mouse tibia was significantly less stiff and less hard than the central and distal ones. Finally, no significant differences were found between the anterior, posterior, medial and lateral sectors.

Although few specimens were tested, a large heterogeneity of bone tissue properties was highlighted by this study underlining the importance of properly characterise the different tissues with a large number of indentations distributed in different regions of the specimens.

This procedure can be now used in pre-clinical studies to assess also the effect of age, pharmacological treatments and/or the response to mechanical stimuli on the local material properties of the bone tissue. Moreover, the measured mechanical properties can be used to populate computational models (e.g. finite element models) used to estimate the structural mechanical properties of the investigated bones.

The results obtained from OI human bone specimens are in line with the literature too. We found that the mechanical properties were not homogeneous in our specimen. In fact, there were significant statistical differences between the two regions and the four sections considered in the study. In this work only one OI sample was tested, but a series of indentations have already been performed on different parts of the tissue. The same analyses may be performed on other patients with other ages or with other types of pathologies. The application of this approach will allow researchers to measure the mechanical properties of bone tissue extracted from biopsy in children with different OI forms and correlated them with structural properties (measured with micro computed tomography) and local mineralization (measured with back-scattered emission microscopy or spectroscopy). Moreover, nanoindentations on OI specimen may be useful to investigate potential differences between healthy and pathological bone, for example investigating the effect of treatments.

REFERENCES

1. Cefalì G., Merlin S. (2011-2012). Tesi di Laurea Magistrale: Caratterizzazione Meccanica di Tessuto Osseo Corticale mediante Nanoindentazione ciclica a carichi multipli. Politecnico di Milano, Corso di Laurea Magistrale in Ingegneria Biomedica, Biomeccanica e Biomateriali.
2. https://www.visiblebody.com/learn/skeleton/types-of-bones
3. Prof. Ing. Luca Cristofolini, (2017-2018). Dispense di Meccanica dei Tessuti Biologici. Cap.3 - Tessuti connettivi calcificati. Università di Bologna, Corso di Laurea Magistrale in Ingegneria Biomedica, Meccanica dei Tessuti Biologici.
4. Zysset, P. K. (2009). Indentation of bone tissue: a short review. Osteoporosis Int, 1049–1055.
5. Prof. Ing. Luca Cristofolini, (2017-2018). Dispense di Meccanica dei Tessuti Biologici. Cap.2 - Classificazione, composizione e struttura dei tessuti. Università di Bologna, Corso di Laurea Magistrale in Ingegneria Biomedica, Meccanica dei Tessuti Biologici.
6. Bedini R., Marinozzi F., Pecci R., Angeloni L., Zuppante F., Bini F., Marinozzi A., (2010). Analisi microtomografica del tessuto osseo trabecolare: influenza della soglia di binarizzazione sul calcolo dei parametri istomorfometrici. Rapporti Istisan 10/15 (Istituto superiore di sanità).
7. Alessandroni E., Marasco R., Pepe V. (2017-2018). Tesina per corso di Meccanica dei Tessuti Biologici: Caratterizzazione a flessione di osso corticale bovino: elasticità, componente organica e inorganica. Università di Bologna, Corso di Laurea Magistrale in Ingegneria Biomedica, Meccanica dei Tessuti Biologici.
8. Wagermaier W, Klaushofer K, Fratzl P, (2015). Fragility of bone material controlled by internal interfaces. Calcif Tissue Int.; 97(3): 201–12.
9. Weiner S, Traub W, Wagner HD. Lamellar bone: structure-function relations. J Struct Biol. 1999;126(3):241–55.
10. F. Gaynor Evans (1969). The mechanical properties of bone.
11. Antonella Forlino, Joan C Marini (November 3, 2015). Osteogenesis imperfecta. Seminar Published online http://dx.doi.org/10.1016/. Department of Molecular

Medicine, Biochemistry Unit, University of Pavia, Pavia, Italy (A Forlino PhD); and Bone and Extracellular Matrix Branch, Eunice Kennedy Shriver National Institute of Child Health and Human Development, National Institutes of Health, Bethesda, MD, USA (J C Marini MD).

12. Marshall C. J., Arundel P., Mushtaq T., Offiah A. C., Pollitt R.C., Bishop N.J., Balasubramanian M., (2016). Diagnostic Conundrums in Antenatal Presentation of a Skeletal Dysplasia with Description of a Heterozygous C-Propeptide Mutation in COL1A1 Associated with a Severe Presentation of Osteogenesis Imperfecta. American Journal of medical genetics.

13. Bishop N., (2016). Bone Material Properties in Osteogenesis imperfecta. Journal of Bone and Mineral Research, Vol. 31, No. xx, pp 1-10.

14. Warman ML, Cormier-Daire V, Hall C, Krakow D, Lachman R, LeMerrer M, Mortier G, Mundlos S, Nishimura G, Rimoin DL, Robertson S, Savarirayan R, Sillence D, Spranger J, Unger S, Zabel B, Superti-Furga A. 2011. Nosology and classification of genetic skeletal disorders: 2010 revision. Am J Med Genet Part A 155A:943–968.

15. F.S. Van Dijk and D.O. Sillence, (12 February 2014). Osteogenesis Imperfecta: Clinical Diagnosis, Nomenclature and Severity Assessment. American Journal of medical genetics.

16. Sillence DO, Barlow KK, Garber AP, Hall JG, Rimoin DL. 1984. Osteogenesis imperfecta type II delineation of the phenotype with reference to genetic heterogeneity. Am J Med Genet 17:407–423.

17. Glorieux FH, Rauch F, Plotkin H, Ward L, Travers R, Roughley P, Lalic L, Glorieux DF, Fassier F, Bishop NJ., (2000). Type V osteogenesis imperfecta: A new form of brittle bone disease. J Bone Miner Res 15:1650–1658.

18. Steiner RD, Adsit J, Basel D. 2013. COL1A1/2-Related Osteogenesis Imperfecta. Genere views [www.ncbi.nlm.nih.gov/books/NBK1295].

19. Kuurila K, Kaitila I, Johansson R, Grenman R. 2002. Hearing loss in Finnish adults with osteogenesis imperfecta: A nationwide survey. Ann Otol Rhinol Laryngol 111:939–946.

20. Sillence DO, Barlow KK, Cole WG, Dietrich S, Garber AP, Rimoin DL., (1986). Osteogenesis imperfecta type III. Delineation of the phenotype with reference to genetic heterogeneity. Am J Med Genet 23:821–832.

21. Rauch F, Travers R, Plotkin H, Glorieux FH, (2002) The effects of intravenous pamidronate on the bone tissue of children and adolescents with osteogenesis imperfecta. J Clin Invest 110:1293–1299.

22. Paterson CR, McAllion S, Stellman JL, (1984) Osteogenesis imperfecta after the menopause. N Engl J Med 310:1694–1696.

23. L. A. Bradbury, S. Barlow, F. Geoghegan, R. A. Hannon, S. L. Stuckey, J. A. H. Wass, R. G. G. Russell, M. A. Brown, E. L. Duncan, (2012). Risedronate in adults with osteogenesis imperfecta type I: increased bone mineral density and decreased bone turnover, but high fracture rate persists. Osteoporos Int, 285-294.

24. Eric S. Orwoll, Jay Shapiro, Sandra Veith, Ying Wang, Jodi Lapidus, Chaim Vanek, Jan L. Reeder, Tony M. Keaveny, David C. Lee, Mary A. Mullins, Sandesh C.S. Nagamani, and Brendan Lee, (February 2014). Evaluation of teriparatide treatment in adults with osteogenesis imperfecta. The Journal of Clinical Investigation, vol. 124, num. 2: 491-498.

25. Maximilien Vanleene, Alexandra Porter, Pascale-Valerie Guillot, Alan Boyde, Michelle Oyen, Sandra Shefelbine, (2012). Ultra-structural defects cause low bone matrix stiffness despite high mineralization in osteogenesis imperfecta mice. Bone 50, 1317–1323.

26. Chipman SD, Sweet HO, McBride DJ, Davisson MT, Marks SC, Shuldiner AR, et al. Defective pro alpha 2(I) collagen synthesis in a recessive mutation in mice: a model of human osteogenesis imperfecta. Proc Natl Acad Sci U S A 1993; 90:1701–5.

27. Ascenzi, A., (1988). The micromechanics versus the macromechanics of cortical bone-A comprehensive presentation. Journal of Biomechanical Engineering 110, 357-363.

28. Vashishth D, Tanner KE, Bonfield W., (2001). Fatigue of cortical bone under combined axial-torsional loading. J. Orthop. Res. 19, 414–420.

29. Hengsberger S, Kulik A, Zysset Ph, (2002b) Nanoindentation discriminates the elastic properties of single human bone lamellae under dry and physiological conditions. Bone.

30. https://en.wikipedia.org/wiki/Berkovich_tip

31. Philippe K. Zysset, X. Edward Guo, C. Edward Hoffler, Kristin E. Moore, Steven A. Goldstein (1999). Elastic modulus and hardness of cortical and trabecular bone lamellae measured by nanoindentation in the human femur. Journal of Biomechanics 32, 1005-1012.

32. Z. Fan, J.G. Swadener, J.Y. Rho, M.E. Roy, G.M. Pharr (2002). Anisotropic properties of human tibial cortical bone as measured by nanoindentation. Journal of Orthopaedic Research 20, 806-810.

33. Mercer C, He MY, Wang R, Evans AG. 2006 Mechanisms governing the inelastic deformation of cortical bone and application to trabecular bone. Acta Biomater. 2, 59–68.

34. A.J. Bushby, V.L. Ferguson, A. Boyde, (Jan 2004). Nanoindentation of bone: Comparison of specimens tested in liquid and embedded in polymethylmethacrylate. J. Mater. Res., Vol. 19, No. 1, 249-259.

35. Zioupos P., (2001) Accumulation of in-vivo fatigue microdamage and its relation to biomechanical properties in ageing human cortical bone. J Microsc; 201:270–8.

36. Cheng Y-T, Cheng C-M (2005) Relationships between initial unloading slope, contact depth, and mechanical properties for conical indentation in linear viscoelastic solids. J Mater Res 20 (4):1046–1053.

37. Dall'Ara E., Schmidt R., Zysset P., (2012). Microindentation can discriminate between damaged and intact human bone tissue. Bone 50, 925–929.

38. Dall'Ara E., Karl C, Mazza G., Franzoso G., Vena P., Pretterklieber M., Pahr D., Zysset P., (2013). Tissue properties of the human vertebral body sub-structures evaluated by means of microindentation. Journal of the mechanical behavior of biomedical materials 25, 23-32.

39. Andreas G. Reisinger, Dieter H. Pahr, Philippe K. Zysset, (2011). Principal stiffness orientation and degree of anisotropy of human osteons based on nanoindentation in

three distinct planes. Journal of the Mechanical Behavior of Biomedical Materials 4, 2113-2127.

40. Fan Z., Smith P.A., Eckstein E. C., Harris G. F., (2006). Mechanical properties of OI type III bone tissue measured by Nanoindentation. Wiley InterScience Periodicals, Inc.

41. Holstein JH, Garcia P, Histing T, Klein M, Becker SC, Menger MD, Pohlemann T., (2011). Mouse models for the study of fracture healing and bone regeneration, pp. 175–191. London, UK: Springer.

42. Casanova M., Balmelli A., Carnelli D., Courty D., Schneider P., Müller R., (2017). Nanoindentation analysis of the micromechanical anisotropy in mouse cortical bone. Royal Society Open Science.

43. Lucchini R., Carnelli D., Ponzoni M., Bertarelli E., Gastaldi D., Vena P., (2011). Role of damage mecheanics in nanoindentation of lamellar bone at multiple sizes: Experiments and numerical modeling. Journal of the Mechanical Behavior of Biomedical Materials 4, 1852-1863.

44. Carnelli D., Vena P., Dao M., Ortiz C., Contro R., (2013). Orientation and size-dependent mechanical modulation within individual secondary osteons in cortical bone tissue. Journal of the Royal Society.

45. Dall'Ara E., Grabowski P., Zioupos P., Viceconti M, (2015). Estimation of local anisotropy of plexiform bone: Comparison between depth sensing micro-indentation and Reference Point Indentation. Journal of Biomechanics 48, 4073–4080.

46. Albert C., Jameson J., Toth J. M., Smith P., Harris G. (2013). Bone properties by nanoindentation in mild and severe osteogenesis imperfecta. Clinical Biomechanics 28, 110–116.

47. Fan Z., Smith P. A., Harris G. F., Rauch F., Bajorunaite R., (2007). Comparison of Nanoindentation Measurements Between Osteogenesis Imperfecta Type III and Type (Femur/Tibia versus Iliac Crest). Connective Tissue Research, 48, 70–75.

48. Mary L Bouxsein, Stephen K Boyd, Blaine A Christiansen, Robert E Guldberg, Karl J Jepsen, and Ralph Müller (July 2010). Guidelines for Assessment of Bone

Microstructure in Rodents Using Micro-Computed Tomography. Journal of Bone and Mineral Research, Vol. 25, No. 7, pp 1468–1486.

49. Martin-Badosa E, Amblard D, Nuzzo S, Elmoutaouakkil A, Vico L, Peyrin F. Excised bone structures in mice: imaging at three-dimensional synchrotron radiation micro CT. Radiology. 2003; 229:921– 928.

50. Jameson J., Albert C., Smith P., Molthen C., Harris G. F., (2011). Micro-CT Characterization of Human Trabecular Bone in Osteogenesis Imperfecta. Medical Imaging: Biomedical Applications in Molecular, Structural, and Functional Imaging.

51. Ranzoni A. M., Corcelli M., Arnett T. R., Guillot P. V., (2018). Micro-Computed tomography reconstructions of tibiae of stem cell transplanted osteogenesis imperfecta mice. SCIENTIFIC DATA | 5:180100 | DOI: 10.1038/s.

52. Oliviero Sara (2019). Non-invasive prediction of bone mechanical properties of the mouse tibia in longitudinal preclinical studies. PhD thesis, University of Sheffield.

53. Oliviero S, Lu Y., Viceconti M., Dall'Ara E. (2017). Effect of integration time on the morphometric, densitometric and mechanical properties of the mouse tibia. Journal of Biomechanics 65: 203-211.

54. Wolfram U., Wilke H.-J., Zysset P., (2010). Rehydration of vertebral trabecular bone: Influences on its anisotropy, its stiffness and the indentation work with a view to age, gender and vertebral level. Bone 46, 348-354.

55. Traub W, Arad T, Vetter U, Weiner S. Ultrastructural studies of bones from patients with osteogenesis imperfecta. Matrix Biol 1994; 14:337–345.

56. Grabner R, Landis WJ, Roschger P, Rinnerthaler S, Peterlik H, Klaushofer K, Fratzi P. Age- and genotype-dependence of bone material properties in the osteogenesis imperfecta murine model (oim). Bone 2001; 29:453– 457.

APPENDIX

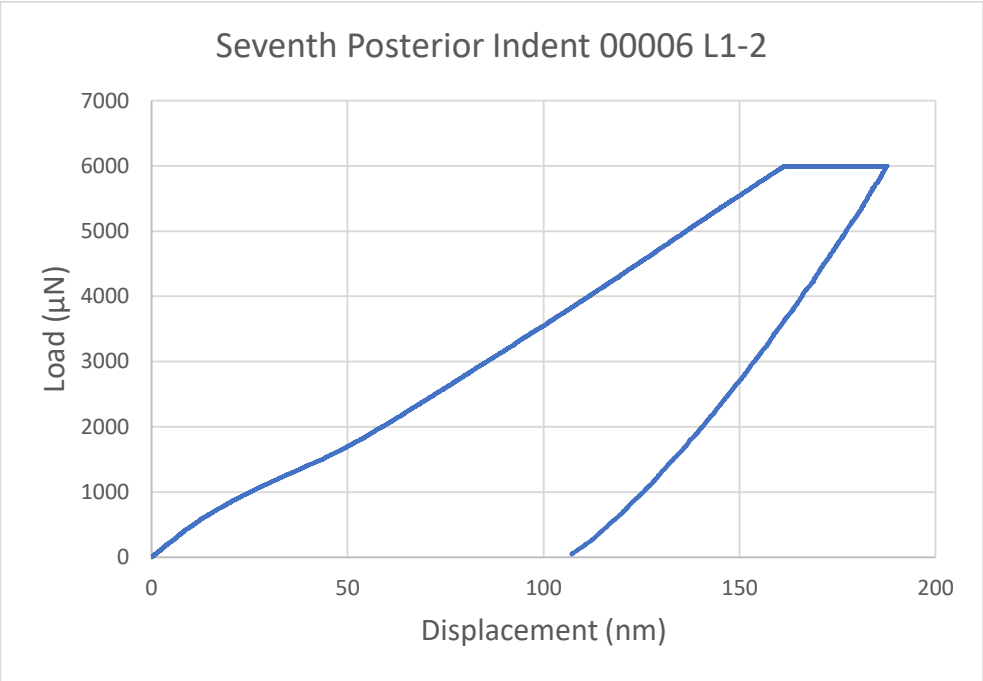

Figure 1A: Load-Displacement curve of a wrong indentation. Balb/C (L1), second slice (the distal one). The indentations have been made on the right side of the bone in the posterior part of the tibia. The wrong curve concerns the first indentation at the top left

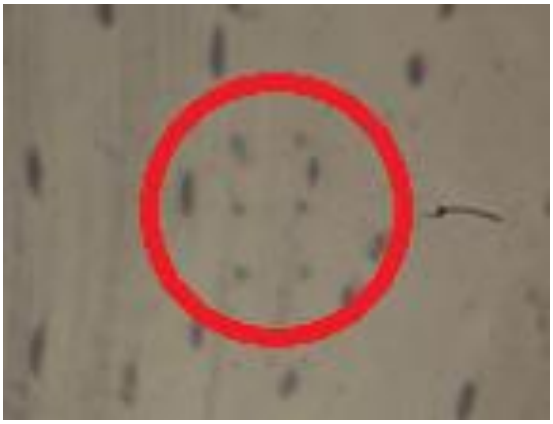

Figure 2A: Balb/C (L1), second slice (the distal one). The indentations are made on the right side of the bone in the posterior part of the tibia. The wrong curve concerns the first indentation at the top left

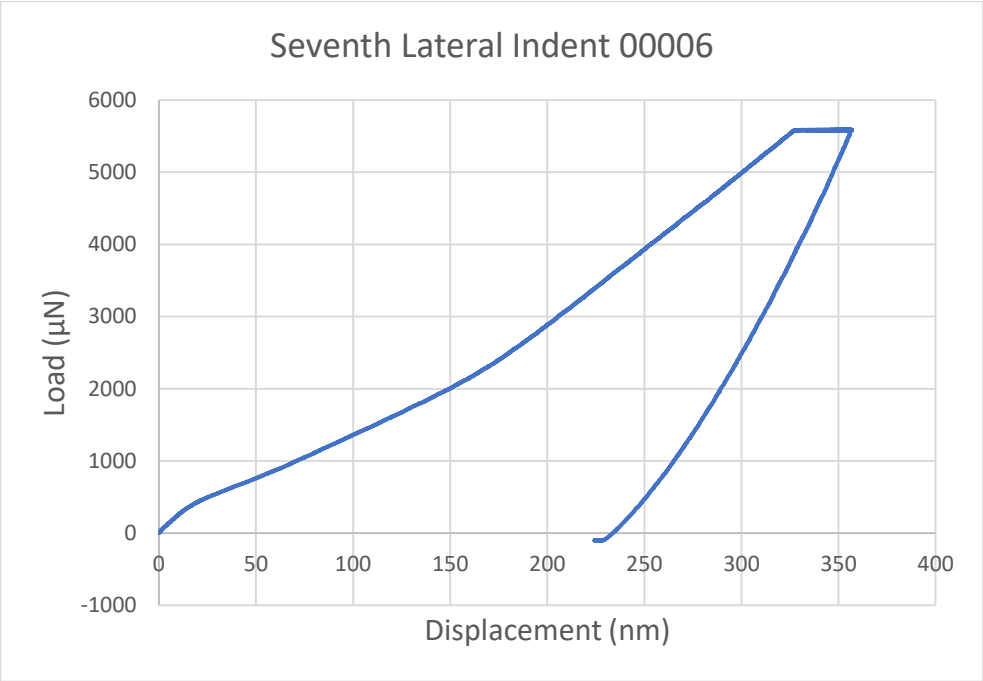

Figure 3A: Load-Displacement curve of a wrong indentation. Balb/C (L1), second slice (the distal one). The indentations have been made on the right side of the bone in the posterior part of the tibia. The wrong curve concerns the first indentation at the top left

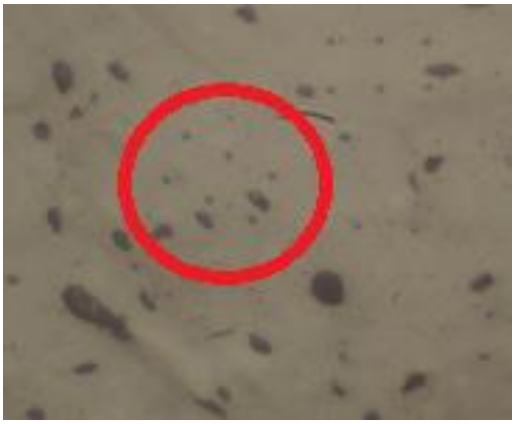

Figure 4A: Balb/C (L1), second slice (the distal one). The indentations are made on the right side of the bone in the posterior part of the tibia. The wrong curve concerns the first indentation at the top left

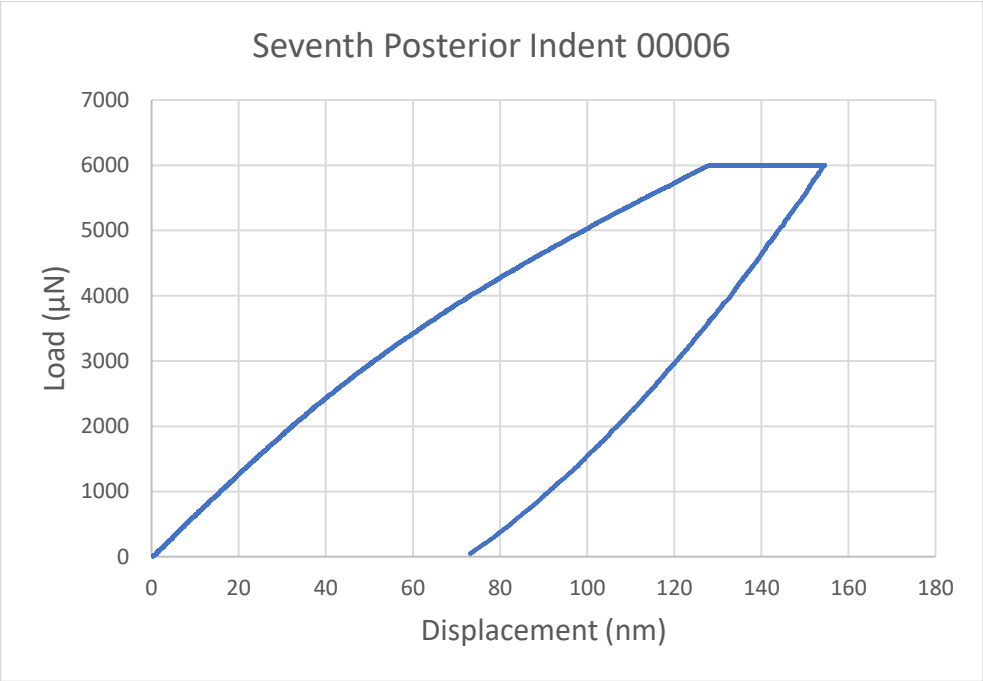

Figure 5A: Load-Displacement curve of a wrong indentation. Balb/C (L1), second slice (the distal one). The indentations have been made on the right side of the bone in the posterior part of the tibia. The wrong curve concerns the first indentation at the top left

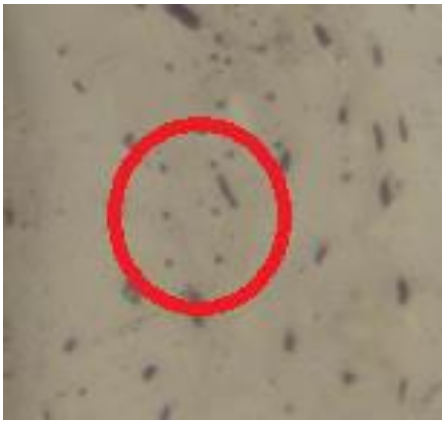

Figure 6A: Balb/C (L3), second slice (the central one). The indentations are made on the right side of the bone in the posterior part of the tibia. The wrong curve concerns the first indentation at the top left

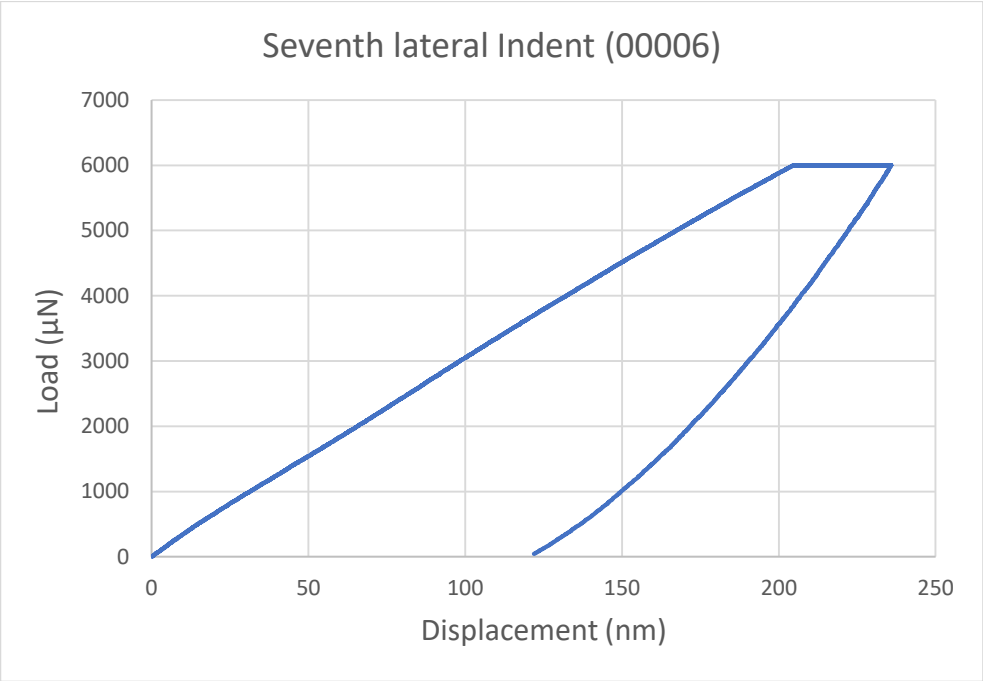

Figure 7A: Load-Displacement curve of a wrong indentation. Balb/C (L1), second slice (the distal one). The indentations have been made on the bottom of the bone in the lateral part of the tibia. The wrong curve concerns the first indentation at the top left

Figure 8A: C57B1/6 (X9L), third slice (the central one). The indentations are made on the bottom of the bone in the lateral part of the tibia. The wrong curve concerns the first indentation at the top left

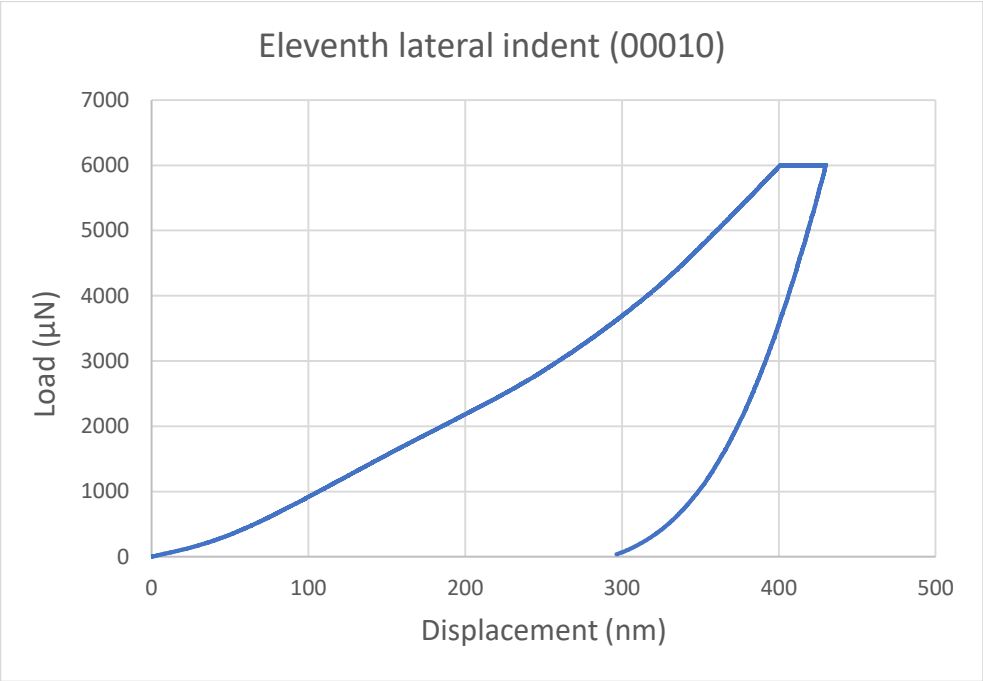

Figure 9A: Load-Displacement curve of a wrong indentation. Balb/C (L1), second slice (the distal one). The indentations have been made on the bottom of the bone in the lateral part of the tibia. The wrong curve concerns the indentation at the center of the second line

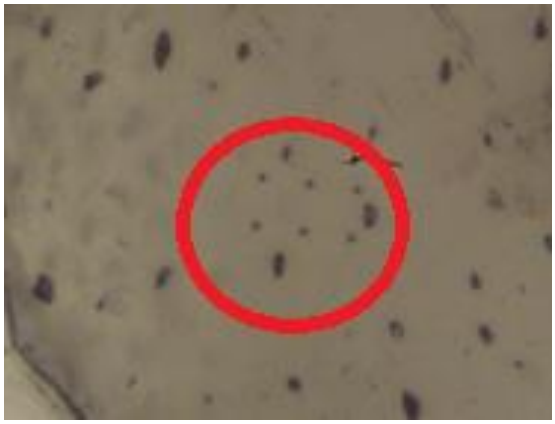

Figure 10A: C57B1/6 (X9L), first slice (the distal one). The indentations are made on the bottom of the bone in the lateral part of the tibia. The wrong curve concerns the indentation at the center of the second line

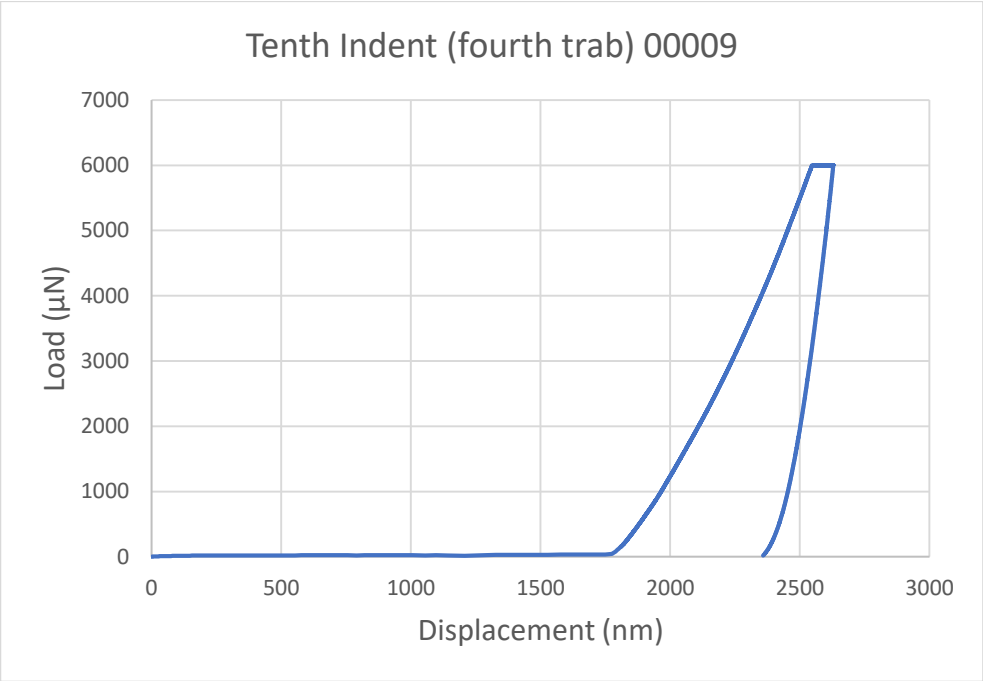

Figure 11A: Load-Displacement curve of a wrong indentation. Balb/C (L3), fifth slice (the proximal one). The indentations have been made on the trabeculae using a 3x1 grid. The wrong curve concerns the indentations made on the fourth trabecula

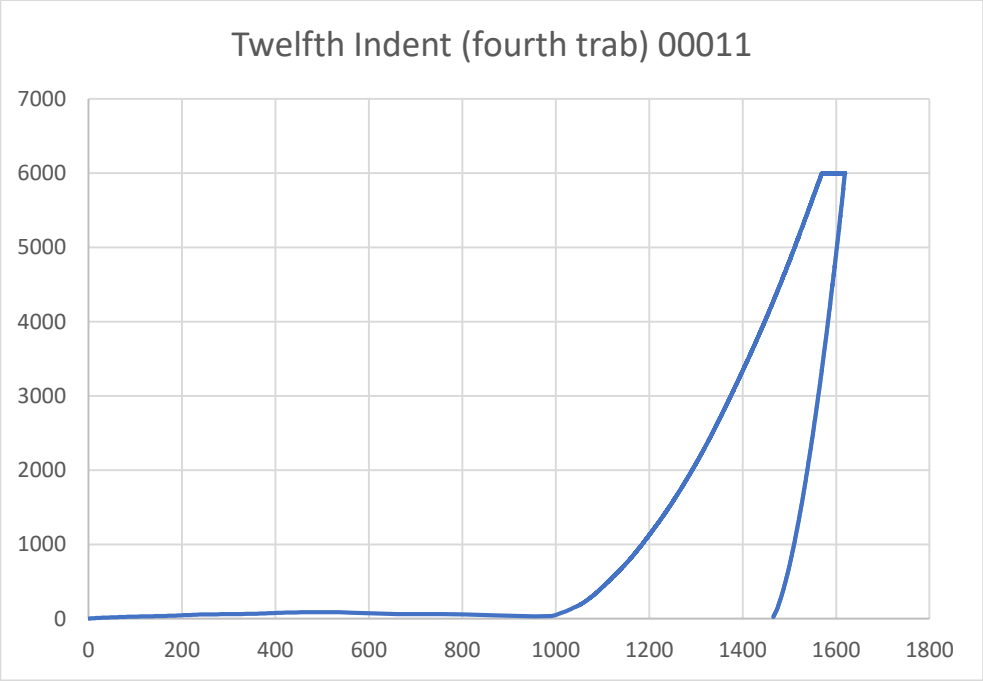

Figure 12A: Load-Displacement curve of a wrong indentation. Balb/C (L3), fifth slice (the proximal one). The indentations have been made on the trabeculae using a 3x1 grid. The wrong curve concerns the indentations made on the fourth trabecula

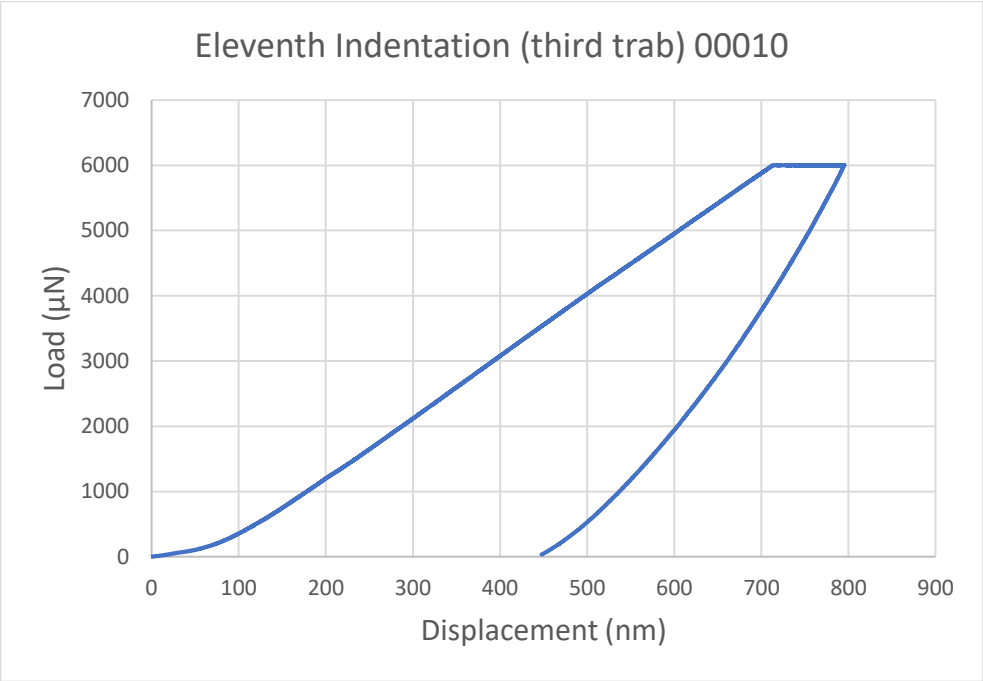

Figure 13A: Load-Displacement curve of a wrong indentation. Balb/C (L1), fifth slice (the proximal one). The indentations have been made on the trabeculae using a 5x1 grid. The wrong curve concerns the indentations made on the third trabecula

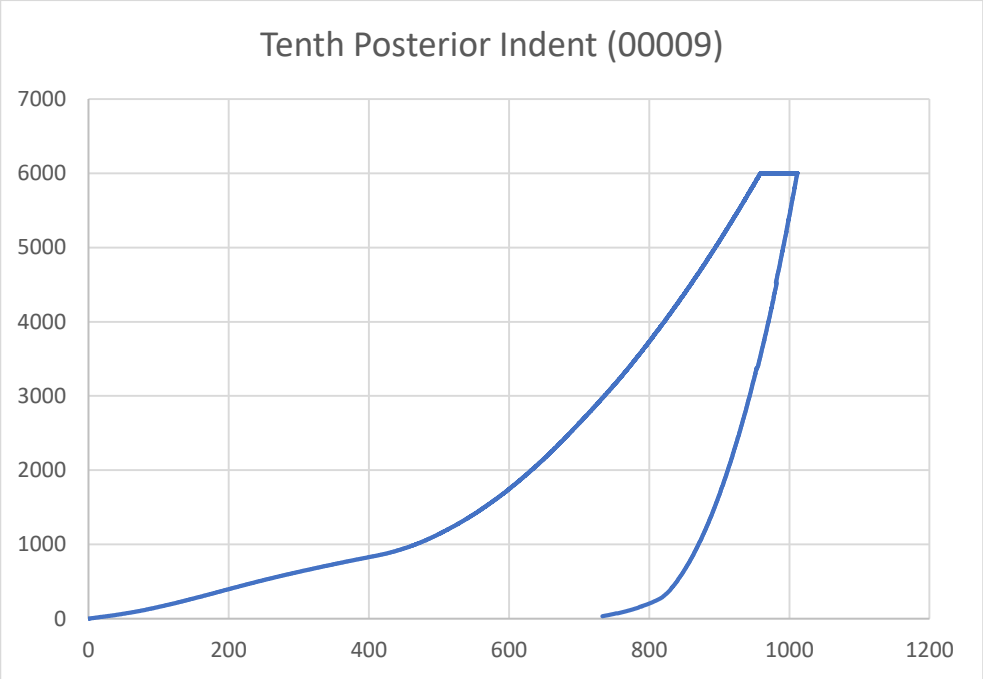

Figure 14A: Load-Displacement curve of a wrong indentation. C57B1/6 (X9L), fourth slice (the proximal one). The indentations are made on the right side of the bone in the posterior part of the tibia. The wrong curve concerns the indentation at the bottom-right

In Table 1A, indentation modulus (E_{ind}) and elastic modulus (E_b) for cortical and trabecular bone for the two mouse strains analysed are reported.

Effect of "mouse strain"			
Mechanical properties	**Bone**	**C57B1/6**	**Balb/C**
E_{ind} (GPa)	**Cortical**	24.30 ± 7.40	25.66 ± 5.43
E_b (GPa)	**Cortical**	22.11 ± 6.74	23.35 ± 4.94
E_{ind} (GPa)	**Trabecular**	16.78 ± 7.30	20.74 ± 5.20
E_b (GPa)	**Trabecular**	15.27 ± 6.64	18.87 ± 4.73

Table 1A: Results on the cortical and trabecular bone for the two different strains

In Table 2A, indentation modulus (E_{ind}) and elastic modulus (E_b) for cortical and trabecular bone for the four mice are reported.

Effect of "mouse subject"					
Mechanical properties	**Bone**	**X7L Specimen**	**X9L Specimen**	**L1 Specimen**	**L3 Specimen**
E_{ind} (GPa)	**Cort**	28.26 ± 4.79	24.12 ± 6.54	25.81 ± 6.07	27.29 ± 4.01
E_b (GPa)	**Cort**	25.72 ± 4.36	21.95 ± 5.95	23.48 ± 5.52	24.84 ± 3.65
E_{ind} (GPa)	**Trab**	21.68 ± 4.49	11.90 ± 6.03	21.14 ± 4.71	21.23 ± 3.62
E_b (GPa)	**Trab**	19.73 ± 4.09	10.83 ± 5.60	19.24 ± 4.28	19.32 ± 3.30

Table 2A: Results on the cortical and trabecular bone for the four mice

In Table 3A, E_r for both cortical and trabecular bone for the four mice are reported. The results are divided by sections.

Reduced modulus E_r (GPa)				
Region	**X7L Specimen**	**X9L Specimen**	**L1 Specimen**	**L3 Specimen**
Cort Dist	28.72 ± 3.26	27.37 ± 2.86	25.68 ± 4.24	27.24 ± 1.47
Cort Cent	30.56 ± 1.67	25.80 ± 3.91	25.30 ± 4.77	30.54 ± 2.74
Cort Prox	22.02 ± 4.36	15.39 ± 5.38	24.89 ± 7.20	24.11 ± 4.02
Trab Prox	21.26 ± 4.33	11.74 ± 5.89	20.74 ± 4.55	20.84 ± 3.51

Table 3A: Reduced modulus on the three regions of cortical bone and on trabecular bone

In Table 4A, H for both cortical and trabecular bone for the four mice are reported. The results are divided by sections.

Hardness H (GPa)				
Region	**X7L Specimen**	**X9L Specimen**	**L1 Specimen**	**L3 Specimen**
Cort Dist	1.05 ± 0.15	0.95 ± 0.13	0.91 ± 0.15	0.97 ± 0.07
Cort Cent	1.05 ± 0.09	0.94 ± 0.14	1.10 ± 0.14	1.06 ± 0.17
Cort Prox	0.84 ± 0.16	0.65 ± 0.28	0.96 ± 0.27	0.91 ± 0.19
Trab Prox	0.80 ± 0.13	0.44 ± 0.24	0.84 ± 0.19	0.86 ± 0.17

Table 4A: Hardness on the three regions of cortical bone and on trabecular bone

In Table 5A, E_{ind} for both cortical and trabecular bone for the four mice are reported. The results are divided by sections.

Indentation modulus E_{ind}				
Region	**X7L Specimen**	**X9L Specimen**	**L1 Specimen**	**L3 Specimen**
Cort Dist	29.47 ± 3.42	28.04 ± 2.93	26.91 ± 3.69	27.91 ± 1.55
Cort Cent	31.40 ± 1.76	26.41 ± 4.10	25.89 ± 5.00	31.38 ± 2.88
Cort Prox	22.47 ± 4.51	15.62 ± 5.55	25.49 ± 7.49	24.64 ± 4.19
Trab Prox	21.68 ± 4.49	11.90 ± 6.03	21.14 ± 4.71	21.23 ± 3.62

Table 5A: Indentations modulus E_{ind} on the three regions of cortical bone and on trabecular bone

In Table 6A, E_b for both cortical and trabecular bone for the four mice are reported. The results are divided by sections.

Elastic modulus E_b				
Region	**X7L Specimen**	**X9L Specimen**	**L1 Specimen**	**L3 Specimen**
Cort Dist	26.82 ± 2.69	25.52 ± 2.67	24.49 ± 3.35	25.40 ± 1.41
Cort Cent	28.57 ± 1.60	24.03 ± 3.73	23.56 ± 4.55	28.56 ± 2.63
Cort Prox	20.45 ± 4.10	14.22 ± 5.05	23.20 ± 6.81	22.43 ± 3.81
Trab Prox	19.73 ± 4.09	10.83 ± 5.60	19.24 ± 4.28	19.32 ± 3.30

Table 6A: Elastic modulus E_b on the three regions of cortical bone and on trabecular bone

In Table 7A, mechanical properties for both cortical and trabecular bone for the two strains are reported. The results are divided by sections.

	C57B1/6			Balb/C	
Region	**E_r (GPa)**	**H (GPa)**		**E_r (GPa)**	**H (GPa)**
Cort Dist	28.28 ± 3.18	1.02 ± 0.15		26.73 ± 2.81	0.95 ± 0.11
Cort Cent	27.43 ± 4.02	0.98 ± 0.13		27.12 ± 4.87	1.08 ± 0.15
Cort Prox	18.70 ± 5.92	0.74 ± 0.25		24.50 ± 5.84	0.94 ± 0.24
Trab Prox	16.50 ± 7.02	0.62 ± 0.26		20.79 ± 4.08	0.85 ± 0.18

Table 7A: E_r and H for each spatial location and strain

The E_{ind} and E_b histograms for the two strains are reported in Fig.15A.

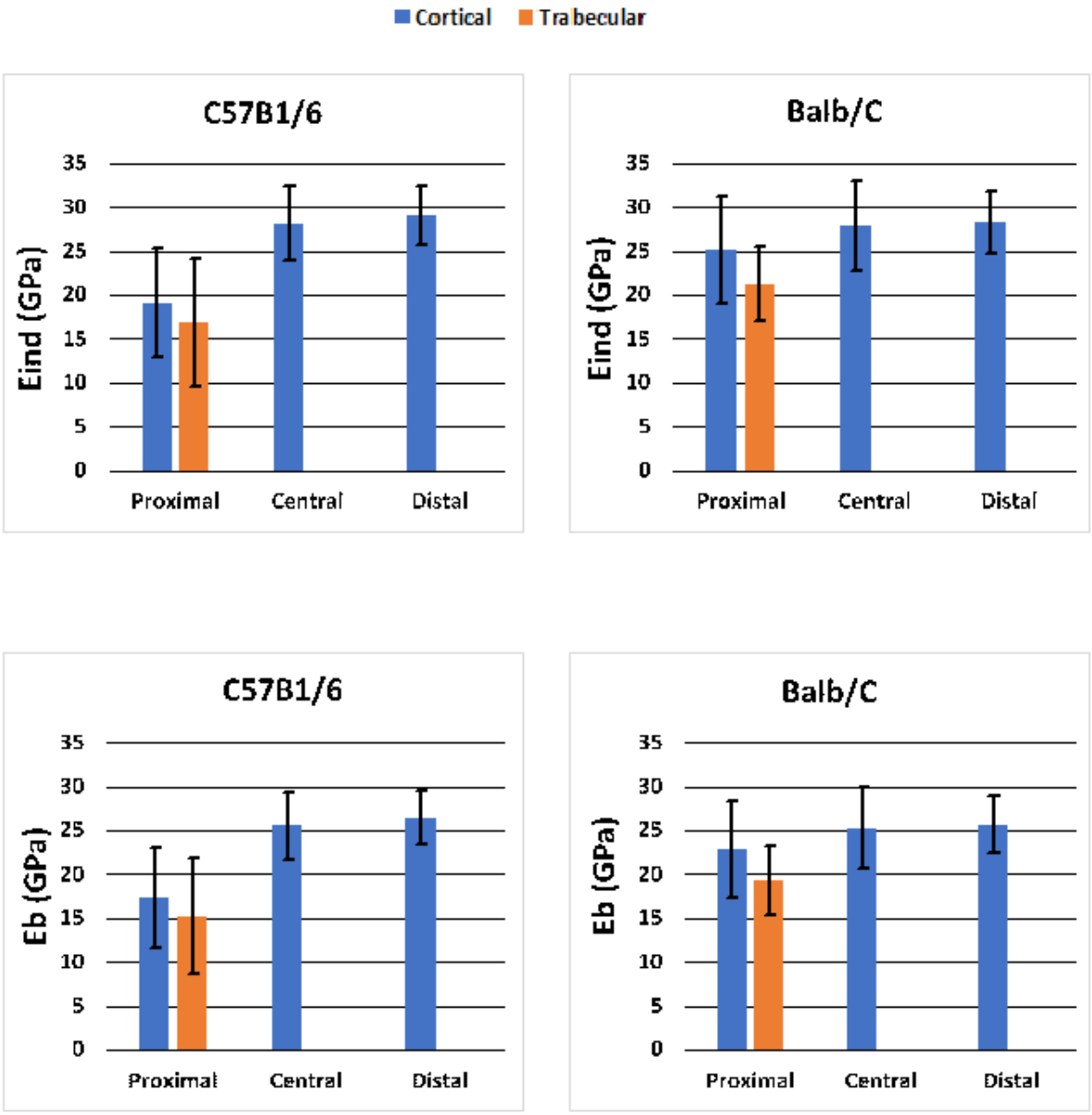

Figure 15A: E_{ind} and E_b histograms for the two strains and three sections

The mechanical properties histograms for the four mice are reported in Figs. 16A to 19A.

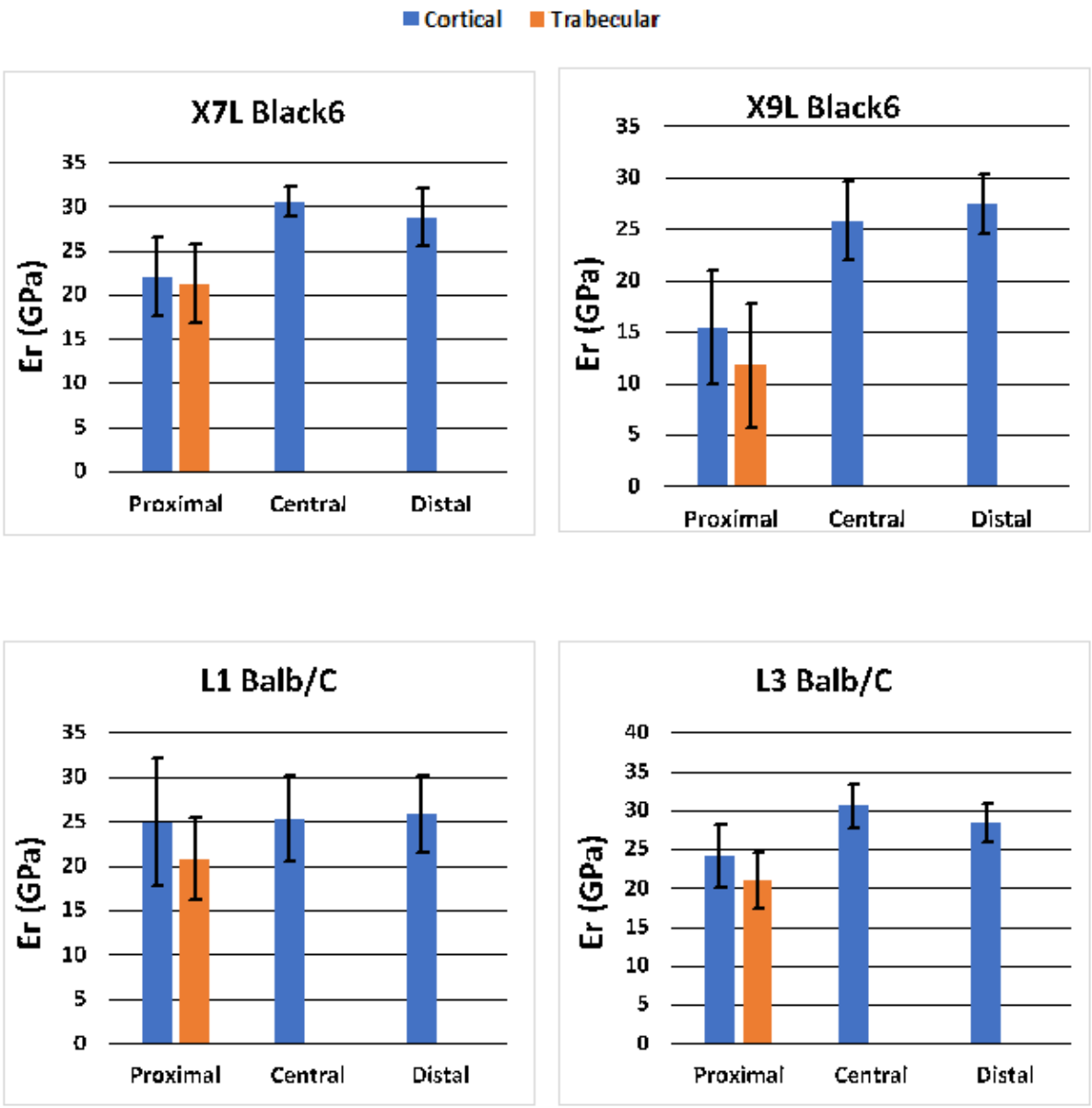

Figure 16A: E_r histograms from the four mice

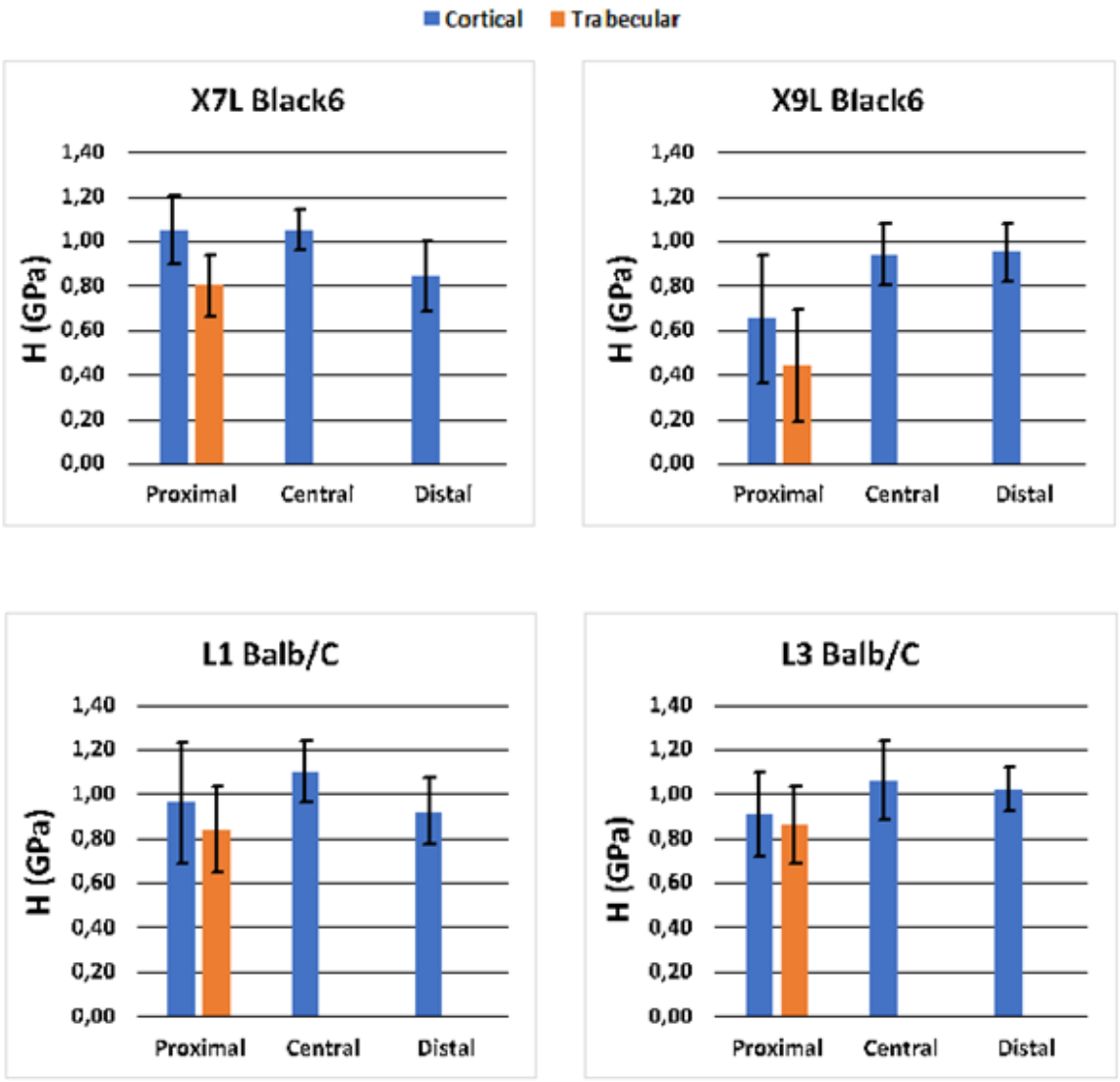

Figure 17A: H histograms from the four mice

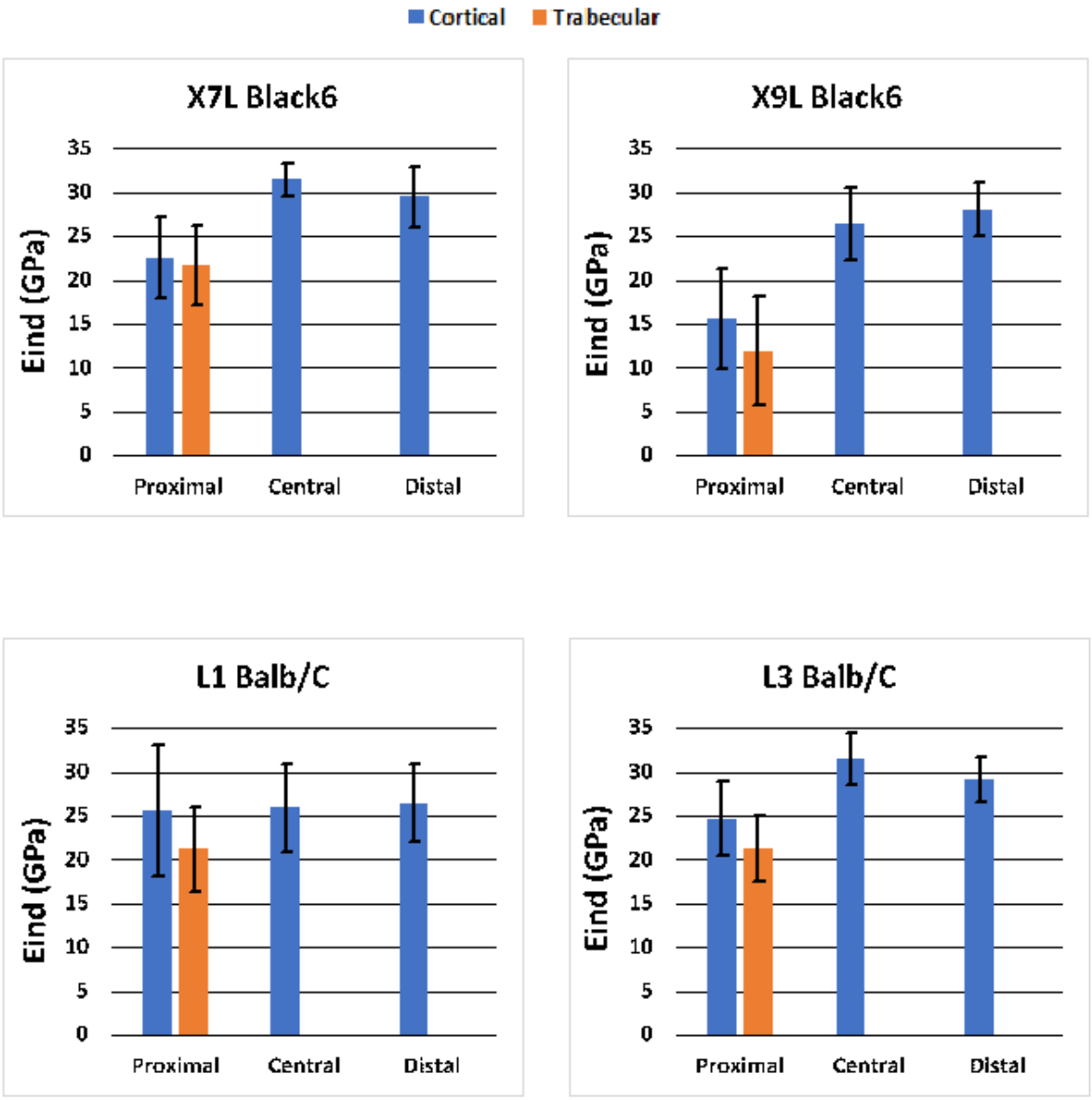

Figure 18A: E_{ind} histograms from the four mice

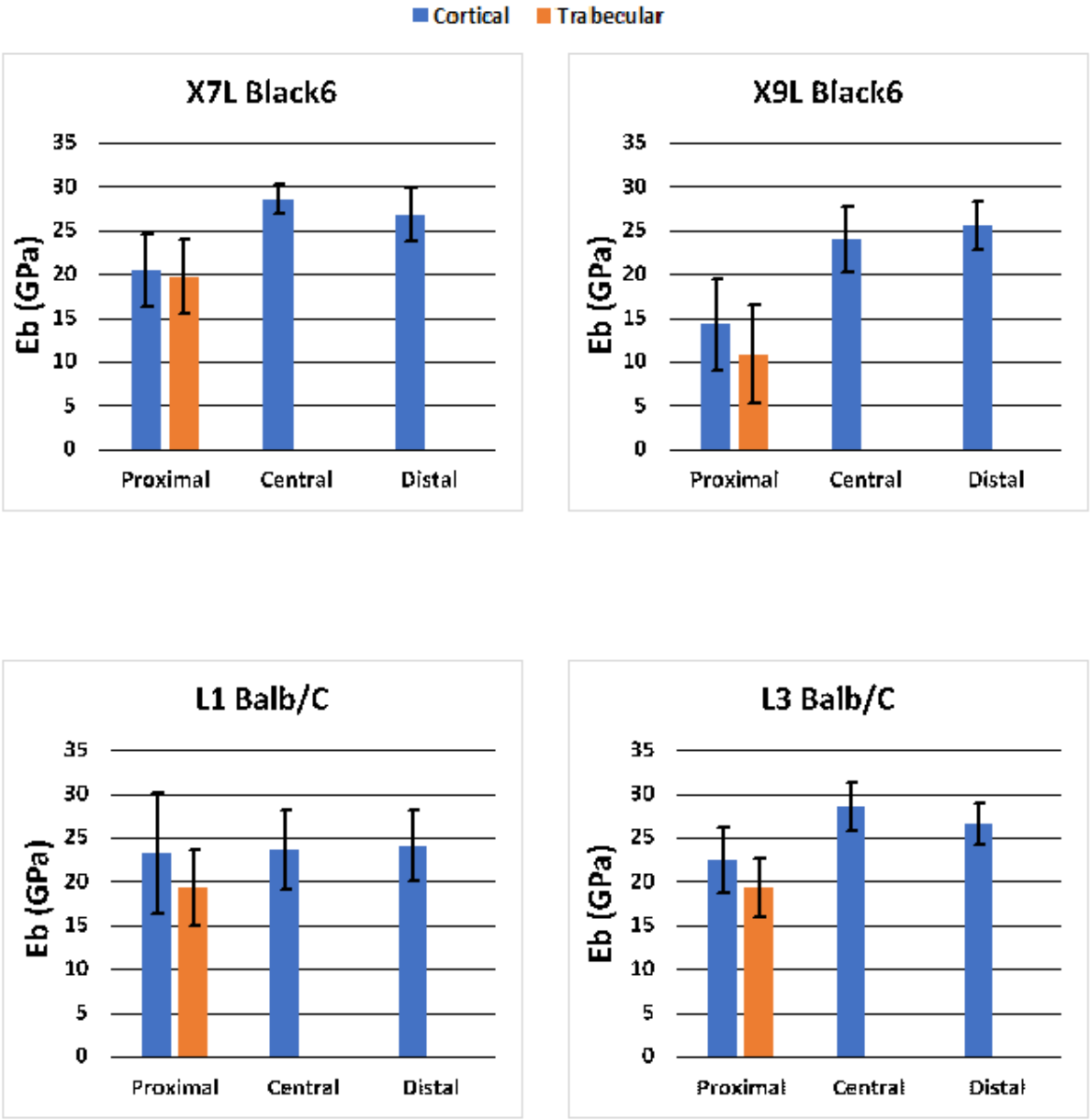

Figure 19A: E_b histograms from the four mice

In Table 8A, E_r for each mouse are reported. The results are divided by sectors.

Reduced modulus E_r (GPa)				
Sector	**X7L Specimen**	**X9L Specimen**	**L1 Specimen**	**L3 Specimen**
Anterior	26.67 ± 6.56	21.60 ± 5.60	25.26 ± 4.32	26.77 ± 4.02
Posterior	27.18 ± 2.92	24.12 ± 4.88	25.40 ± 5.33	26.83 ± 2.88
Medial	28.94 ± 3.58	24.82 ± 6.92	24.82 ± 7.88	25.25 ± 4.75
Lateral	27.45 ± 4.05	23.77 ± 7.07	25.33 ± 5.29	27.74 ± 2.89

Table 8A: Reduced modulus for each mouse and four each sector

In Table 9A, *H* for each mouse are reported. The results are divided by sectors.

Hardness *H* (GPa)				
Sector	**X7L Specimen**	**X9L Specimen**	**L1 Specimen**	**L3 Specimen**
Anterior	1.00 ± 0.21	0.74 ± 0.25	0.98 ± 0.15	1.01 ± 0.17
Posterior	0.94 ± 0.10	0.90 ± 0.11	1.02 ± 0.20	0.94 ± 0.13
Medial	1.07 ± 0.15	0.93 ± 0.21	0.98 ± 0.31	0.91 ± 0.19
Lateral	0.97 ± 0.17	0.91 ± 0.23	1.04 ± 0.19	1.01 ± 0.12

Table 9A: Hardness for each mouse and four each sector

In Tables 10A to 13A, mechanical properties for each slice are reported.

Reduced modulus E_r			
	Region	**E_r (Gpa)**	**Std**
X7L-1	Distal 1	26.61	2.76
X7L-2	Distal 2	30.83	2.29
X7L-3	Central	30.56	1.70
X7L-4	Proximal	22.02	4.46
X7L-4_trab	Proximal	21.26	4.42
X9L-1	Distal	27.37	2.86
X9L-2	Central 1	27.86	4.22
X9L-3	Central 2	23.55	1.99
X9L-4	Proximal	15.39	5.50
X9L-4_trab	Proximal	11.74	6.02
L1-1	Distal	25.83	4.31
L1-2	Central 1	29.68	2.88
L1-3	Central 2	21.11	1.11
L1-4	Proximal 1	30.66	2.60
L1-5	Proximal 2	19.12	5.65
L1-5_trab	Proximal 2	20.74	4.65
L3-1	Distal 1	27.22	1.50
L3-2	Distal 2	29.66	2.68
L3-3	Central	30.54	2.80
L3-4	Proximal 1	26.42	3.17
L3-5	Proximal 2	21.80	3.54
L3-5_trab	Proximal 2	20.84	3.59

Table 10A: Reduced modulus Er for each slice

Hardness *H*			
	Region	**H (Gpa)**	**Std**
X7L-1	Distal 1	0.98	0.16
X7L-2	Distal 2	1.11	0.12
X7L-3	Central	1.05	0.09
X7L-4	Proximal	0.84	0.16
X7L-4_trab	Proximal	0.80	0.14
X9L-1	Distal	0.95	0.13
X9L-2	Central 1	0.95	0.14
X9L-3	Central 2	0.94	0.14
X9L-4	Proximal	0.65	0.29
X9L-4_trab	Proximal	0.44	0.25
L1-1	Distal	0.92	0.15
L1-2	Central 1	1.17	0.16
L1-3	Central 2	1.03	0.08
L1-4	Proximal 1	1.16	0.13
L1-5	Proximal 2	0.76	0.23
L1-5_trab	Proximal 2	0.84	0.19
L3-1	Distal 1	0.97	0.07
L3-2	Distal 2	1.07	0.10
L3-3	Central	1.06	0.18
L3-4	Proximal 1	1.02	0.13
L3-5	Proximal 2	0.81	0.19
L3-5_trab	Proximal 2	0.86	0.17

Table 11A: Hardness H for each slice

Indentation modulus E_{ind}			
	Region	**E_{ind} (GPa)**	**Std**
X7L-1	Distal 1	27.25	2.88
X7L-2	Distal 2	31.69	2.41
X7L-3	Central	31.40	1.80
X7L-4	Proximal	22.47	4.61
X7L-4_trab	Proximal	21.68	4.59
X9L-1	Distal	28.04	3.00
X9L-2	Central 1	28.57	4.41
X9L-3	Central 2	24.05	2.07
X9L-4	Proximal	15.62	5.67
X9L-4_trab	Proximal	11.90	6.16
L1-1	Distal 1	26.44	4.49
L1-2	Distal 2	30.47	3.03
L1-3	Central	21.51	1.15
L1-4	Proximal 1	31.51	2.75
L1-5	Proximal 2	19.47	5.81
L1-5_trab	Proximal 2	21.14	4.81
L3-1	Distal 1	27.88	1.57
L3-2	Distal 2	30.46	2.83
L3-3	Central	31.38	2.95
L3-4	Proximal 1	27.05	3.32
L3-5	Proximal 2	22.24	3.67
L3-5_trab	Proximal 2	21.23	3.70

Table 12A: Indentation modulus Ei_{nd} for each slice

Elastic modulus E_b			
	Region	**E_b (GPa)**	**Std**
X7L-1	Distal 1	24.80	2.62
X7L-2	Distal 2	28.84	2.19
X7L-3	Central	28.57	1.64
X7L-4	Proximal	20.45	4.19
X7L-4_trab	Proximal	19.73	4.18
X9L-1	Distal 1	25.52	2.73
X9L-2	Distal 2	26.00	4.02
X9L-3	Central	21.89	1.88
X9L-4	Proximal	14.22	5.16
X9L-4_trab	Proximal	10.83	5.60
L1-1	Distal 1	24.06	4.08
L1-2	Distal 2	27.73	2.76
L1-3	Central	19.57	1.05
L1-4	Proximal 1	28.68	2.50
L1-5	Proximal 2	17.72	5.29
L1-5_trab	Proximal 2	19.24	4.37
L3-1	Distal 1	25.37	1.43
L3-2	Distal 2	27.72	2.57
L3-3	Central	28.56	2.68
L3-4	Proximal 1	24.62	3.02
L3-5	Proximal 2	20.23	3.34
L3-5_trab	Proximal 2	19.32	3.37

Table 13A: Elastic modulus E_b for each slice

The E_{ind} and E_b histograms for the OI human bone are reported in Fig. 20A.

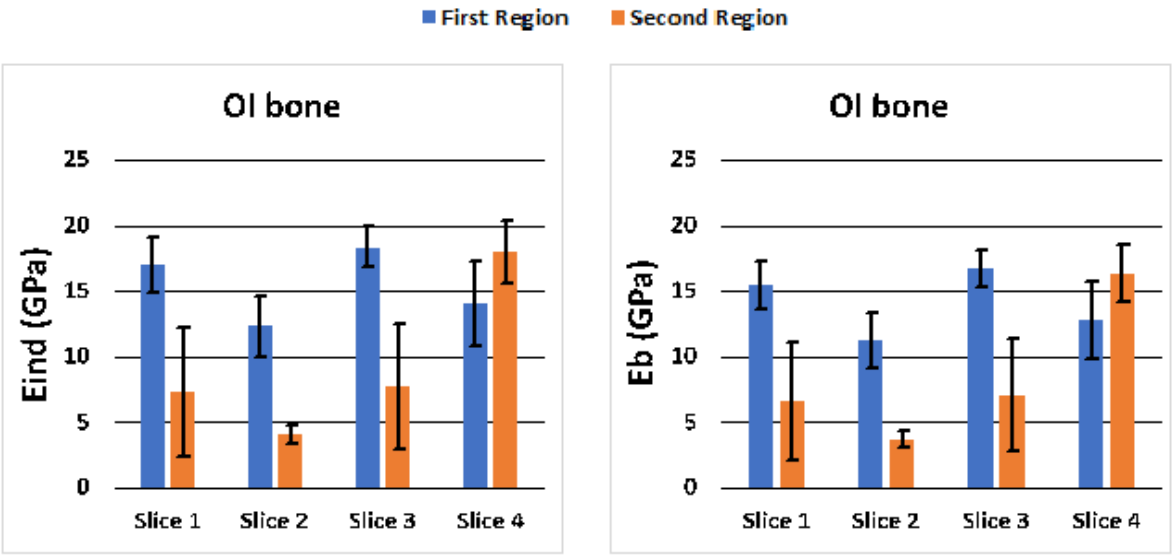

Figure 20A: E_{ind} and E_b histograms from the OI human bone